



**BANDWIDTH ANALYSIS OF A TIGHTLY-PACKED CROSSED-DIPOLE ARRAY
FOR SATELLITE COMMUNICATIONS**

THESIS

Lawrence J. Lee, Captain, USAF

AFIT-ENG-MS-18-M-041

**DEPARTMENT OF THE AIR FORCE
AIR UNIVERSITY**

AIR FORCE INSTITUTE OF TECHNOLOGY

Wright-Patterson Air Force Base, Ohio

DISTRIBUTION A. Approved for public release: distribution unlimited.

The views expressed in this thesis are those of the author and do not reflect the official policy or position of the United States Air Force, the Department of Defense, or the United States Government.

This material is declared a work of the U.S. Government and is not subject to copyright protection in the United States.

AFIT-ENG-MS-18-M-041

BANDWIDTH ANALYSIS OF A TIGHTLY-PACKED CROSSED-DIPOLE ARRAY
FOR SATELLITE COMMUNICATIONS

THESIS

Presented to the Faculty
Department of Electrical and Computer Engineering
Graduate School of Engineering and Management
Air Force Institute of Technology
Air University
Air Education and Training Command
in Partial Fulfillment of the Requirements for the
Degree of Master of Science in Electrical Engineering

Lawrence J. Lee, B.S.E.E.

Captain, USAF

March 2018

DISTRIBUTION A. Approved for public release: distribution unlimited.

AFIT-ENY-MS-18-M-041

BANDWIDTH ANALYSIS OF A TIGHTLY-PACKED CROSSED-DIPOLE ARRAY
FOR SATELLITE COMMUNICATIONS

Lawrence J. Lee, B.S.E.E.

Captain, USAF

Committee Membership:

Andrew J. Terzuoli, PhD
Chair

Peter J. Collins, PhD
Member

Colonel Dane F. Fuller, USAF, PhD (Member)
Member

Dan S. Janning, PhD
Member

Ronald J. Marhefka, PhD
Member

Abstract

A bandwidth analysis of a tightly-packed crossed-dipole array antenna is presented in this thesis. A parametric study is described which varies the element spacing in the array and the resulting change in the terminal impedances is reported. The increased mutual coupling seen by the elements as a result of smaller element spacings is shown to minimize the variation in the value of the elements terminal currents across a 0.3 GHz to 3.0 GHz frequency range. This small variation in current translates into a minimal variation in the terminal impedances for a fixed excitation voltage. This is shown to be an ideal condition in which to perform a wide-band impedance matching technique using stepped-transmission lines to bring the voltage-standing-wave-ratio (VSWR) of the array below 2. The analysis is performed using a method-of-moments computational electro-magnetics code which models the antenna as a finite-by-infinite array using Floquet Mode expansion. The current distribution and the far-field pattern across the L-band frequency range for the array is also presented.

This work is dedicated to my family, friends and mentors who have supported me and guided me through my time at AFIT.

Acknowledgments

I would like to acknowledge the professors at AFIT, the committee members, and mentors who have made this research possible. In particular, I would like to acknowledge Dr. Marhefka for his continually helpful feedback, guidance and expertise throughout this research process. I am also very grateful to Dr. Janning for his advice and for his help in implementing the computer codes used in this thesis. Throughout the research process, Dr. Collins has provided valuable instruction in the area of computational electro-magnetics, which has been an important part of this research. I would also like to thank Colonel Fuller for his guidance and for providing his expertise on space systems. I am indebted to my fellow students at AFIT and the research assistants who have helped me along the way. Finally, I would like to thank my advisor, Dr. Terzuoli, for providing me with all of the resources I needed to conduct this research and for continually supporting me and challenging me to succeed.

Lawrence J. Lee

Table of Contents

	Page
Abstract	iv
Dedication	v
Acknowledgments	vi
Table of Contents	vii
List of Figures	ix
List of Tables	xi
List of Acronyms	xii
 I. Introduction	 1
1.1 Overview	1
1.2 Problem Statement	3
1.3 Research Objectives	3
1.4 Assumptions and Limitations	4
1.5 Methodology	6
1.6 Summary	7
 II. Background and Literature Review	 8
2.1 Deployable Cruciform Antenna	9
2.2 Periodic Arrays and Frequency Selective Surfaces	11
2.3 Stepped-Transmission Line Wide-band Matching	12
 III. Methodology	 15
3.1 Parametric Study on Inter-element Spacing and the Effect on Bandwidth	15
3.1.1 Array Geometry Description	15
3.1.2 Parametric Study Approach	18
3.2 Using SPLAT to Model the Array	22
3.2.1 Code I/O	23
3.2.2 Frequency Sweep Mode	24
3.2.3 Bistatic Pattern Mode	25

	Page
3.2.4 SPLAT Geometry Definitions and Array Construction	27
3.2.5 SPLAT Theory and Principles of Operation	30
3.2.5.1 Infinite Column Array Floquet Currents	30
3.2.5.2 Column Array Green's Functions, Near-Zone E-Field and Far-Zone E-Field	33
3.2.5.3 Thin-Wire Method-of-Moments	37
3.3 Stepped Transmission Line Wide-band Matching	41
3.3.1 Single-Stage Stepped-Transmission Line Matching	43
3.3.2 Two-Stage Stepped-Transmission Line Matching	47
3.4 Plotting the Array Currents and the Far-Field	51
IV. Results and Analysis	54
4.1 Array Element Spacing - Parametric Study	54
4.1.1 Vertical Elements of the Two-Column Collinear Array and Ground Plane Distance	54
4.1.1.1 Vertical Dipole Array Ground Plane Distance Results	59
4.1.2 Horizontal Elements of the Two-Column Collinear Array	63
4.2 Stepped-Transmission Line Wide-band Matching	64
4.2.1 Impedance Matching Results: Two-Column Collinear Array	65
4.2.2 Impedance Matching Results: Two-Column Staggered Array	68
4.3 Current Distributions on the Array Dipoles	71
4.3.1 Current Distribution on Two-Column Collinear Array	72
4.3.2 Current Distribution on Two-Column Staggered Array	77
4.4 Tightly Packed Dipole Array Far-field Patterns	78
4.4.1 Far-Field Amplitude Plot: Two-Column Collinear Array	78
4.4.2 Far-Field Amplitude Plot: Two-Column Staggered Array	84
V. Conclusion	90
Appendix: Full Results	92

List of Figures

Figure	Page
2.1 Cruciform reflector antenna	9
2.2 Deployment of the cruciform reflector antenna	10
2.3 108-Element crossed-dipole array feed design	11
3.1 Two-column collinear and staggered array geometries	16
3.2 Parametric Study Chart	20
3.3 SPLAT Cell	27
3.4 Two-column crossed dipole array configurations with ground-planes.	29
3.5 Plot of the unweighted sinusoidal basis functions	32
3.6 Terminal impedances plotted on Smith Chart	42
3.7 Stepped-transmission line matching diagram	44
3.8 Single-stage stepped-transmission line matching process	45
3.9 Dual-stage stepped-transmission line matching process	49
3.10 MATLAB GUI screenshot for fine tuning transmission line length	50
3.11 Current distribution reconstructed from weighted basis functions	51
4.1 Terminal impedance comparisons for varying D_z and D_x for vertical elements .	55
4.2 Real and imaginary components of terminal impedances with varying D_z and D_x	60
4.3 Plots of normalized reactances	61
4.4 Terminal impedances for varying ground plane distances for vertical elements .	62
4.5 Terminal impedance comparisons for varying D_z and D_x for horizontal elements	63
4.6 Terminal impedances for varying ground plane distances for horizontal elements	64
4.7 Impedance matching results for two-column collinear vertical dipole array . . .	65
4.8 Impedance matching results for two-column collinear horizontal dipole array .	67
4.9 Impedance matching results for two-column staggered vertical dipole array . .	68

Figure	Page
4.10 Impedance matching results for two-column staggered horizontal dipole array .	70
4.11 Current distributions on collinear array at 1.5 GHz	73
4.12 Current distribution on collinear array for L-band frequencies	75
4.13 Current distribution on collinear array for limits of the impedance bandwidth frequencies	76
4.14 Current distribution on staggered array	77
4.15 $ \mathbf{E}_\theta $ Far-field amplitude azimuthal pattern for collinear crossed-dipole array . .	79
4.16 $ \mathbf{E}_\theta $ far-field amplitude elevation pattern for collinear crossed-dipole array . . .	80
4.17 Cruciform reflector geometry fill-angle	81
4.18 $ \mathbf{E}_\phi $ Far-field amplitude azimuthal pattern for collinear crossed-dipole array . .	83
4.19 $ \mathbf{E}_\phi $ Far-field amplitude elevation pattern for collinear crossed-dipole array . . .	84
4.20 $ \mathbf{E}_\theta $ Far-field amplitude azimuthal pattern for staggered crossed-dipole array . .	86
4.21 $ \mathbf{E}_\theta $ Far-field amplitude elevation pattern for staggered crossed-dipole array . .	87
4.22 $ \mathbf{E}_\phi $ Far-field amplitude azimuthal pattern for staggered crossed-dipole array . .	88
4.23 $ \mathbf{E}_\phi $ Far-field amplitude elevation pattern for staggered crossed-dipole array . .	89

List of Tables

Table	Page
3.1 Configurations used in the parametric study for the collinear arrays	21
3.2 Array parameters used to model the staggered array configuration	22
4.1 Parametric study table	54
4.2 Impedance matching results	71
4.3 Collinear and Staggered Array Beamwidth Calculations	82

List of Acronyms

Acronym	Definition
AFIT	Air Force Institute of Technology
AFOSR	Air Force Office of Scientific Research
AIAA	American Institute of Aeronautics and Astronautics
CEM	Computational Electro-Magnetics
FBW	Fractional Bandwidth
FORTTRAN	Formula Translation
FSS	Frequency Selective Surfaces
GUI	Graphical User Interface
IEEE	Institute of Electrical and Electronics Engineers
I/O	Input/Output
MATLAB	Matrix Laboratory
PEC	Perfect Electric Conductor
RF	Radio Frequency
R-X	Resistance vs. Reactance
SPLAT	Scattering from Periodic Linear Array of Thin-wire elements
VSWR	Voltage-Standing-Wave-Ratio

BANDWIDTH ANALYSIS OF A TIGHTLY-PACKED CROSSED-DIPOLE ARRAY FOR SATELLITE COMMUNICATIONS

I. Introduction

1.1 Overview

Deployable reflector antennas are often used on communication satellites because they can provide high gain and directivity once they are placed in orbit. These types of antennas are designed to be space and weight efficient and can be folded and stowed inside of the limited volume of a launch vehicle's payload fairing. Traditionally, many of these deployable antenna designs have used flexible, expanding parabolic membranes to form the main reflector. As an alternative, one antenna design that is being studied for its feasibility uses a cross-shaped deployable reflector that opens through a series of expanding cells that are built into the arms [1]. A reflective mesh material is suspended between the cells that make up each arm. The final shape of the deployed reflector forms two orthogonal reflecting arms each with a curvature that follows a parabolic contour. This reflector is being studied as part of an Air Force Office of Scientific Research (AFOSR) sponsored project. Previous studies have considered the mechanical feasibility of the deployment mechanism and the electrical properties of the reflector [1], [2]. Several designs for the feed have also been investigated which focused on tailoring the beam pattern to efficiently fill the surface of the reflector [3], [4]. These studies for the feed have thus far been limited to a single frequency analysis at 1.5 GHz. This frequency was chosen because the surface of the reflector was designed with a mesh density fine enough to support the L-band range of frequencies from 1 - 2 GHz [1].

The focus of this thesis is in designing a suitable feed for the cruciform reflector which provides an impedance bandwidth large enough to cover the L-band frequencies. The impedance bandwidth is defined in this study as the set of frequencies where the Voltage-Standing-Wave-Ratio (VSWR) at the terminals of the antenna is less than 2:1. This commonly used metric for describing the impedance bandwidth of antennas ensures that as much power is delivered to the antenna as possible from the generator, and that minimal power is reflected back towards the generator. A threshold VSWR of 2 means that at a maximum, the reflected power lost at the terminals of the antenna is limited to 11% of the total power supplied by the generator at the L-band frequencies.

The approach for designing the feed will start by first considering a general array antenna layout with a loosely defined physical spacing between the array elements. The general array design consists of several rows and columns of tightly spaced crossed-dipole elements. This kind of array configuration was proposed as a promising feed design because similarly configured tightly packed array structures have been used to produce broadband antennas in the past [5]. The array elements are chosen to be crossed-dipoles to produce the circular polarization for the emitted wave which is necessary for satellite communications [6]. A parametric study will be performed on this general design by varying the spacing between the array elements. The terminal impedances and reflection coefficients for each element will be observed as the element spacing is varied. The spacing configurations which produce the most favorable impedance characteristics will be identified. The findings of the parametric study will then be used to define a specific element spacing for the array to create a final feed design.

Next, a wide-band impedance matching network will be developed that would be applied to the terminals of the array elements in the feed. This matching network will be used to transform the impedances that were calculated for the array in the 1-2 GHz range to ensure that the VSWR of the antenna is below 2 for all of the L-band frequencies.

The study will be conducted using a computational electromagnetics code to simulate the different array designs. This code will calculate the currents on the array elements which can then be used to find the impedances at the terminals of each element. This code will also be used to calculate the far-field radiation pattern produced by the final feed design.

1.2 Problem Statement

Previous analyses for the feed of the deployable cruciform reflector antenna have been limited to a single-frequency at 1.5 GHz. Additionally, these analyses have only looked at the far-field radiation pattern and have not addressed the impedance characteristics of the feed. These impedance characteristics are critical in determining the radiation efficiency of an antenna across the desired bandwidth. Therefore, this study focuses on designing a feed which meets the bandwidth criteria of having a VSWR less than 2 for the L-band range of frequencies.

1.3 Research Objectives

The primary objective of this research is to find an array configuration based on the tightly packed crossed-dipole design to serve as a feed for the cruciform reflector antenna.

Additionally, this research uses the theory and computational tools developed for analyzing Frequency Selective Surfaces (FSS) to model the antenna feed. Past broadband antennas based on FSS designs consisted of multiple columns of dipole arrays modeled as finite-by-infinite structures. Generally, the number of columns used in these structures were on the order of tens of columns. These antennas were shown to produce around a 4:1 fractional bandwidth [5]. The proposed crossed-dipole array for this feed reduces the number of columns down to only two. Therefore, another research objective is to see if array antennas designed at this lower limit for the number of columns in the array can still produce close to a 4:1 bandwidth without using any dielectric layers.

Another research objective is to test the efficacy of the stepped-transmission line wide-band matching technique used to bring the VSWR of the array antenna below two. This technique is simple in its implementation and only requires short sections of transmission line with differing characteristic impedances to accomplish the matching. The amount of reduction in the VSWR after implementing these simple matching networks will be noted in the study.

1.4 Assumptions and Limitations

A number of approximations are made in the investigation of the crossed-dipole arrays to simplify the analysis. The first is the modeling of the column arrays in the feed structure using infinite periodic columns. The center section of the proposed feed design is comprised of a 28-by-2 crossed-dipole array. This will be modeled in the computational electro-magnetics code using two infinitely long columns of periodically spaced elements. This allows Floquet's Theorem to be utilized which simplifies the treatment of the array currents as will be discussed in Chapter 3. The consequence of this approximation is that the edge effects are ignored in the infinite direction. Therefore, the last few elements towards the ends of the 28-by-2 array may not be modeled accurately using this approach. Nevertheless, because there are so many more elements in the one direction versus the other, this approach will sufficiently capture the impedance and radiation characteristics for the large majority of the elements in the array.

Another approximation which is made in the analysis of the feed is that the horizontal and vertical elements of each crossed-dipole are considered separately. This assumes that the orthogonal elements of a crossed-dipole do not couple when they are radiating. The justification for making this assumption stems from the fact that the radiation pattern of half-wave dipoles have a toroidal shape with the nulls in the pattern pointing in the direction parallel to the dipole orientation [7]. Treating the orthogonal elements separately allows for a greater range of geometric configurations to be considered without encountering the

physical limitation of overlapping dipoles in the parametric study. This helps isolate the effect of reducing the element spacing for each direction in the analysis.

The simulations also do not take into account how the dipoles are being mechanically supported in the array. Whether they are embedded in a substrate or supported on posts is ignored in the simulation. Furthermore, the feed-lines connecting the individual elements to the generator are not modeled from an electromagnetic interference stand-point. While the scattering effect of these physically present objects is important, the focus of this study was not necessarily to model the array in full physical fidelity in its surrounding environment. Instead, from an engineering standpoint this study focuses on designing broadband arrays using a number of fundamental design principles. As such, the analysis focuses on capturing and describing the physics of just the scattering and coupling from the array elements themselves. The ground-plane however, was considered in the study since it is a major contributor to not only the radiation pattern, but because it also has a significant effect on the bandwidth of the array as well. Furthermore, because a bulk of this thesis consists of the parametric study, rapid analyses of a large number of configurations in which the major physical effects that could be described succinctly was preferred. Full physical fidelity modeling of the feed would be appropriate at a later stage in the design maturity.

Aside from the matching network applied directly behind the terminals of each antenna, the rest of the feed network consisting of the Radio Frequency (RF) circuit elements such as directional couplers are not included in this study. The domain of this problem is restricted to observing the impedances at the terminals of the dipole elements as a result of the coupling between them. The behind-the-ground-plane problem is not considered in this study.

Finally, the array designs are limited to an analysis that does not consider any type of dielectric coatings on the array. These dielectric coatings are typically used to further

improve the bandwidth of the arrays but this study only focuses on the effect of changing the geometric spacing between elements radiating in free-space. Therefore, throughout the analysis, the permittivity and permeability constants present in the equations and simulations are the values for these constants in vacuum. All conducting surfaces were assumed to be lossless perfect electric conductors as well.

1.5 Methodology

The methodology used in this study is provided in full detail in Chapter 3, but an overview of the approach will be explained here. The general feed design described in Section 1.1 will be analyzed first in a Computational Electro-Magnetics (CEM) code called Scattering from Periodic Linear Array of Thin-wire elements (SPLAT) [8]. The vertical and horizontal element spacing between crossed-dipoles will be changed between the simulations that are executed in SPLAT. The output data from SPLAT is a file containing the calculated array element currents. This output file will be post-processed in Matrix Laboratory (MATLAB) where a number of scripts will use the array currents to calculate the terminal impedances of the individual elements. From these impedance values, the reflection coefficient and the VSWR will also be calculated and the results will be plotted on a Smith Chart. These results will show how the various element spacings affect the impedance bandwidth of the array. Based on these results, a final array configuration will be determined and this final configuration will be simulated again in SPLAT.

The terminal impedance values for this final design will then be used to develop an impedance matching network using the principles of stepped-transmission line matching. This will be done using MATLAB by applying the governing equations for the impedance transformation which results from connecting the stepped-transmission line network to the antenna terminals. The terminal impedances, reflection coefficients and VSWR after matching will again be plotted on a Smith Chart and compared to the results before matching.

Finally, the far-field radiation pattern for the final array design will be calculated using SPLAT. The output data for this type of simulation is a file containing the values of the θ and ϕ components of the electric field for different observation angles. This data will be imported into MATLAB and plotted on a polar-dB plot to show the far-field radiation pattern from the feed.

1.6 Summary

This thesis covers the design and analysis of a crossed-dipole array feed for a deployable cruciform reflector antenna for use in satellite communications. This study focuses on the impedance characteristics of the feed and will be analyzed primarily using a computational electro-magnetics code. The overall research goal is to design a feed with an impedance bandwidth covering the L-band range of frequencies. A brief discussion of the background of the project, the assumptions and limitations made in this study, and an overview of the methodology have been provided in this section.

Overall, the design and analysis of this reflector antenna is a sponsored research project funded by the Air Force Office of Scientific Research and the results of this study have implications in improving the efficiency of United States Air Force satellite communications.

II. Background and Literature Review

The literature review presented in this chapter is divided into three sections. First, the project history of the deployable cruciform reflector antenna will be discussed by summarizing three prior Air Force Institute of Technology (AFIT) theses that have analyzed different aspects of this antenna. Additionally, a number of conference articles were submitted to various Institute of Electrical and Electronics Engineers (IEEE) and American Institute of Aeronautics and Astronautics (AIAA) conferences concerning this design which will be summarized as well. Two of these articles focused specifically on the feed design.

In the second section, some of the literature concerning frequency selective surfaces and array antennas will be discussed. This section covers the texts that have developed the theory of frequency selective surfaces that were used in this study. In particular, the two books written by B.A. Munk covering this topic in detail are cited heavily throughout this thesis. Many of the derivations and design techniques used in this thesis were adopted directly from those two books. Additionally, the PhD dissertation written by D.S. Janning describes in detail the theoretical aspects of the SPLAT code used for this study. Portions of the theoretical aspects describing SPLAT's operation from that text have been reproduced in Chapter 3 of this thesis.

Lastly, the remaining section covers the topic of stepped-transmission line matching. This matching technique has been applied to a wide variety of RF devices and has had a long history of implementation. The literature on this topic stretches back to reports from the Radio Research Laboratory at Harvard University from World War II. Examples of how this technique was used to perform impedance matching in ways that are similar to what was done in this thesis are provided and discussed in this last section.

2.1 Deployable Cruciform Antenna

The deployable cruciform reflector antenna shown in Figure 2.1 was first studied at AFIT for its scattering characteristics by J.M. Wilson as part of his thesis research [2]. The antenna, referred to as the R150 antenna, was designed to have an overall length of 150 m, and a width of 6.74 m, for each of its two intersecting arms. The parabolic contour of each arm was designed so that the focal length of the reflector would be located 80 m from the center of the arms. This type of large geometry was proposed by the Air Force Office of Scientific Research to investigate large, high-gain satellite reflector antennas that could transmit at high data rates. The goal of the R150 design was to produce a reflector with a surface area which matched that of a 50 m diameter parabolic surface when deployed, yet was still small enough when stowed to fit inside of a 5 m diameter payload fairing. While several other reflector designs with multiple arms were considered that could meet this criterion, mechanical studies done by Jennings, Black and Greschik eventually favored the R150 design for its relative simplicity [9].

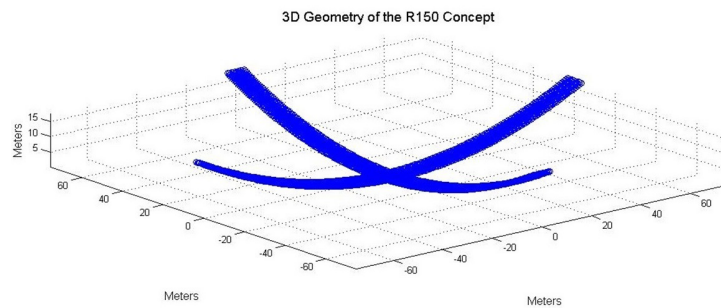


Figure 2.1: Cruciform reflector antenna

Studies of the R150 reflector from a mechanical perspective were performed by Heller et. al. [10]. These studies concluded that the reflector could be constructed robustly enough to withstand the force of deployment. This construction specified using eight graphite-epoxy truss boxes for each of the reflector arms that could collapse down into the required 5 meter storage limit. This detailed R150 deployment schematic is shown in Figure 2.2. Heller proposed using pre-deformed springs that could release the arms once in orbit and a network of Kevlar cables would maintain the curvature of the R150 arms. Additionally, his work also showed that the reflector mesh suspended between each of the truss boxes could maintain a surface-to-diameter error ratio of less than 10,000:1 allowing for reliable L-band communications. The results of Hellers work were published in his AFIT thesis and in a paper submitted to the AIAA Space Structures Conference titled “Precision of Large Deployable Reflector” in 2014 [9].

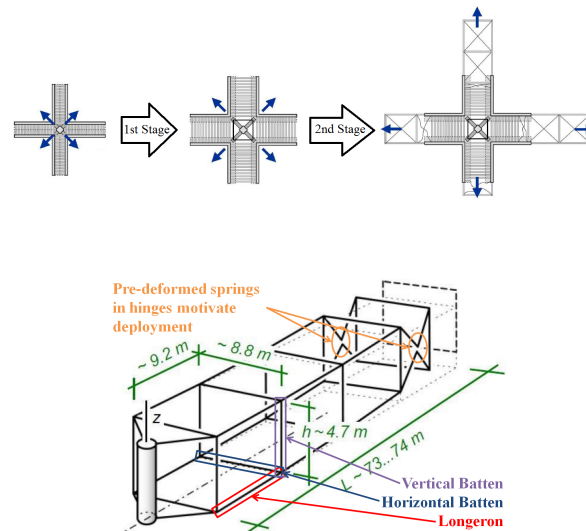


Figure 2.2: Deployment of the cruciform reflector antenna

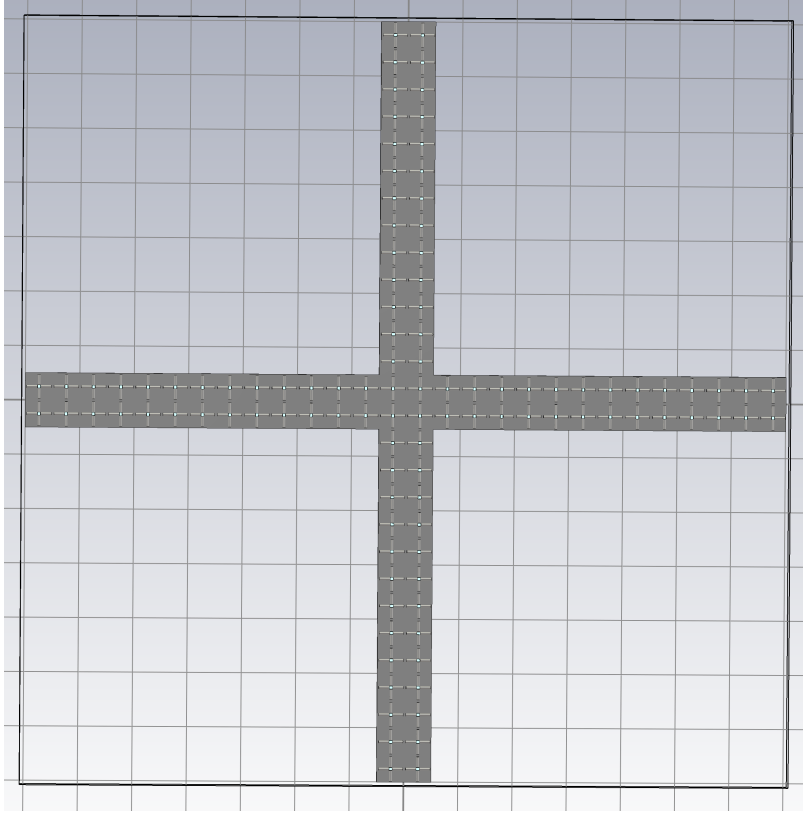


Figure 2.3: 108-Element crossed-dipole array feed design

2.2 Periodic Arrays and Frequency Selective Surfaces

The study of periodic arrays in the context of frequency selective surfaces was developed by B.A. Munk in *Frequency Selective Surfaces: Theory and Design* [5] and *Finite Antenna Arrays and FSS* [11]. In this thesis, the tightly packed crossed-dipole array is analyzed as a periodic array. Therefore, many of the techniques demonstrated in this thesis are described in those two texts by Munk. In particular, the computational electro-magnetics code, SPLAT, used in this analysis builds on the theory of finite-by-infinite arrays as developed in [11]. Crucial to the analysis of infinite periodic arrays is Floquet's Theorem, which succinctly characterizes the array element currents by relating all current values to a reference element current within the array. The application of Floquet's Theorem to the analysis of periodic antenna arrays is described in the aforementioned

works by Munk and by Bhattacharyya in his text *Phased Array Antennas: Floquet Analysis, Synthesis, BFNs, and Active Array Systems* [12].

In these texts, the Green's Functions relating the currents on an infinite array to the electric field are derived. This relationship is used to characterize the scattering properties of periodic arrays and these Green's Functions form the constitutive equations used in SPLAT [8]. A detailed description of SPLAT regarding both its theory and operation are described in the dissertation "Surface Waves in Arrays of Finite Extent" and the *SPLAT User's Guide and Programmer's Manual*, by D.S. Janning [13],[8]. A more detailed description of how the theory developed in these texts and enacted in the code are provided in Section 3.2.

Finally, the wideband potential of tightly-packed periodic arrays is described in [11]. This work demonstrates the beneficial effect that the capacitive coupling between the closely-packed array elements has on keeping the terminal impedances as constant as possible across frequency. The 4:1 bandwidth of these kinds of arrays demonstrated in [11] motivated the tightly-packed crossed-dipole array design investigated in this thesis.

2.3 Stepped-Transmission Line Wide-band Matching

In order to realize the bandwidth potential of periodic arrays, a wide-band matching network is necessary to reduce the VSWR seen at the antenna terminals. The type of matching network chosen for the antenna in this thesis is the stepped-transmission line wide-band matching network which is also described in [11]. This simple matching network consists of a series connection of transmission lines with different characteristic impedances and has been described in various works. The matching network works by establishing different reflection coefficients at the junctions between the mismatched transmission lines to cancel out the reflected wave. The result is an impedance transformation that drives down the VSWR at the antenna terminals. In this thesis, the

impedance matching is done in part through a graphical technique using the Smith Chart to visualize the impedance transformations that result from adding the matching network.

Very High Frequency Techniques Vol. I, compiled from the research conducted at the Radio Research Laboratory at Harvard University, describes broadband matching techniques that are also analyzed using graphical methods [14]. In this text, the bandwidth of RF devices (including antennas) are described through using Resistance vs. Reactance (R-X) curves. The bandwidth is related to the physical area that these curves occupy in the complex plane. The stepped-transmission line is referred to as the “series-line transformer” in [14] and its purpose is to cancel out the reflected wave from the antenna terminals. Circles of constant reflection coefficient called definition circles are established on the R-X plane and the impedance transformation caused by adding the series-line transformer is visualized by moving the points that lie outside of these circles into the definition circles. This is similar to the impedance transformation visualization on the Smith Chart that is performed in this thesis, where the goal is to move as much of the impedance curve inside of the $VSWR = 2$ circle at the center of the Smith Chart as possible. This process is described in detail in Section 3.3.

A similar technique is described in “The Design of Frequency-Compensating Matching Sections” by Rumsey [15]. This paper outlines a method of transforming a complex load impedance that changes with frequency such that the resulting transformed impedance remains as close as possible to a specified resistance over a small (50%) frequency range. The transformation and matching is accomplished via sections of quarter-wave coaxial lines. The paper describes the design procedure and provides the accompanying design equations for determining the parameters of the matching sections. The analysis is limited to quarter-wavelength sections to achieve a purely resistive transformation and hinges on the assumption that the shortest and simplest matching sections are preferred. The paper gives guidelines for using either high or low impedance

lines depending on which quadrant of the Smith Chart the original impedance curve lies. Some of the stepped-transmission line networks used in this thesis rely on a second stage consisting of a quarter-wavelength section of either higher or lower impedance than the feedline, and the analysis performed by Rumsey in [15], provides useful design guidelines.

The impedance transformation that results from adding sections of stepped-transmission lines can be described using the transmission line equations as discussed in Section 3.3. In the literature, several authors have discussed analytical techniques of determining the optimal transmission line length and characteristic impedance values to perform the matching. In this thesis, a combination of analytical and graphical techniques was used to perform the matching. Hamid and Yunik describe in their article: “On the Design of Stepped-Transmission Line Transformers,” a single frequency matching technique using an analytical and graphical method [16]. For a single frequency case, the authors describe a technique for finding a set of optimal transmission line lengths and characteristic impedances based on the ratio of the load resistance and characteristic impedance of the feedline. The results of this paper show that this method is better than the quarter-wavelength matching as shown in [15].

A purely analytical technique to find the optimal length and characteristic impedance is described by Regier in “Impedance Matching with a Series Transmission Line Section” [17]. In this paper, Regier sets up two transmission line equations: one from the load towards the feedline, and the second from the feedline towards the load. By equating the real and imaginary parts of these two equations together (assuming that the equations are equal for a perfect impedance match), the author sets up two simultaneous equations that results in a quadratic equation. The solution of the quadratic equation yields the length and characteristic impedance of the matching section. Again, the analysis in [17] is limited to a single frequency case.

III. Methodology

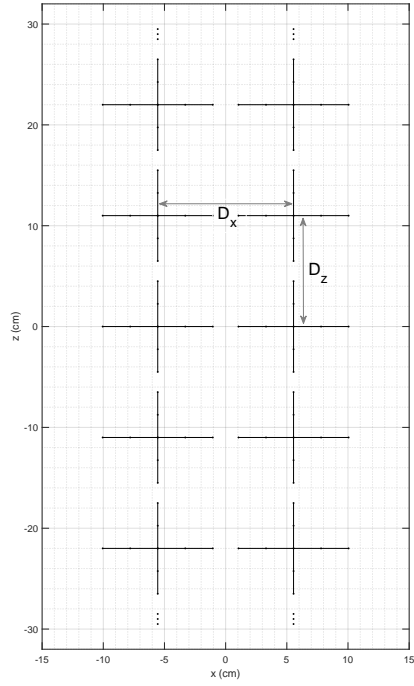
3.1 Parametric Study on Inter-element Spacing and the Effect on Bandwidth

The specific physical dimensions of the 108-element crossed-dipole array introduced in [4] and shown in Figure 2.3 was described without exact specifications given for details, such as the spacing between radiating elements, the ground plane distance, or the dipoles' lengths and thicknesses. These details were left open so that a parametric study could be conducted to find the optimal dimensions that would maximize the array's bandwidth. In this research, the parametric study to find these optimal dimensions was performed using a method-of-moments electromagnetics code to simulate the array. The details of the array geometry and the independent variables controlling the array dimensions are discussed in the following sections.

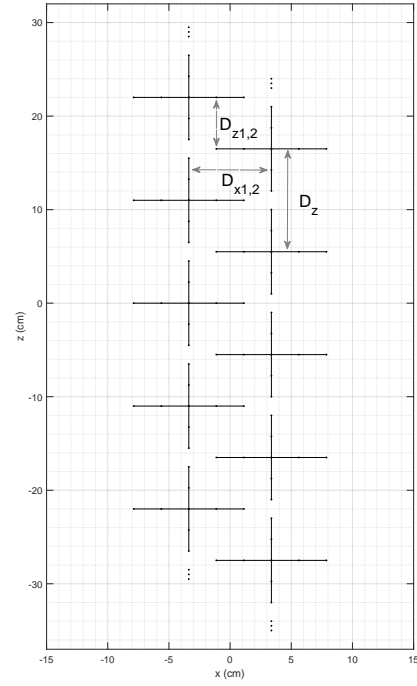
3.1.1 Array Geometry Description.

Two types of array geometries were considered in this parametric study for the crossed-dipole array. These two configurations are shown in Figure 3.1. The first configuration is a collinear arrangement of crossed-dipoles where the terminals of the dipole elements are in-line with each other. The second type of array is a staggered arrangement of crossed-dipoles which allows for a tighter spacing between radiating elements.

For the collinear configuration, the two independent variables that define the spacing between adjacent dipoles in the simulations are D_x and D_z . D_x measures the horizontal spacing between the terminals of adjacent dipoles from each column. The reference coordinate system used in this study defines the horizontal direction along the x-axis. D_z measures the vertical spacing between the terminals of adjacent dipoles within each column. The vertical direction is defined along the z-axis.



(a)



(b)

Figure 3.1: (a) Two-column collinear array configuration. (b) Two-column staggered array configuration.

For the staggered configuration, $D_{z1,2}$ defines the vertical spacing between adjacent dipoles from Column 1 to Column 2. $D_{x1,2}$ defines the horizontal spacing between adjacent dipoles from Column 1 to Column 2. D_z defines the vertical distance between the elements in the same column just as in the collinear configuration. For both configurations, the spacing distances specified by these variables are measured from the center terminals of the dipoles.

In order to reduce the number of independent variables for the parametric study, the length of every dipole was fixed at 9.0 cm and the thickness was fixed at 0.5 cm. These dimensions were chosen to create an array of half-wave dipoles at the center-frequency

of 1.5 GHz in the L-band (1-2 GHz). These were the range of frequencies for which the deployable cruciform antenna was designed [2].

The parametric study was focused on optimizing the geometry configuration of the collinear arrays, but the results from the study were used to design a staggered array configuration as well. The staggered configuration was considered in the impedance matching and pattern calculation stages of this research. This was done in order to provide a point of comparison to the collinear arrays and to show the results of what could be expected from using a denser array configuration.

It should be noted that Figure 3.1a shows only the two central vertical columns of the feed depicted in Figure 2.3. The parametric study was limited to analyzing only these two central vertical columns for two reasons. First, the cross-shaped feed depicted in Figure 2.3 is rotationally symmetric by 90° . Thus, the driving point impedance, current distribution, and far-field pattern calculated for these two vertical columns also apply to the two horizontal rows if they are rotated by 90° . Second, the method-of-moments code used to model the feed in the parametric study is designed around variable configurations of infinite vertical column arrays of dipoles [13]. One limitation of this code is that it does not model arrays that are infinite in the horizontal direction [8]. This code, called SPLAT, which stands for Scattering from Periodic Linear Array of Thin-wire elements, was originally developed for analyzing finite-by-infinite periodic arrays to study frequency selective surfaces [8]. The two central columns of the feed in Figure 2.3 were modeled as a finite-by-infinite array in this parametric study because the number of elements in the vertical dimension is much greater than the number of elements in the horizontal dimension (14:1). As such, the computed values for the terminal impedances and current distributions will be a close approximation to those found on the actual finite array—at least for the elements towards the center of the column.

This approximation of using finite-by-infinite arrays simplifies the calculation of the element currents and terminal impedances through the application of Floquet's Theorem as is discussed in Section 3.2.5. By this principle, and through a number of acceleration routines built into the code, SPLAT quickly solves for the current distributions on the array. Therefore, a large number of array geometries can be quickly simulated which makes SPLAT ideally suited for this parametric study. A detailed description of the code and an explanation of how it was used in this study is provided in Section 3.2.

3.1.2 Parametric Study Approach.

The parametric study was designed in order to test the hypothesis given in [4], which states that smaller inter-element spacings improve the bandwidth of the array by increasing the capacitive coupling between elements. The inter-element spacing in the simulations was controlled in SPLAT by specifying the D_x , D_z , or $D_{x1,2}$ and $D_{z1,2}$ dimensions shown in Figure 3.1. These spacing parameters affect the type of capacitance seen between the dipoles in the array once the elements are excited. For the collinear array, the variation in D_z affects the tip-to-tip capacitance between the vertical dipoles and the side-by-side capacitance between the horizontal dipoles. Conversely, the D_x variation affects the tip-to-tip capacitance between the horizontal dipoles and the side-by-side capacitance between the vertical dipoles. For the staggered array, the horizontal and vertical dipoles are configured in a parallel-in-echelon formation and the $D_{x1,2}$ and $D_{z1,2}$ spacings affect the capacitance seen between the staggered monopole sections. By varying one spacing parameter at a time and holding the others constant, the parametric study focused on identifying the effect that each type of capacitive coupling has on the bandwidth of the array. Ultimately, a final array configuration was chosen based on the results of this parametric study. The final design incorporated the best combination of the different types of coupling mechanisms in order to maximize the array's impedance bandwidth.

To simulate circular-polarization for the crossed-dipole elements, the horizontal and vertical dipoles were driven separately by defining two independent voltage generators at the feed gap between the horizontal and vertical elements. Since the orthogonal components of each crossed-dipole are excited separately and driven 90° out-of-phase to produce a circularly polarized wave, the horizontal and vertical elements were simulated as two separate arrays. This was done not only because of the non-interaction between the orthogonal and out-of-phase elements, but also because treating the horizontal and vertical arrays separately allowed for smaller D_x and D_z configurations to be implemented for the collinear arrangement. Although these tighter spacings would not be physically realizable in the collinear arrays—since any spacing smaller than the length of one monopole section causes the crossed-dipole elements to touch in Figure 3.1a—these configurations were included to show the effect on the impedance as the element spacings are brought to their lower limits. Furthermore, handling these dimensions separately helped distinguish the effect of tip-to-tip capacitance versus side-by-side capacitance. The separate simulations also helped distinguish the effect of capacitive coupling in the infinite versus finite array dimension.

The effect of the ground plane was also investigated in the parametric study. The ground plane not only serves to direct the radiation from the feed towards the cruciform reflector, but the literature shows that the inclusion of a ground plane is also a crucial part of extending the bandwidth of a periodic array [5]. Therefore, the parametric study investigated the effects of including, excluding and varying the distance of the ground plane between simulations. The details on how the ground plane was implemented in SPLAT using Image Theory is provided in Section 3.2.4.

For a given array configuration, the dipoles were driven by defining a 1V excitation across the terminals of the dipoles via a delta-gap generator definition in the method-of-moments code. By varying the frequency of this excitation across a one decade range

from 0.3 GHz to 3.0 GHz (which encompasses the L-band set of frequencies) the value of the terminal currents for each dipole was calculated and the frequency response of the array in this band could be observed. The phase of the voltages at the terminals was kept fixed at a 0° phase reference since the feed is not designed to scan when illuminating the cruciform reflector. The driving point impedance of the dipoles in the array across the 0.3 GHz to 3.0 GHz frequency range was calculated by dividing the terminal currents by the voltage at the dipole terminals. These driving point impedance values were then plotted on a Smith Chart in order to calculate and visualize the reflection coefficient and the VSWR across the frequency range. Figure 3.2 summarizes the parametric study approach for the collinear array configurations. The categories under each dipole orientation outline which array parameters are fixed or varying as the frequency sweep excitation is being performed.

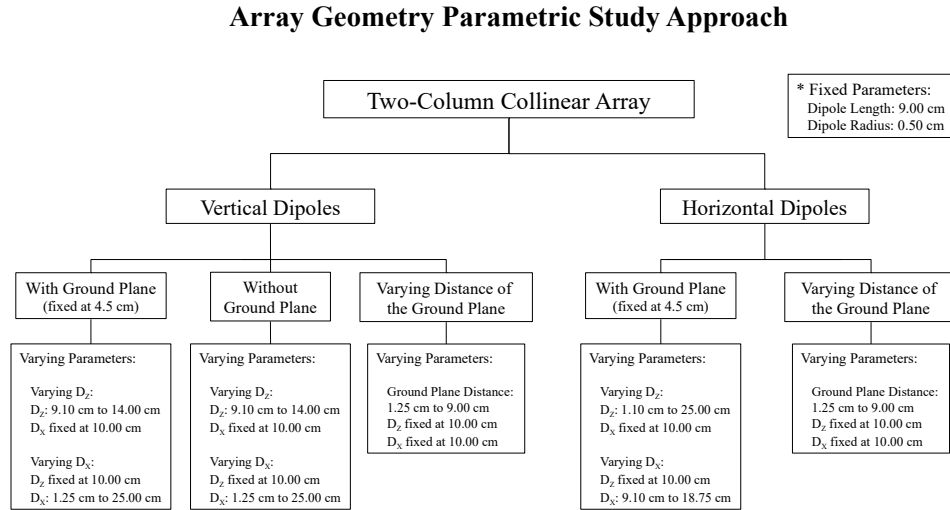


Figure 3.2: Organization of the parametric study divided into the vertical and horizontal array geometries.

The results of this parametric study are presented in Section 4.1 and were used to determine an optimal geometry for the collinear array. The optimal geometry was

determined based on the configurations that produced the tightest clustering of impedance values around the center frequency of 1.5 GHz when plotted on the Smith Chart. Because the voltage at the terminals is always fixed at 1V, a tight grouping of impedance values around the center frequency indicates that the current at the terminals of the dipoles is not changing greatly with frequency. As will be discussed in Section 4.1, this tight grouping of impedances across frequency shows the beneficial effect of the capacitive coupling in the array. This coupling helps keep the terminal currents as constant as possible across the frequency range. This proves to be advantageous when performing wide-band impedance matching which transforms the impedance curve by rotating it towards the center of the Smith Chart. As shown in Section 3.3, tighter impedance curves ensure that as much of the frequency range as possible is brought towards the center of the Smith Chart and below a VSWR of 2 (the bandwidth criterion) after matching. Table 3.1 lists all spacing arrangements for the collinear arrays that were simulated in this parametric study. The results for a similarly performing staggered array is also presented in Section 4.1.

Table 3.1: Configurations used in the parametric study for the collinear arrays.

	Element Orientation	D_z	D_x	Ground Plane Dist.	Changing Spacing ¹	Direction of Change ²
1	Vertical	9.10 cm - 14.00 cm	10 cm	No Ground Plane	Tip-to-Tip	Infinite
2	Vertical	9.10 cm - 14.00 cm	10 cm	4.5 cm	Tip-to-Tip	Infinite
3	Vertical	10.00 cm	1.25 cm - 25.0 cm	No Ground Plane	Side-by-Side	Finite
4	Vertical	10.00 cm	1.25 cm - 25.0 cm	4.5 cm	Side-by-Side	Finite
5	Vertical	10.00 cm	10.00 cm	1.25 cm - 9.00 cm	Ground-Plane Dist.	–
6	Horizontal	1.10 cm - 25.00 cm	10 cm	4.5 cm	Side-by-Side	Infinite
7	Horizontal	10.00 cm	9.10 cm - 18.75 cm	4.5 cm	Tip-to-Tip	Finite
8	Horizontal	10.00 cm	10.00 cm	1.25 cm - 9.00 cm	Ground Plane Dist.	–

*Fixed parameters: dipole lengths = 9.0 cm, dipole radii = 0.5 cm, $\epsilon_r=1$, $\mu_r=1$

1: Refers to the type of spacing layout between dipole elements that is changing

2: Indicates whether the changing spacing is occurring in the infinite or finite array dimension

The dimensions for this staggered dipole array configuration are listed in Table 3.2 below:

Table 3.2: Array parameters used to model the staggered array configuration.

	Element Orientation	D_z	$D_{z1,2}$	$D_{x1,2}$	Ground Plane Distance
1	Vertical	9.10 cm	4.55 cm	6.75 cm	5.00 cm
2	Horizontal	9.10 cm	4.55 cm	6.75 cm	5.00 cm

*Fixed parameters: dipole lengths = 9.0 cm, dipole radii = 0.5 cm, $\epsilon_r=1$, $\mu_r=1$

3.2 Using SPLAT to Model the Array

SPLAT is an electro-magnetics method-of-moments code developed at the Ohio State University's ElectroScience Laboratory [8]. The code was developed to model finite-by-infinite planar arrays of arbitrarily oriented dipole elements. As mentioned in Section 3.1.2, this code was used to compute the array currents in the parametric study, from which the driving point impedances and far-field patterns for the feed were calculated. A complete description of the theory incorporated into SPLAT is explained in [13] and [8] and will not be repeated in full detail here. However, an overview of three of the major theory components behind SPLAT's operation is necessary in order to describe the approach taken in this research and to explain some of the results. These three theory components are: (1) the expression of the array currents using Floquet's Theorem, (2) the development of the Green's Function for an infinite column array of dipoles (from which the expressions for the near-zone and far-zone E-fields are derived), and (3) the thin-wire method-of-moments used to compute the array currents. In addition to this overview of the theory, a detailed description of the approach taken to construct the collinear and staggered column arrays in SPLAT is provided. Finally, since much of the post-processing of the array currents and far-field patterns was performed outside of SPLAT in MATLAB, a description of the code Input/Output (I/O) and the details of the two modes of operation used in SPLAT that produced the results are provided as well. The code I/O overview, description of the modes of operation and the method of array construction will be addressed first.

3.2.1 Code I/O.

SPLAT is a Formula Translation (FORTRAN) program that requires several input files that must be provided before the program is executed. Although a number of these input files are optional depending on the simulation parameters, two files that must always be present are the Command File and the Geometry File.

The Command File specifies which mode of operation the code should be run in (monostatic pattern, bistatic pattern, or frequency sweep) and specifies a number of global simulation parameters such as the frequency range and scattering angles. This file also lists the names of the Geometry File, output files and any auxiliary input files used in the simulation. The Command Files used in the parametric study are provided in Appendix A.1. For this parametric study, SPLAT was run in the frequency sweep mode to calculate terminal impedances and in bistatic pattern mode to calculate the far-field.

The Geometry File specifies the dimensions of the array created in SPLAT. This file contains information on the physical dimensions of the dipoles, the spacing between elements and columns, and the material properties in the simulation. The parametric study was performed by creating a set of Geometry Files that correspond to the parameter settings specified in Table 3.1. A MATLAB wrapper batch script was then written to execute SPLAT by looping through these sets of Geometry Files and collecting the output results. Examples of the Geometry Files used to define the collinear and staggered arrays are provided in Appendix A.1.

The only other auxiliary file used in this parametric study was the Voltage Vector File. This file was used to specify the voltages applied at the terminals of the dipoles in the array. The file is simply a list of complex voltages separated into $\hat{\theta}$ and $\hat{\phi}$ components. The order of the listed voltages corresponds to the order in which the modes are defined in the SPLAT simulation environment as is discussed in Section 3.2.4. The terminal voltages were always set to a real normalized value of 1V for the study. For the vertical dipole

arrays, the $\hat{\theta}$ component of the voltage was set to 1V while the $\hat{\phi}$ component was set to 0V. Similarly, for the horizontal dipoles, the $\hat{\phi}$ component was set to 1V while the $\hat{\theta}$ component was set to 0V. An example voltage file for a collinear array is provided in Appendix A.1.

3.2.2 *Frequency Sweep Mode.*

The contents of the output file from SPLAT depend on the mode of operation in which the program is run. For the frequency sweep mode, SPLAT produces an output file which contains the value of the scattered Electric Field at a user specified output angle, and the value of the terminal currents for only the very last frequency run in the simulation. Since the goal of the parametric study was to calculate the terminal impedances using the terminal currents computed for every frequency, SPLAT was modified to produce a new output file in frequency sweep mode. This new output file lists the terminal currents for every frequency in the frequency range specified in the command file (0.3 GHz to 3.0 GHz in this study).

Thus, for the parametric study, the data collected from SPLAT was comprised of a set of output files containing the value of the terminal currents at each frequency for all of the geometric configurations specified in Table 3.1. This data was then post-processed in MATLAB. The MATLAB scripts converted these terminal currents into terminal impedances by dividing them by the terminal voltages. These impedance values were then plotted on a Smith Chart normalized to 50Ω. The reflection coefficient at the terminals of the dipoles was calculated using the following equation:

$$\Gamma = \frac{Z_L - Z_0}{Z_L + Z_0}; \quad Z_0 = 50\Omega \quad (3.1)$$

where Z_L is the terminal impedance and Z_0 is the impedance of the transmission line connecting the generator to the terminals of the dipoles. For this study, a characteristic impedance of 50Ω was defined for this feedline from the generator.

From the reflection coefficient, the VSWR at the terminals of the antenna was calculated by the following equation:

$$VSWR = \frac{1 + |\Gamma|}{1 - |\Gamma|} \quad (3.2)$$

The VSWR was plotted across the 0.3 GHz to 3.0 GHz range on a separate graph accompanying the Smith Chart for each geometry configuration listed in Table 3.1.

3.2.3 *Bistatic Pattern Mode.*

To obtain the far-field plots, SPLAT was run in bistatic pattern mode using the same Geometry and Voltage Vector Files from the frequency sweep simulations. The Command File for a bistatic pattern simulation specifies the scattering angles relative to the axis of the array for which the scattered field values are computed. The frequency of excitation and the angular resolution of the scattered field is also specified in this Command File. For a given excitation vector, the observation angles for the bistatic scattering calculated by SPLAT is limited to variation only in the azimuthal direction ($\hat{\phi}$). The $\hat{\theta}$ observation angle is fixed in the specular direction [8].

The voltages defined as the excitation in the parametric study performed in this research are always completely polarized in the $\hat{\phi}$ or $\hat{\theta}$ direction. While these voltages simulate the signal supplied from the generator, these voltages can also be thought of as being the $\hat{\phi}$ and $\hat{\theta}$ components of the excitations caused by a perfectly circularly polarized plane-wave impinging on the surface of the array at an angle normal to the \hat{z} axis. That is an incident wave with $\theta_{in} = 90^\circ$.

In this equivalent hypothetical scenario, the horizontal dipoles are excited only by the $\hat{\phi}$ component of the circularly polarized incident E-field and the vertical dipoles are excited only by the $\hat{\theta}$ component of the circularly polarized incident E-field. All of this is to say that the output observation angle, θ_{out} , for all of the bistatic pattern simulations performed in this study is fixed at 90° based on the voltage vector definitions. This is

because SPLAT calculates the θ_{out} output angle as $\theta_{out} = \pi - \theta_{in}$ [8]. Since this study uses SPLAT to simulate a radiating antenna, no incident wave is defined as an excitation. Therefore, the θ_{in} excitation angle and θ_{out} are defined solely via the voltages in Voltage Vector File.

For this reason, all of the far-field plots calculated using SPLAT in this study are limited to the great circle plane of $\theta = 90^\circ$ with ϕ varying from 0° to 360° . In other words, SPLAT in bistatic pattern mode was only used to calculate the azimuthal variation of the far-field pattern. Additionally, based on the voltage vector definition and the separate simulation of the horizontal and vertical arrays, the far-field plots are divided into two figures: one for the \mathbf{E}_ϕ component of the radiated field from the horizontal dipoles, and one for the \mathbf{E}_θ component from the vertical dipoles. These two separate plots represent the radiation pattern for the circularly polarized array and show where the \mathbf{E}_ϕ and \mathbf{E}_θ components are always 90° out-of-phase.

The output file for a bistatic pattern simulation in SPLAT lists the $\hat{\theta}$ and $\hat{\phi}$ components of the Electric Field for the ϕ_{out} scattering angles specified in the command file. The pattern was calculated for excitations at the center frequency of 1.5 GHz, the limits of the L-band at 1.0 GHz and 2.0 GHz, and for the limits of the impedance bandwidth calculated for each configuration as discussed in Section 3.3. The specific details on how the outputs of SPLAT were used to plot the far-field using MATLAB is discussed in Section 3.4.

In order to produce the elevation pattern for the far-field, the electric field was calculated outside of SPLAT in MATLAB. The array current distribution on the individual dipole elements found using SPLAT were exported to MATLAB. The far-field from a single dipole element was found and then multiplied by the appropriate array factor to calculate the total field. This method approximates the current distribution on the finite array using the infinite array currents calculated using SPLAT.

3.2.4 *SPLAT Geometry Definitions and Array Construction.*

Each infinite column in SPLAT is characterized by the physical dimensions of an arbitrarily selected reference dipole within that infinite column and the vertical spacing, D_z , between the dipoles in that column. In SPLAT, these reference dipoles are referred to as cells. The cell is constructed by the user through the Geometry Input File. The reference dipole is divided into separate nodes and segments as depicted in Figure 3.3.

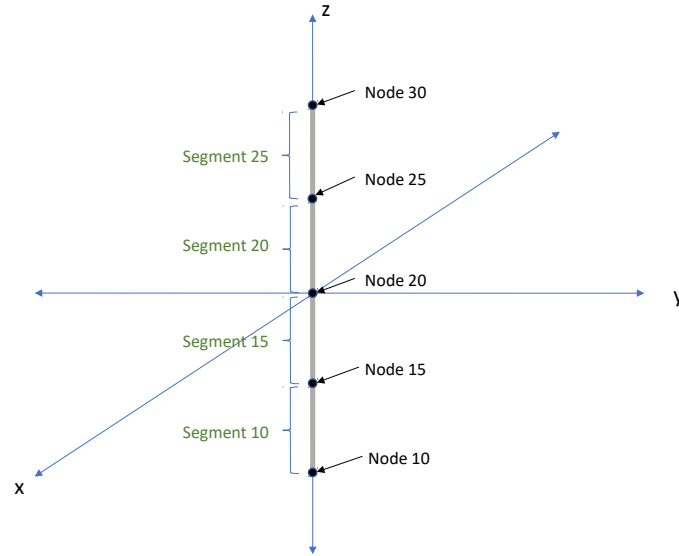


Figure 3.3: SPLAT Cell

The nodes and segments are given unique integer labels in the geometry definition. This is done so that a unique current mode (basis function) can be defined over the different sections of the dipole as shown in Figure 3.5. Each mode is assigned a unique integer label once SPLAT is run and these labels are noted in the output file. The voltages defined in the Voltage Vector File must be associated with the correct mode label in order to apply the voltages at the correct location in the array.

The reference dipole defined by the cell definition is replicated along the \hat{z} direction to form an infinite column array with the D_z spacing between dipoles that is specified in

the Geometry File. Cell definitions can then be duplicated with different coordinate offsets applied to the center of the reference dipole in order to construct multi-column arrays. If the D_z spacing is the same for the other columns, the Geometry File allows identical columns to be defined as an array using a single cell definition. A center coordinate for the array is defined separately from the center coordinate of the reference dipole. The coordinates for all of the dipoles in that geometry are then referenced to the center coordinate of the array. This approach was used to construct the two-column collinear array as shown in Figure 3.1a. Two different cells were defined to construct the horizontal dipole array and the vertical dipole array separately. These different cells were created using separate Geometry Files in order to keep the horizontal dipole simulations separate from the vertical dipole simulations. In conducting the parametric study, the D_z and D_x offsets were changed in the Geometry Files to make the element spacings either closer or farther apart.

The array feature was also used to create an image array in order to simulate an infinite Perfect Electric Conductor (PEC) ground plane. For current sources above a PEC ground plane, the total field in the region above the ground plane can be modeled using Image Theory. The total field which is a superposition of the reflected and forward traveling wave from the current sources are equivalent to the superposition of fields from the actual current sources and the fields radiated by image currents flowing in the opposite direction located in the image plane [7]. The ground plane in the feed design shown in Figure 2.3 is located $\lambda/4$ (for λ at 1.5 GHz) behind the array. This was done in order to redirect the $-\hat{y}$ radiation from the feed back towards the cruciform reflector by a reflection off of the ground-plane. The $\lambda/4$ spacing produces a reflected wave that is in-phase by the time it reaches the feed elements. The reflected wave then constructively interferes with the forward propagating wave from the crossed-dipoles in the direction towards the cruciform reflector. The SPLAT simulation replaces the finite ground plane depicted in Figure 2.3 with an idealized infinite ground plane for simplicity in the simulation. In order to do this using Image Theory, an

image array in SPLAT was placed at $\lambda/2$ behind the actual array. This places the image array in the image plane which is double the distance away from the array as the true ground plane. Here, $\lambda = 20$ cm at the center frequency of 1.5 GHz, so the image distance in SPLAT was set to 10 cm. The crossed-dipole arrays with their respective image ground planes as constructed in SPLAT are depicted in Figure 3.4.

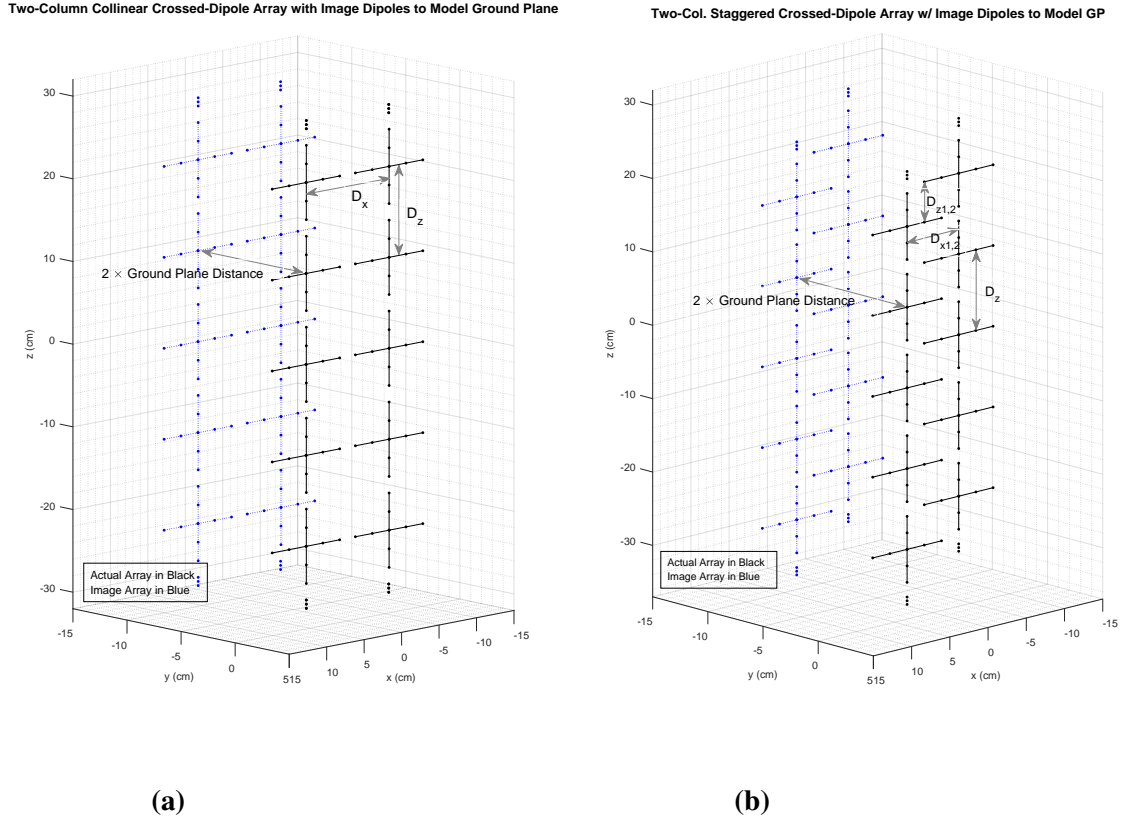


Figure 3.4: (a) Collinear arrangement with image array and (b) Staggered arrangement with image array to simulate an infinite ground plane

In order to produce currents flowing in the opposite direction for the array in the image plane, a voltage of -1V instead of 1V was applied to the terminals of the dipoles in the image array. This is equivalent to defining identical currents as those in the actual array, but with unit vectors pointing in the opposite direction for the currents in the image array.

The validity of this approach was confirmed by observing the output currents calculated by SPLAT. The image currents that are calculated always have the same magnitude but opposite sign in the output files. An example output file showing this is provided in Appendix A.1.

3.2.5 SPLAT Theory and Principles of Operation.

SPLAT calculates the currents induced on a planar array of dipoles by an excitation in the form of an incident wave or through voltages impressed at the terminals of the dipoles [8]. These currents are then used to calculate the scattered field. The currents generate the near-field which governs the mutual coupling between array elements, and the currents also generate the far-field which gives the radiation pattern for the array. For this study, the currents are also used to calculate the impedances seen at the terminals of the dipoles. Since the current plays such an important part in deriving the parameters investigated in this study, the following three sections will look into how they are generated in more detail. These sections will explain how changing the array's physical parameters affects the value of the currents. Additionally, an explanation of how the currents are solved for using the method-of-moments is provided.

3.2.5.1 Infinite Column Array Floquet Currents.

The major advantage of using infinite periodic arrays to model the 108-element crossed-dipole feed is that Floquet's Theorem can be used to succinctly describe the currents on all of the array elements. Floquet's Theorem states that: "the currents on all the elements in an infinite column are identical in magnitude and differ in phase by the same phase progression as the excitation applied to the column." [11], [12]. The consequence of Floquet's Theorem is that the currents on hisall the elements in the infinite column can be related to and described by the current on an arbitrarily selected reference element within the column. When the conditions for applying Floquet's Theorem are met, the currents on the elements of an infinite column that are described in this fashion are known as Floquet

Currents. The conditions are that the element spacings must be uniform and the phase of the excitation between the elements must be periodic [11].

For this study, the excitations are the voltages impressed at the terminals of the array dipoles. For both the collinear and staggered arrays these voltages are all set to a normalized value of 1V with no phase progression (0°) applied across the array (no beam steering). Therefore, in this study all of the element currents in an infinite column are identically equal to the current on a reference dipole in that column. SPLAT uses a method-of-moments routine to solve for the value of this reference current using information about the excitation and the field equations that dictate the mutual coupling between the elements of infinite arrays. Since the currents on all of the elements in a single infinite periodic column can be expressed using only the reference current, the problem is reduced to solving for just the unknown reference current for each infinite column in the geometry.

Given that the current distribution on a dipole is usually some variation of a sinusoidal function, the currents on the dipole elements in SPLAT are modeled using weighted combinations of the normalized sinusoidal functions given in the equation shown below [13]:

$$\bar{F}(l') = \begin{cases} \hat{p}^{(a)} \frac{\sin \beta(l^{(a)} - |l'|)}{\sin \beta l^{(a)}}; & \text{current on the "a" monopole} \\ \hat{p}^{(b)} \frac{\sin \beta(l^{(b)} - |l'|)}{\sin \beta l^{(b)}}; & \text{current on the "b" monopole} \end{cases} \quad (3.3)$$

The current is defined separately for each monopole section where $\hat{p}^{(a)}$ and $\hat{p}^{(b)}$ are unit vectors that point in the direction of each monopole's orientation (this allows for bent monopoles to be defined in the SPLAT framework). The length of each monopole segment is represented by $l^{(a)}$ and $l^{(b)}$, which allows for asymmetric dipoles to be defined. The variable l' is the distance variable along the monopole segments. In general, the currents given by Equation 3.3 can be rewritten for lossy media through using the propagation

constant $\gamma = \alpha + j\beta$ instead in Equation 3.3. By the identity $-j \sin(jz) = \sinh(z)$, Equation 3.3 becomes:

$$\bar{F}(l') = \begin{cases} \hat{p}^{(a)} \frac{\sinh \gamma(l^{(a)} - |l'|)}{\sinh \gamma l^{(a)}}; & \text{current on the "a" monopole} \\ \hat{p}^{(b)} \frac{\sinh \gamma(l^{(b)} - |l'|)}{\sinh \gamma l^{(b)}}; & \text{current on the "b" monopole} \end{cases} \quad (3.4)$$

Equation 3.4 is used to define the current distribution on the dipoles in SPLAT. To use method-of-moments terminology, Equation 3.4 is the form of the basis function that models the current on the dipoles [8]. SPLAT uses overlapping basis functions, referred to as modes, to construct the current. For the parametric study, three overlapping modes were used per dipole. Equation 3.4 is defined such that the value of the current is equal to zero at one endpoint and is equal to one at the other end point. This is shown in Figure 3.5 where each mode current is constructed from two monopole current segments:

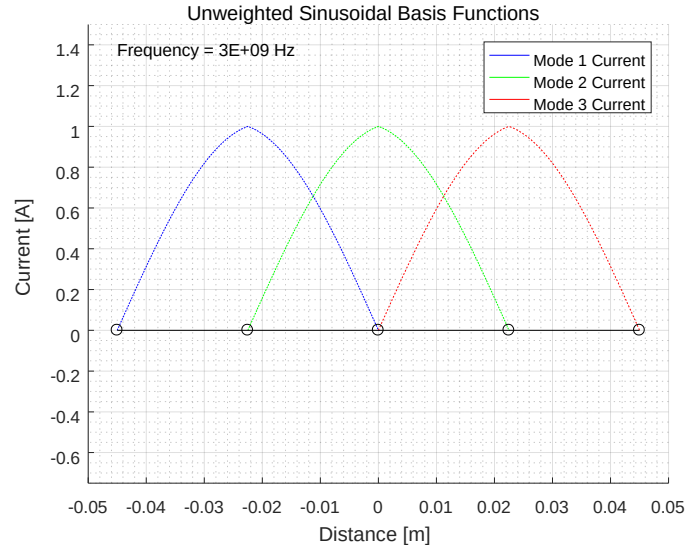


Figure 3.5: Unweighted sinusoidal basis functions

The two current segments both approach, and are equal to one, at the center of each mode. As depicted in Figure 3.5, the dipole is also divided into four segments with five nodes,

with the terminal of the dipole defined at the central node. This is consistent with the cell geometry definition shown in Figure 3.3.

The unknowns that are solved for in the method-of-moments routine are the weighting coefficients that scale these individual current basis functions. Since the basis functions are defined such that they are equal to one at one endpoint and zero at the other, at the terminals of the dipole, the three mode currents overlap such that the terminal current is completely defined by Mode 2 and only Mode 2. Since the value of the basis function defined in Equation 3.5 is equal to one at the terminal, the terminal current is completely defined by just this weighting coefficient. This property was used to extract the value of the terminal currents directly from the output file's list of complex current coefficients. The value of the current at the terminals did not have to be reconstructed from the superposition of the three weighted basis functions as is necessary elsewhere on the dipole.

Through these mode definitions and the application of Floquet's Theorem, the terminal currents for every element in an infinite column array are described completely by one number: the coefficient for the basis function at the central terminal of the reference dipole.

3.2.5.2 Column Array Green's Functions, Near-Zone E-Field and Far-Zone E-Field.

The mode currents in SPLAT are used to calculate the near-zone and far-zone E-Fields for the array. The near-zone E-Field is used to calculate the mutual coupling between the array elements. Both the near-field and the far-field are obtained by first deriving the Green's Function for a column array of infinitesimal current sources [5]. This Green's Function is then integrated along the length of the current mode expansions to obtain the Green's Function for the finite-length dipoles in one column array. A full derivation is provided in [5] and [13], but an abbreviated derivation is given below:

The infinitesimal current on the n th element in an infinite column array is described by the following equation:

$$I_n = I_0 e^{-j\beta s_z n D_z} \quad (3.5)$$

where I_0 is the magnitude of the current on the reference element, D_z is the spacing between dipoles, and β is the propagation constant. Equation 3.5 was derived assuming that a plane wave was used to excite the current. Therefore, the phase of the current is described using s_z , which is the \hat{z} component of the unit vector along the direction of propagation for that incident wave. For an excitation caused instead by terminal voltages, the phase term could be expressed by an equivalent periodic phase-progression applied across the column. As discussed in the previous section, the infinitesimal element currents expressed using Equation 3.5 are used to weight the current distribution functions of Equation 3.4 to give a complete description of the current distributions on each dipole in the array:

$$\bar{I} = I_n \bar{F}(l') \quad (3.6)$$

With the current now defined using the sinusoidal basis functions and Floquet's Theorem, the rest of the approach for deriving the near-field and far-field equations involves first deriving the Green's Function from the magnetic vector potential \bar{A} of the array. \bar{A} is found through solving the inhomogeneous vector wave equation expressed in cylindrical coordinates as:

$$\begin{aligned} \nabla^2 \bar{A} + \beta^2 \bar{A} &= -\bar{J} \\ \frac{1}{\rho} \frac{\partial}{\partial \rho} \rho \frac{\partial}{\partial \rho} \bar{A} + \frac{\partial^2}{\partial z^2} \bar{A} + \beta^2 \bar{A} &= -\bar{J} \end{aligned} \quad (3.7)$$

The current density \bar{J} for the entire infinite column of point currents is expressed using Equation 3.5, yielding:

$$\bar{J} = \hat{p} I_0 dl e^{-j\beta s_z n z} \delta(y) \delta(x) \sum_{n=-\infty}^{\infty} \delta(z - nD_z) \quad (3.8)$$

The solution for the magnetic vector potential which satisfies Equation 3.7 using the expression above for the current density is [13], we have:

$$\bar{A}(\rho, z) = \hat{p} \frac{I_0 dl}{j4D_z} \sum_{n=-\infty}^{\infty} H_0^{(2)}(\beta r_\rho \rho) e^{-j\beta r_z z} \quad (3.9)$$

where the distance variable $r_z = s_z + \frac{n\lambda}{D_z}$, and $r_\rho = \sqrt{1 - r_z^2}$ when $r_z^2 < 1$, and $r_\rho = -j\sqrt{r_z^2 - 1}$ when $r_z^2 > 1$. From the magnetic vector potential \bar{A} , the electric field for an infinite column of infinitesimal current sources can be computed from:

$$\bar{E} = \frac{1}{j\omega\epsilon} (\nabla \nabla \cdot \bar{A} + \beta^2 \bar{A}) \quad (3.10)$$

The final result describes the field radiated from the infinite column of infinitesimal current sources located on the \hat{z} axis. When the equation is written to describe the field from the array at any arbitrary location (so long as it is parallel to the z-axis), the result is the following [13]:

$$\begin{aligned} d\bar{E}(\bar{R}|\bar{R}') &= -\frac{ZI_0 dl}{4D_z} \sum_{n=-\infty}^{\infty} e^{-j\beta r_z(z-z')} \cdot \\ &\left\{ \hat{x} \left[p_x \left((r_z^2 + r_\rho^2 v_y^2) \beta H_0^{(2)} + (v_x^2 - v_y^2) r_\rho \frac{H_1^{(2)}}{\xi} \right) + p_y v_x v_y \left(2r_\rho \frac{H_1^{(2)}}{\xi} - \beta r_\rho^2 H_0^{(2)} \right) + p_z (j\beta r_\rho r_z) v_x H_1^{(2)} \right] \right. \\ &+ \hat{y} \left[p_x v_x v_y \left(2r_\rho \frac{H_1^{(2)}}{\xi} - \beta r_\rho^2 H_0^{(2)} \right) + p_y \left((r_z^2 + r_\rho^2 v_x^2) \beta H_0^{(2)} - (v_x^2 - v_y^2) r_\rho \frac{H_1^{(2)}}{\xi} \right) + p_z (j\beta r_\rho r_z) v_y H_1^{(2)} \right] \\ &\left. + \hat{z} \left[(p_x v_x + p_y v_y) (j\beta r_\rho r_z) H_1^{(2)} + p_z \beta r_\rho^2 H_0^{(2)} \right] \right\} \quad (3.11) \end{aligned}$$

The argument of the Hankel functions in the equation is $\beta r_\rho \xi$ and $\xi = |\bar{\rho} - \bar{\rho}'| = \sqrt{(x - x')^2 - (y - y')^2}$. The shifted distance variables v_x and v_y are $v_x = (x - x')/\xi$ and $v_y = (y - y')/\xi$. Z is the wave impedance of the medium which is equal to $\sqrt{\frac{j\omega\mu}{\sigma + j\omega\epsilon}}$. The d in front of $\bar{E}(\bar{R}|\bar{R}')$ indicates that this equation is for an infinite column of periodically spaced infinitesimal current point sources. The Hankel functions of the first and second kind in Equation 3.11 indicate that the field is comprised of a superposition of ingoing ($H_m^{(0)}$) and outgoing ($H_m^{(1)}$) cylindrical waves emanating from each point source.

From Equation 3.11, the equation for the electric field from one of the sinusoidal basis functions (modes) comprising the current on the reference dipole of the array (which by Floquet's Theorem describes the current on every dipole in the array) can be found by integrating Equation 3.11 along this single basis function. This means that Equation 3.11 is a Green's Function which relates the electric field to the currents from the dipoles of the infinite array. As mentioned previously, these currents of the infinite number of elements are represented compactly as a single equation (Equation 3.5). These currents are broken down further into a finite number of basis functions per dipole and each one of these basis functions is called as a Floquet mode. Therefore, all of the currents for every element in the infinite array can be described using this finite set of modes. The field contribution from each mode is found through the convolution of the mode current distribution with the Green's Function of Equation 3.11. Again the basis function is defined in Equation 3.5. The result of this integration of Equation 3.11 is an expression for the Electric Field given by:

$$\bar{E}_s(\bar{R}) = -\frac{ZI_{so}}{4D_z} \sum_{n=-\infty}^{\infty} \int ds I(s) e^{-j\beta r_z(z-z')} \cdot \bar{K}_n(\beta, x, y; x', y', \hat{p}) \quad (3.12)$$

where \overline{K}_n is the kernel given by the Green's Function of Equation 3.11 and s indicates the expansion mode for which the field is being calculated. Equation 3.12 is used to calculate the far-field pattern for the array.

For the calculations of the mutual coupling between array elements using the near-zone E-field, the expansion into Floquet modes is not used in SPLAT. Instead a closed form expression for the electric field from a single dipole using the current distribution definition of Equation 3.5 is used. The expression is found by considering the field from each monopole segment separately yielding [13]:

$$\begin{aligned} \overline{E}^{(a)} = \frac{ZI_0}{4\pi \sinh \gamma l^{(a)}} & \left\{ \frac{\hat{R}_0 - \hat{p}^{(a)}(\hat{R}_0 \cdot \hat{p}^{(a)})}{R_0[1 - (\hat{R}_0 \cdot \hat{p}^{(a)})^2]} [\sinh \gamma l^{(a)} e^{-\gamma R_0} \right. \\ & + (\hat{R}_0 \cdot \hat{p}^{(a)}) \cosh \gamma l^{(a)} e^{-\gamma R_0} - (\hat{R}_a \cdot \hat{p}^{(a)}) e^{-\gamma R_a}] \\ & \left. + \hat{p}^{(a)} \left[\frac{e^{-\gamma R_a}}{R_a} - \cosh \gamma l^{(a)} \frac{e^{-\gamma R_0}}{R_0} \right] \right\} - \hat{R}_0 \frac{ZI_0}{4\pi} \frac{e^{-\gamma R_0}}{R_0} \left(1 + \frac{1}{\gamma R_0} \right) \end{aligned} \quad (3.13)$$

In Equation 3.13, the unit vector \hat{R}_0 points from the terminal of the dipole to the observer location, \hat{R}_a points from the tip of the a -monopole to the observer and \hat{p} is the direction of current flow on the a -monopole segment. R_0 and R_a are the distances from the terminal to the observer, and the tip of the a -monopole to the observer respectively. An equivalent expression can be written for the b -monopole segment of the dipole. Using Equation 3.13 the fields from the individual elements in the array are added together to find the value of the field at the observation location. SPLAT incorporates several acceleration routines to cause the summations in the near-field calculations to converge faster [13], [8].

3.2.5.3 *Thin-Wire Method-of-Moments.*

The final portion of the description of SPLAT in this chapter is an overview of how SPLAT solves for the unknown array currents using the method-of-moments. The approach behind the method-of-moments technique is to first model the problem by defining a

response function (u), an excitation function (f), and an operator or kernel describing the system (L) [18] given by:

$$Lu = f \quad (3.14)$$

For the scattering problem in a SPLAT simulation, the kernel is the Green's Function for an infinite column array given in Equation 3.12, or the closed-form expression for the fields from a single dipole in Equation 3.13. The excitation functions are either an incident-wave impinging on the array, or the voltages that are impressed at the terminals of the dipoles in the array as is the case in this study. The unknowns are the currents which correspond to the response function in the problem.

Next, the problem is discretized by expanding the unknown currents that form the response function into a set of basis functions with unknown coefficients. These basis functions are the normalized sinusoidal functions given in Equation 3.4, which are the Floquet modes for an infinite column array that span the length of the dipole. Therefore, the unknowns now are the coefficients that weight these sinusoidal basis functions represented by Equation 3.6. The discretized set of currents that approximate the actual currents is represented by \hat{u} in the system model:

$$L\hat{u} \simeq f \quad (3.15)$$

The residual error after the discretization is defined as:

$$L\hat{u} - f \triangleq r \quad (3.16)$$

The next step is to define the excitation and enforce the boundary conditions on the scatterer. In SPLAT's thin-wire method of moments formulation, the scattering problem is modeled using the Surface Equivalence Principle by replacing the wires of the antenna by

equivalent electric and magnetic surface current densities. The equivalent surface current densities are given by

$$\vec{J}_s^{eq} = \sum_{k=1}^N \frac{I_k}{2\pi a_k} \vec{F}_k^e(l'), \quad \text{and} \quad \vec{M}_s^{eq} = \sum_{k=1}^N \frac{Z_{s,n} I_n}{2\pi a_k} \vec{F}_k^e(l') \quad (3.17)$$

where the index k refers to the mode k , I_k represents the unknown current (the weighting coefficient for the current basis function), a_k is the radius of the dipole, and $\vec{F}_k^e(l')$ are the basis functions given by Equation 3.4. The magnetic surface currents are related to the electric surface currents through the surface impedance Z_s . These equivalent currents radiate the scattered field exterior to the wires and the negative of the incident fields interior to the wire [13]. The condition to be enforced in the scattering problem is to ensure that the total field inside of the wire is equal to zero, i.e:

$$\vec{E} = \vec{E}^{inc} + \vec{E}^s = 0 \quad (3.18)$$

Using the equivalent surface currents, the scattered field is represented as the superposition of the radiated fields from the individual basis function currents. Equation 3.12 or Equation 3.13 are used for \vec{E} , yielding:

$$\vec{E}^s = \vec{E}(\vec{J}_s^{eq}; \vec{r}') + \vec{E}(\vec{M}_s^{eq}; \vec{r}') = 0 \quad (3.19)$$

$$\vec{E}^s = \vec{E}\left(\sum_{n=1}^N \frac{I_n}{2\pi a_n} \vec{F}_n^e; \vec{r}'\right) + \vec{E}\left(\sum_{n=1}^N \frac{Z_{s,n} I_n}{2\pi a_n} \vec{F}_n^e; \vec{r}'\right) = 0 \quad (3.20)$$

$$\vec{E}^s = \sum_{n=1}^N I_n \left[\vec{E}\left(\frac{\vec{F}_n^e}{2\pi a_n}; \vec{r}'\right) + \vec{E}\left(\frac{Z_{s,n} \vec{F}_n^e}{2\pi a_n}; \vec{r}'\right) \right] = 0 \quad (3.21)$$

At this point in the problem formulation, there are N unknowns representing the N modes or basis functions that were used to discretize the unknown currents. While N number of equations could be generated by trying to enforce the boundary condition at N different points along the wire, the more accurate method-of-moments technique is to simultaneously generate the N number of equations by minimizing the residual error, r . This is done by forcing an orthogonality condition between the residual error and a set of testing functions across the entire problem domain using the inner product definition:

$$0 = \langle t_m, L\hat{u} - f \rangle \quad (3.22)$$

$$\langle t_m, L\hat{u} \rangle = \langle t_m, f \rangle \quad (3.23)$$

Using Galerkin's method the testing functions are of the same form as the basis functions $\bar{F}_k(l')$ [18] so the inner product of Equation 3.23, is computed on Equation 3.18 as:

$$\begin{aligned} \bar{E}|_{\text{inside wire}} &= 0 \\ \int \bar{E} \cdot \bar{F}_k dl' &= \int \bar{F}_k \cdot 0 dl' \end{aligned} \quad (3.24)$$

$$\int \bar{E} \cdot \bar{F}_k dl' = 0; \text{ and } \bar{E} = \bar{E}^{inc} + \bar{E}^s$$

$$\int \bar{E} \cdot \bar{F}_k dl' = \int (\bar{E}^{inc} + \bar{E}^s) \cdot \bar{F}_k dl' = 0 \quad (3.25)$$

$$\int \left(\bar{E}^{inc} + \sum_{n=1}^N I_n \left[\bar{E} \left(\frac{\bar{F}_n^e}{2\pi a_n}; \vec{r}' \right) + \bar{E} \left(\frac{Z_{s,n} \bar{F}_n^e}{2\pi a_n}; \vec{r}' \right) \right] \right) \cdot \bar{F}_k dl' = 0 \quad (3.26)$$

$$\int (\bar{E}^{inc}) \cdot \bar{F}_k dl' = - \int \left(\sum_{n=1}^N I_n \left[\bar{E} \left(\frac{\bar{F}_n^e}{2\pi a_n}; \vec{r}' \right) + \bar{E} \left(\frac{Z_{s,n} \bar{F}_n^e}{2\pi a_n}; \vec{r}' \right) \right] \right) \cdot \bar{F}_k dl' \quad (3.27)$$

Equation 3.27 generates the sufficient number of equations necessary to solve for the N unknowns in the scattering problem. These are the N unknown current coefficients I_n that

weight the N Floquet mode currents on the dipoles in the array. Equation 3.26 can be decomposed into a voltage vector and an impedance matrix:

$$V_k = \int \left(\bar{E}^{inc} \right) \cdot \bar{F}_k(l') dl' \quad (3.28)$$

$$Z_{k,n} = - \int \bar{E} \left(\frac{\bar{F}_n^e}{2\pi a_n}; \bar{r}' \right) \cdot \bar{F}_k(l') dl' + \bar{E} \left(\frac{Z_{s,n} \bar{F}_n^e}{2\pi a_n}; \bar{r}' \right) \cdot \bar{F}_k(l') dl' \quad (3.29)$$

$$V_k = Z_{k1}I_1 + Z_{k2}I_2 + \dots + Z_{kN}I_N \rightarrow \mathbf{V} = \bar{\bar{Z}}\mathbf{I} \quad (3.30)$$

$$\mathbf{V} = \begin{bmatrix} V_1, V_2, \dots, V_N \end{bmatrix}^T, \quad \mathbf{I} = \begin{bmatrix} I_1, I_2, \dots, I_N \end{bmatrix}^T, \quad \bar{\bar{Z}} = \begin{bmatrix} Z_{11} & Z_{12} & \dots & Z_{1N} \\ Z_{21} & Z_{22} & \dots & Z_{2N} \\ \vdots & \vdots & \ddots & \vdots \\ Z_{N1} & Z_{N2} & \dots & Z_{NN} \end{bmatrix} \quad (3.31)$$

With the voltage vector known for the given problem and the impedance matrix filled by Equation 3.29, the vector of unknown complex current coefficients can then be solved. For the particular SPLAT simulations run in the parametric study performed in this research, the vector of voltages was supplied using the Voltage Vector Input file.

3.3 Stepped Transmission Line Wide-band Matching

An example of the terminal impedances plotted on a Smith Chart for one of the collinear array configurations is shown in Figure 3.6. Constant VSWR values are represented graphically as circles centered at $Z = 1.0 + j0.0\Omega$ on the Smith Chart. The dotted circle in blue is the circle of impedance values that correspond to a VSWR of 2 as defined by Equation 3.2.

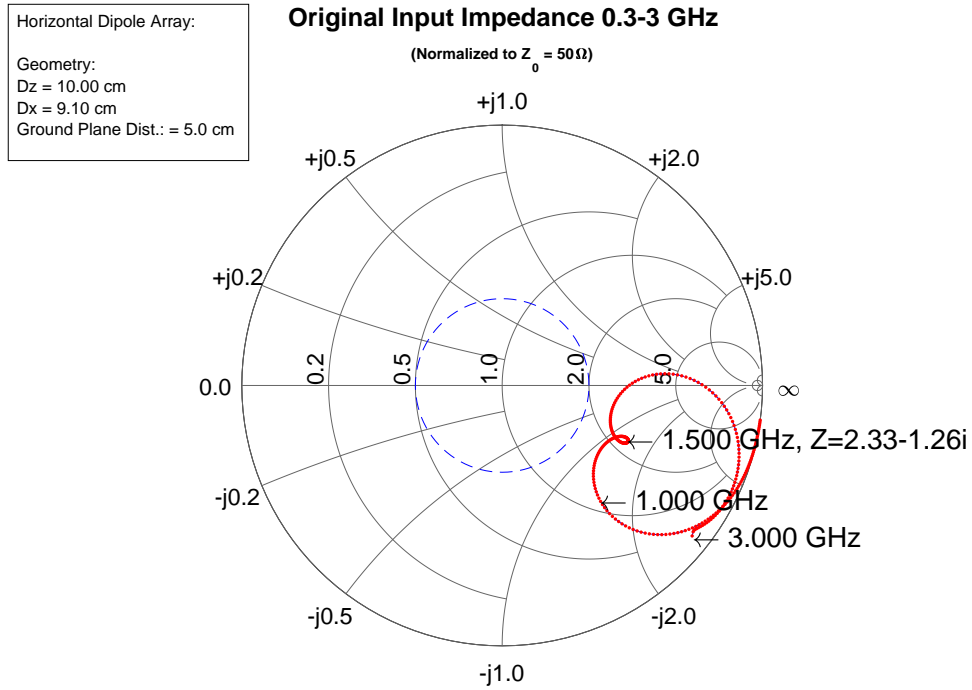


Figure 3.6: Terminal impedances plotted on Smith Chart

At a VSWR of 2, the reflection coefficient Γ between the terminals of the antenna and the 50Ω transmission line from the generator is equal to $1/3$ by Equation 3.1. This value of Γ corresponds to a reflected power loss at the terminals of the dipole of 11.1%. A VSWR of 2 is generally regarded as a good match between the antenna and the transmission line and serves as the criteria for determining the impedance bandwidth in this study. Since the Smith Chart is a polar plot of normalized impedances, the value of $Z = 1.0 + j0.0\Omega$ at the center of Figure 3.6 represents a true unnormalized impedance of 50Ω . The characteristic

impedance Z_0 of the transmission line from the generator to the terminals of the dipoles used in this study is purely real and has a value of 50Ω . Therefore, a normalized terminal impedance of $Z_L = 1.0 + j0.0\Omega$ provides a perfect conjugate match between the impedance of the line and the impedance of the load. At this location of Z_L at the center of the Smith Chart, the VSWR is equal to 1, and no power is reflected back from the dipole towards the generator.

As seen in Figure 3.6, although the terminal impedances for the frequencies around the L-band are clustered together fairly closely to $Z_L|_{1.5 \text{ GHz}}$, these impedance values lie outside of the VSWR of 2 circle. The goal of wide-band impedance matching is to bring as much of this impedance curve in towards the center of the Smith Chart as possible. In this case, the objective was to bring the VSWR below 2 for the L-band set of frequencies.

3.3.1 *Single-Stage Stepped-Transmission Line Matching.*

The wide-band matching technique used to transform the driving point impedances seen at the terminals of the dipole is the stepped transmission line matching technique. This technique as described in [5] uses sections of transmission line with different characteristic impedances placed in series between the 50Ω line from the generator and the dipole terminals. These different segments of transmission line transform the terminal impedances and change the reflection coefficient Γ between the segment junctions. The result is that the matching network moves the impedance curve towards the center of the Smith Chart. The single-stage stepped-transmission line matching network is depicted in Figure 3.7a. The impedance transformation seen between the voltage and current waveforms as they travel through a length of transmission line is dictated by the transmission line equation [19]:

$$Z_1 = Z_{01} \frac{Z_L + jZ_{01} \tan \beta L_1}{Z_{01} + jZ_L \tan \beta L_1} \quad (3.32)$$

In Equation 3.32, Z_L is the input impedance seen directly at the terminals of the dipoles, Z_{01} is the characteristic impedance of the transmission line inserted between the terminals of the dipole, and the 50Ω feedline, β is the propagation constant of the Z_{01} line, and L_1 is the length of the inserted Z_{01} transmission line.

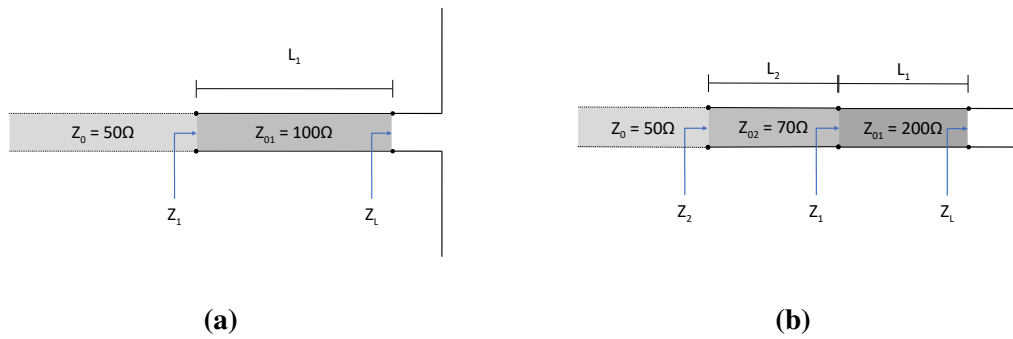


Figure 3.7: (a) Single-stage stepped transmission line matching at dipole terminals. (b) Dual-stage stepped transmission line matching at dipole terminals.

The result of applying Equation 3.32 is a clockwise rotation (direction towards the generator) around the Smith Chart which transforms the original input impedance Z_L into Z_1 . If Z_{01} was equal to Z_0 , then the transformed impedance Z_1 would have the same Γ and VSWR values as the original input impedance Z_L . In this case, Equation 3.32 simply describes the value of the impedance as it rotates on a constant VSWR circle on the Smith Chart as the signal moves down the 50Ω feedline through the length L_1 . The transformed input impedance Z_1 will have rotated around the Smith Chart on its original VSWR circle through a rotation angle corresponding to the length of L_1 . After traveling $\lambda/2$ down the 50Ω transmission line, Z_1 would again equal Z_L with no change to the reflection coefficient or the VSWR.

However, if the inserted section of transmission line has characteristic impedance Z_{01} that does not equal Z_0 as depicted in Figure 3.7a, then the input impedance Z_L and the reflection coefficient seen at the junction between the Z_{01} line and the dipole terminals

would instead be plotted on a Smith Chart normalized to Z_{01} as shown in Figure 3.8b. The Z_L impedances plotted on this Smith Chart normalized to Z_{01} describes the reflection coefficient between the antenna terminals and the beginning of the Z_{01} line.

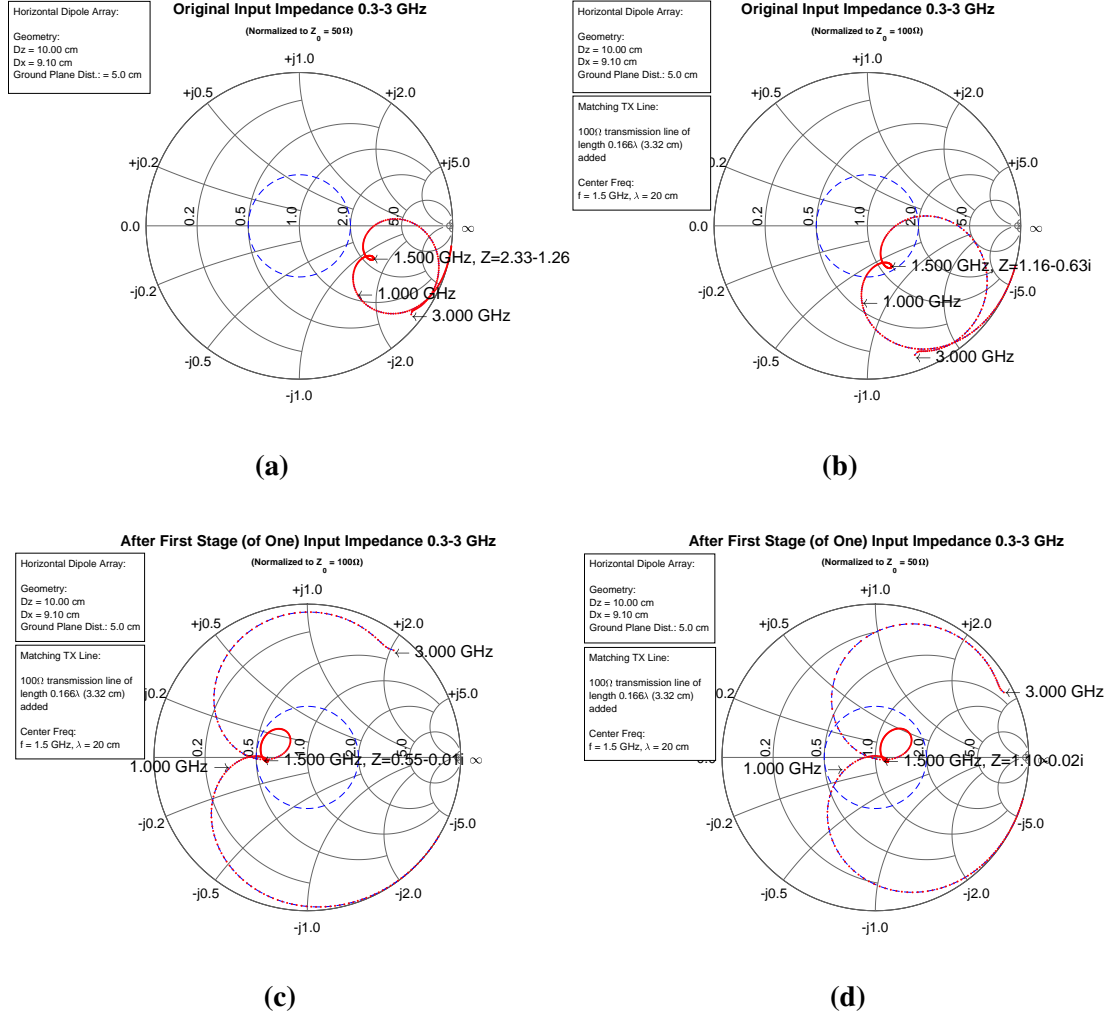


Figure 3.8: (a) Terminal impedances normalized to $Z_0 = 50\Omega$ (b) Terminal impedances normalized to $Z_{01} = 100\Omega$ (c) Transformed impedances normalized to $Z_{01} = 100\Omega$ (d) Transformed impedances normalized to $Z_0 = 50\Omega$

Equation 3.32 again describes the impedance transformation that take place as the voltage and current waves move down the L_1 length of Z_{01} line. The resulting impedance

transformation after moving through the Z_{01} line is shown in Figure 3.8c. As seen in this figure, Z_L for the center frequency has now been transformed to the real axis to an impedance value of $Z_L = 0.5 + j0.0$. The rest of the impedance curve has also rotated clockwise towards the generator although Z_L for each frequency experiences a different amount of rotation based on Equation 3.32. (*Note that β also changes with λ .)

Finally, after traveling down the Z_{01} line through the length L_1 , the voltage and current waves encounter the $Z_0 = 50\Omega$ line which connects the network the rest of the way back to the generator. In order to describe the reflection coefficient between the end of the Z_{01} line and the start of the Z_0 line, the value of the impedances at the end of the Z_{01} line are plotted on a Smith Chart normalized to $Z_0 = 50\Omega$ as shown in Figure 3.8d.

By carefully choosing the length of the Z_{01} line and the characteristic impedance of this segment, the terminal impedances have been transformed and much of the impedance curve has been brought inside of the VSWR of 2 circle as seen by comparing Figure 3.8a and Figure 3.8d. For the single-stage stepped-transmission line matching technique, the general approach was to focus on the impedance at the center frequency of 1.5 GHz and add the appropriate length of Z_{01} line to bring it into the center of the Smith Chart for a perfect conjugate match. The amount of line necessary to produce the desired rotation can be obtained from reading the corresponding distance in wavelengths towards the generator as measured on the perimeter of the Smith Chart. In this example, the rotation of 119° of $Z_L|_{1.5 \text{ GHz}}$ from Figure 3.8b to Figure 3.8c corresponds to adding 0.166λ (or 3.32 cm) of 100Ω line.

As shown by Figure 3.8c, the impedances associated with the higher frequencies undergo a greater amount of rotation relative to the lower frequencies. The end effect is an undesirable unraveling of the impedance curve which spreads out the terminal impedances across the Smith Chart. This effect is exacerbated if the original impedance curve was not

tightly wound to begin with. For this reason, the goal of the parametric study was to find an array configuration that produced the tightest possible curve to minimize this unraveling.

3.3.2 Two-Stage Stepped-Transmission Line Matching.

The unraveling of the impedance curve through the impedance transformation can be partially mitigated by using multiple sections of transmission lines. A two-stage stepped-transmission line matching network accomplishes the impedance matching by staggering the impedance transformations across two sections of transmission line with different characteristic impedances. For this matching network, Equation 3.32 is then applied twice: first between the junction between the dipole terminals and the Z_{01} transmission line, and then between the Z_{01} and Z_{02} , transmission line. When Equation 3.32 is applied at the second junction, Z_L would be replaced with Z_{01} , Z_{01} would be replaced with Z_{02} and the length L_1 would be replaced by L_2 , which is the length of the Z_{02} transmission line. The propagation constant β is the value for the medium inside of the Z_{02} line.

The general approach for using the two-stage stepped-transmission line technique is to first rotate $Z_L|_{1.5 \text{ GHz}}$ onto the real axis of the Smith Chart using the first Z_{01} transmission line section. Then, if the second Z_{02} section of transmission line is a quarter-wavelength long, then Equation 3.32 is reduced to:

$$Z_2 = Z_{02} \frac{Z_{01} + jZ_{02} \tan \beta L_2}{Z_{02} + jZ_{01} \tan \beta L_2}; \quad L_2 = \lambda/4, \beta = 2\pi/\lambda \quad (3.33)$$

$$Z_2 = \frac{Z_{02}^2}{Z_1}; \quad (3.34)$$

Equation 3.34 represents a purely real transformation of the impedance Z_1 to Z_2 . If Z_2 can be set to 50Ω , then the second-stage has successfully transformed the normalized terminal impedance $Z_L|_{1.5 \text{ GHz}}$ to $1.0 + j0.0\Omega$ for perfect conjugate match with the 50Ω line. This impedance transformation process is visualized by sliding Z_1 on the real axis to the center

of the Smith Chart. The appropriate value of Z_{02} that is required to produce this purely real transformation which brings $Z_1|_{1.5GHz}$ to the center of the Smith Chart can be solved for by setting Z_2 equal to 50Ω in Equation 3.34, yielding:

$$Z_{02} = \sqrt{(Z_1|_{1.5GHz})(Z_2)}; \quad (3.35)$$

$Z_1|_{1.5GHz}$ is known from the output of Equation 3.32 applied after the first Z_{01} section of transmission line. For the crossed-dipole arrays investigated in this study, the added sections of transmission line had characteristic impedances limited to the values used in commonly available coaxial cables: 70Ω , 100Ω , and 200Ω . Figure 3.9 demonstrates the impedance transformation process using the two-stage stepped-transmission line technique.

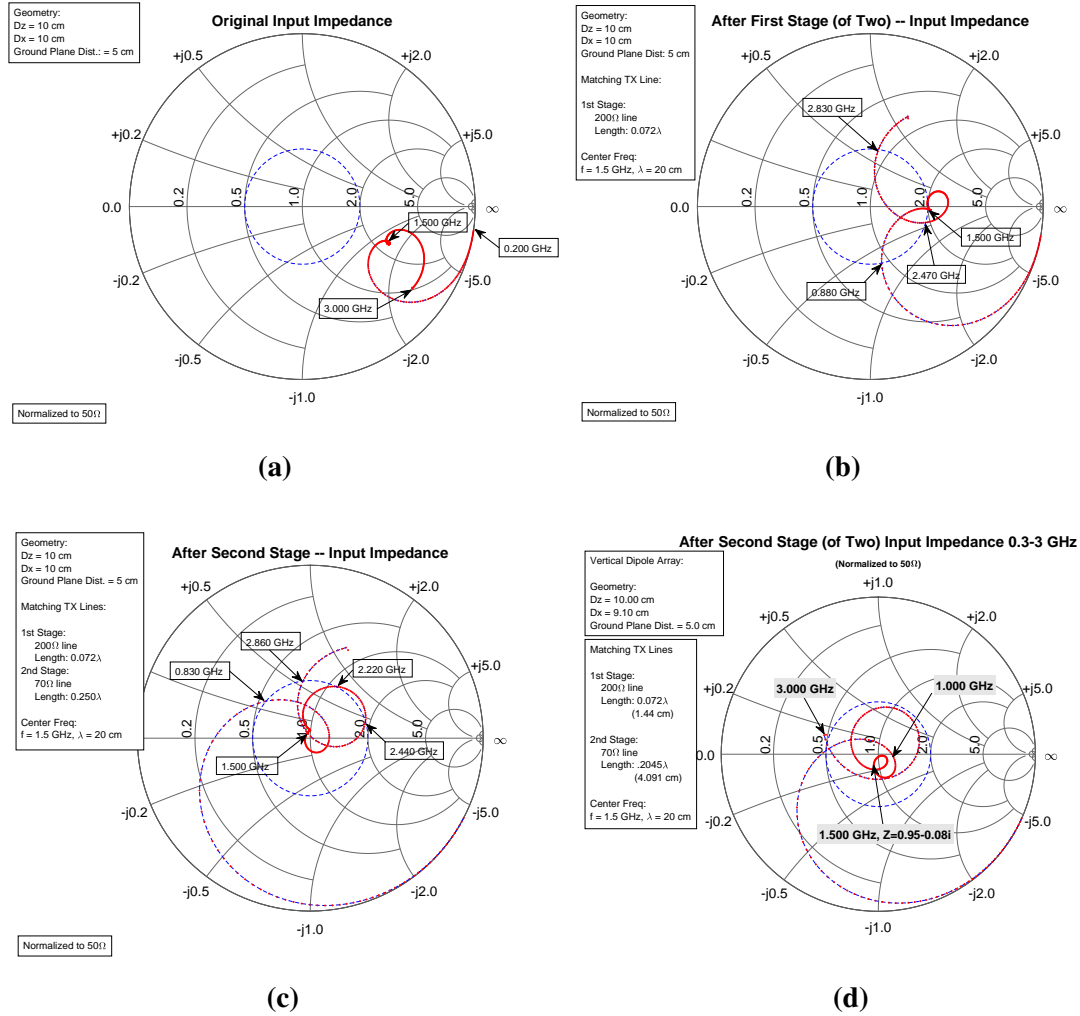


Figure 3.9: (a) Terminal impedances normalized to $Z_0 = 50\Omega$ (b) Terminal impedances after first section of transmission line (c) Terminal impedances after second quarter-wave section of transmission line (d) Terminal impedances after second section of transmission line with length slightly less than a quarter-wavelength

As shown in Figure 3.9c and Figure 3.9d, some fine tuning of the length of the added sections of transmission lines could be performed to try and bring more of the curve into the VSWR of 2 circle. To help this fine tuning process, a MATLAB script was written to observe the effect of finely varying the length of the transmission line using a Graphical User Interface (GUI). This script uses a slider to gradually adjust the length of the second transmission line. This script was also used for the single-stage matching technique to try make fine adjustments for that network as well. A screenshot of this GUI is shown in Figure 3.10.

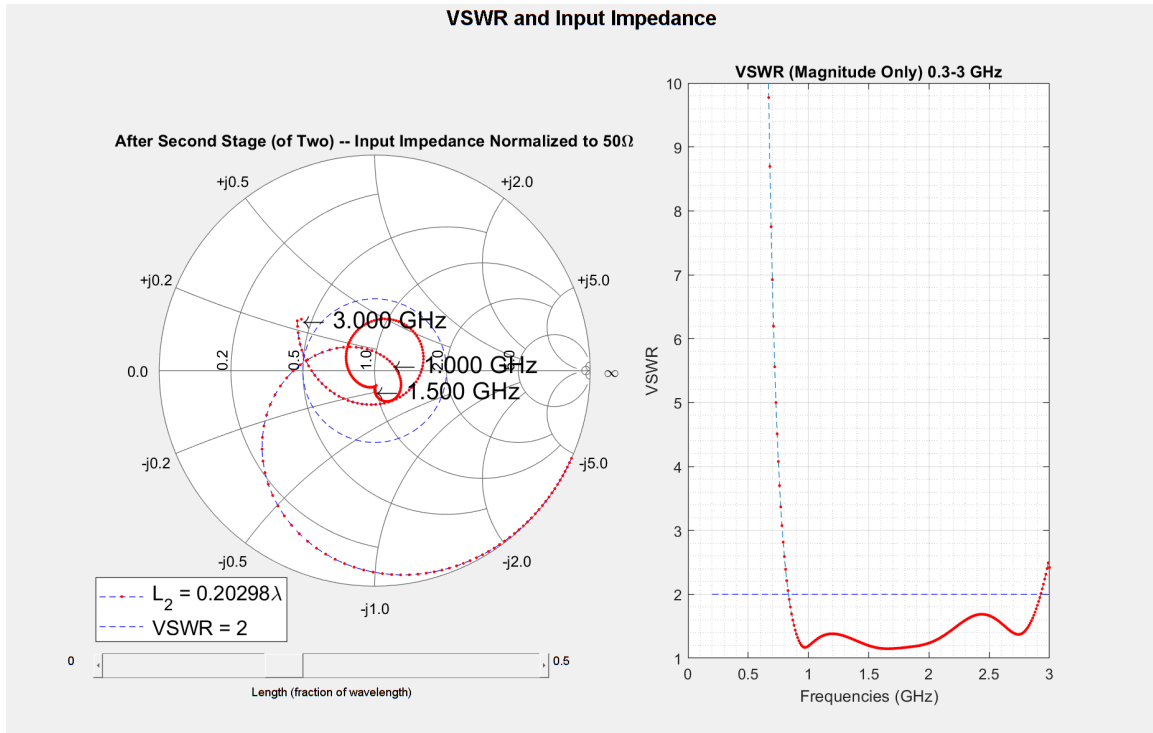


Figure 3.10: MATLAB GUI for fine tuning transmission line length

The wide-band matching was performed at the terminals of the reference dipoles for each of the infinite columns defined in SPLAT. The horizontal and vertical dipole arrays were simulated separately, and therefore, a separate wide-band matching network was designed for the dipole arrays in each orientation. This would be equivalent to attaching

separate matching networks for the two independently driven dipole ports at every crossed-dipole element on an actual physical implementation of the antenna. The coupling effect of the feedlines or the matching networks was limited to this level of fidelity and this study does not consider the behind the ground-plane part of the design problem. The stepped-transmission line wide-band matching portion of this study formed the final stage of the bandwidth optimization section.

3.4 Plotting the Array Currents and the Far-Field

As discussed in Section 3.2.5.1, SPLAT's method-of-moments routine solves for the coefficients of the sinusoidal expansion functions used to model the current on the dipole elements as depicted in Figure 3.5. These coefficients were used to weight the basis functions to reconstruct and plot the current distribution on the elements in the array as shown in Figure 3.11.

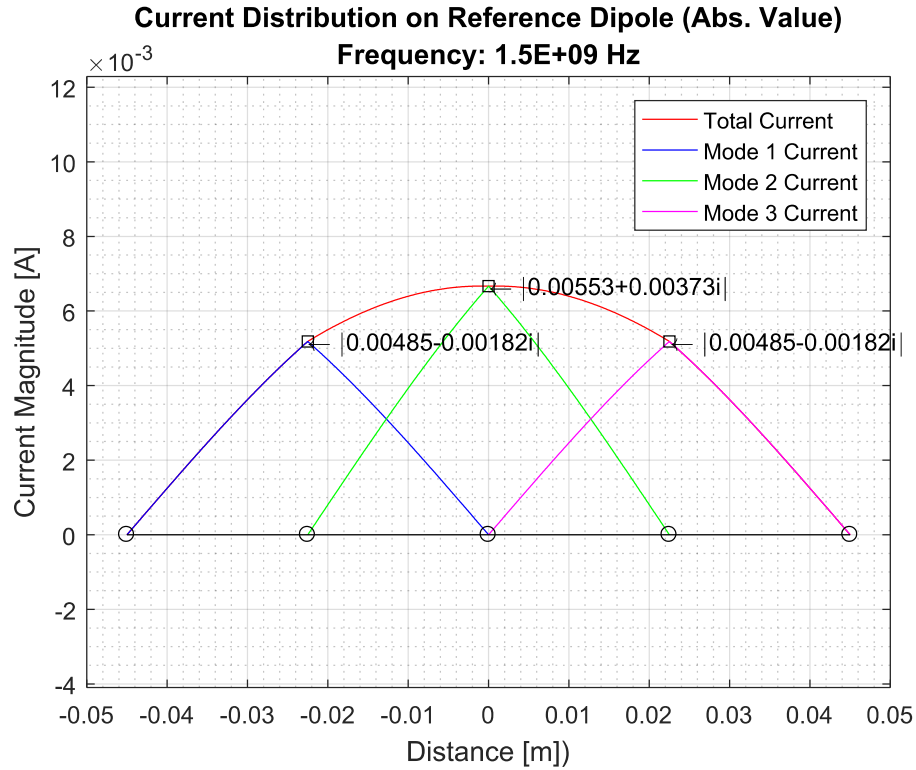


Figure 3.11: Current distribution reconstructed from weighted basis functions

Although the impedance curves on the Smith Chart show the variation in the terminal currents across the 0.3 GHz to 3.0 GHz frequency range, these current plots also show the changing current distribution across the length of the dipole element. The effect of mutual coupling between neighboring dipoles along the length of the element, especially in the finite-array dimension, can be seen once these currents are plotted.

The shape of the current distributions on the array elements also provides some physical insight in explaining the shape of the far-field patterns. SPLAT calculates the far-field values by applying Equation 3.12, which incorporates the element currents in the pattern function term. Therefore, a plot of the current distribution helps provide some visual indication of when strong side-lobes start appearing in the frequency range. The current and far-field plots help set limits on the pattern bandwidth, which is narrower than the impedance bandwidth found from the results of the parametric study, and the stepped-transmission line wide-band matching solution. The real, imaginary, and absolute value of the terminal currents were plotted for the various array configurations.

The azimuthal far-field patterns are produced by running SPLAT in bistatic pattern mode as described in Section 3.2.3. Since the image arrays simulate an infinite ground-plane behind the array, only the pattern in the region above the ground plane was kept from the results calculated by SPLAT. For the elevation patterns, the current distributions found in SPLAT as described in Section 3.2.5.1 were first exported to MATLAB. The far-field elevation pattern was calculated for the finite array shown in Figure 2.3 through pattern multiplication. The far-field for a single, horizontal dipole above an infinite ground-plane with the current distributions computed in SPLAT were calculated using the following equation from [7] for the element factor:

$$E = \left(j\eta \frac{kI_0 l e^{-j\beta r}}{4\pi r} \right) \sqrt{1 - \sin^2(\theta) \sin^2(\phi)} [2j \sin \beta h \cos \theta] \quad (3.36)$$

with h being the height above the ground plane. Equation 3.36 was then multiplied by the space factor calculated by numerically integrating the current distribution on the reference dipole found from SPLAT along the length of the dipole with the propagation term:

$$\int_{-l/2}^{l/2} I(z') e^{-j\beta z' \cos \theta} dz' \quad (3.37)$$

Finally, the array factor for the 28×2 array comprising the center two columns of the feed shown in Figure 2.3 was calculated using the following array factor equation:

$$AF = \sum_{n=1}^N \left[\sum_{m=1}^M (I_{1n} I_{m1}) e^{j(m-1)(\beta d_x \sin \theta \cos \phi + \beta_x)} \right] e^{j(m-1)(\beta d_x \sin \theta \cos \phi + \beta_x)} \quad (3.38)$$

Multiplying Equations 3.36, 3.37, and 3.38 yields the final pattern for the finite array using the currents calculated using SPLAT. Doing these pattern multiplication steps outside of SPLAT was necessary to generate the elevation pattern, since the elevation pattern for an infinite array would simply be a delta function in the direction normal to the array.

For the cases where the current distribution was not identical between the two columns, the far-field for the two reference dipoles was first calculated, then a single linear array factor (28×1 array factor) was applied. This was done by applying Equation 3.36 and Equation 3.37 separately for each reference dipole then summing the two products to get the total far-field. The resulting azimuthal and elevation patterns are shown in Section 4.4.2. All patterns are normalized to the peak value of the main-beam.

IV. Results and Analysis

4.1 Array Element Spacing - Parametric Study

The impedance curves calculated for the collinear array configurations specified in Table 3.1 are presented and analyzed in this section. The chart titles indicate for which column in the array the impedances were calculated. Column 1 is always the column lying in the $-x$ portion of the array, while Column 2 is always the column in the $+x$ portion of the array as shown in Figure 3.4a. For all collinear array configurations tested in this parametric study, the impedance values from Column 1 were identical to the impedance values from Column 2. Therefore, only the results for Column 1 are shown in this section. For convenience, Table 3.1 has been repeated here:

Table 4.1: Parametric Study table

Config. No.	Element Orientation	D_z	D_x	Ground Plane Dist.	Changing Spacing ¹	Direction of Change ²
Config. 1	Vertical	9.10 cm - 14.00 cm	10.00 cm	No Ground Plane	Tip-to-Tip	Infinite
Config. 2	Vertical	9.10 cm - 14.00 cm	10.00 cm	4.50 cm	Tip-to-Tip	Infinite
Config. 3	Vertical	10.00 cm	1.25 cm - 25.00 cm	No Ground Plane	Side-by-Side	Finite
Config. 4	Vertical	10.00 cm	1.25 cm - 25.00 cm	4.50 cm	Side-by-Side	Finite
Config. 5	Vertical	10.00 cm	10.00 cm	1.25 cm - 9.00 cm	Ground-Plane Dist.	—
Config. 6	Horizontal	1.10 cm - 9.00 cm	10.00 cm	4.50 cm	Side-by-Side	Infinite
Config. 7	Horizontal	10.00 cm	9.10 cm - 18.75 cm	4.50 cm	Tip-to-Tip	Finite
Config. 8	Horizontal	10.00 cm	10.00 cm	1.25 cm - 9.00 cm	Ground Plane Dist.	—

*Fixed parameters: dipole lengths = 9.0 cm, dipole radii = 0.5 cm, $\epsilon_r=1$, $\mu_r=1$

1: Refers to the type of spacing layout between dipole elements that is changing

2: Indicates whether the changing spacing is occurring in the infinite or finite array dimension

4.1.1 Vertical Elements of the Two-Column Collinear Array and Ground Plane Distance.

Figure 4.1 shows the results for the terminal impedances calculated for the first four configurations from Table 4.1:

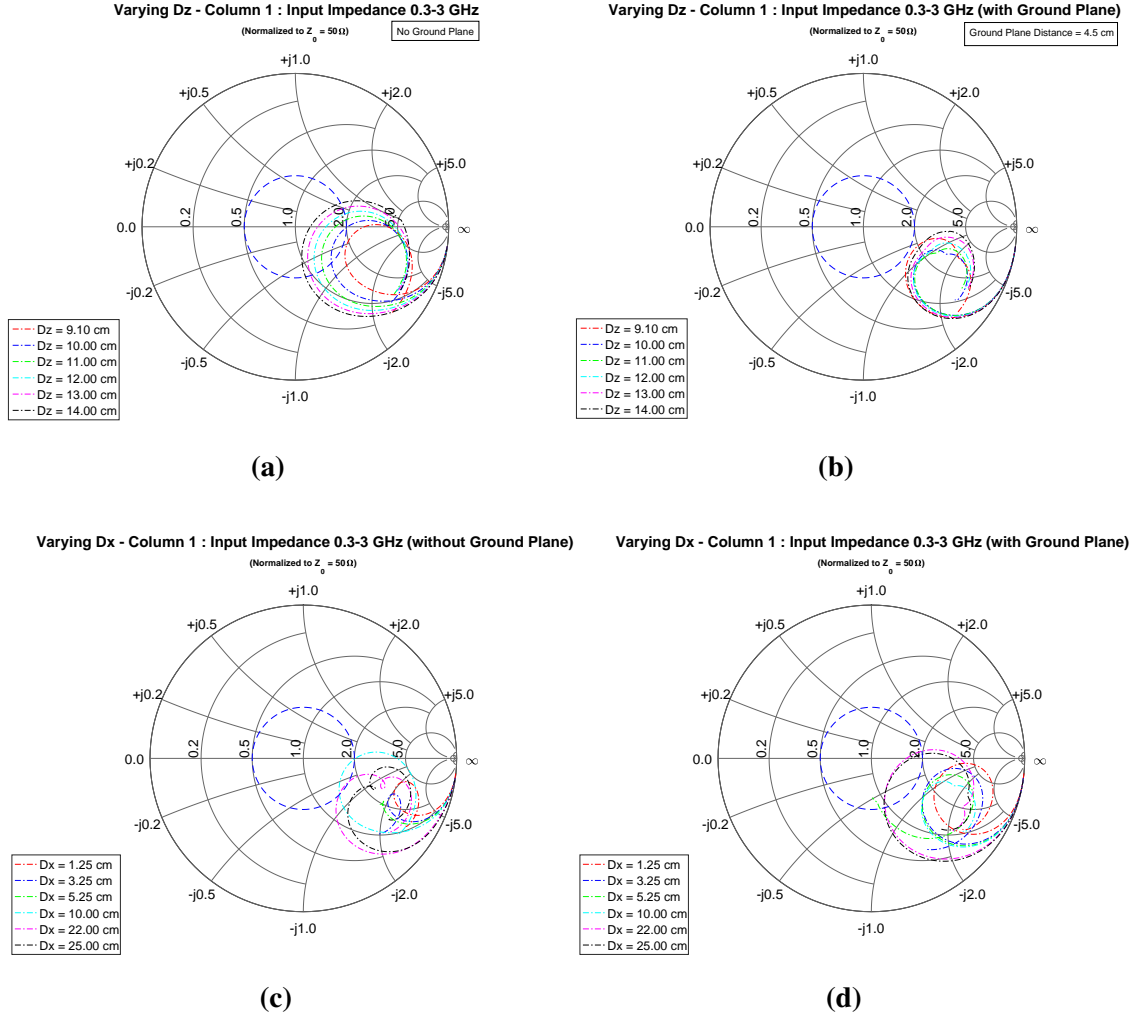


Figure 4.1: (a) Terminal impedances for Configuration 1 (b) Terminal impedances for Configuration 2 (c) Terminal impedances for Configuration 3 (d) Terminal impedances for Configuration 4

As shown in Figure 4.1a where the ground-plane was excluded, the progressively smaller tip-to-tip inter-element spacings for vertical elements in the infinite array direction causes the impedance curves to tighten considerably. The direction of change in the

impedance curves is towards the lower right-hand quadrant of the Smith Chart. This indicates that the impedance values are becoming more capacitive (imaginary component less than zero). The D_z spacing of 9.10 cm, which corresponds to a gap spacing of only 1 mm between adjacent dipoles in a vertical column, produces the largest terminal impedance values (in magnitude), and is the tightest curve for the array without a ground-plane.

For this simple two-column collinear array of vertically oriented dipoles, the change in the terminal impedance curves with the spacing D_z as shown in Figure 4.1a, can be explained using a 2-port network model for the two columns and Equation 4.1. This equation describes the mutual impedance $Z^{q',q}$ between a column array q and an external element q' , which is the reference dipole in the adjacent infinite column [5] i.e:

$$Z^{q',q} = \frac{\beta Z}{4D_z} \sum_{n=-\infty}^{\infty} e^{-j\beta(q'-q)r_z} r_\rho^2 P_z^{(q)} P_z^{q't} H_0^{(2)}(\beta r_\rho |\bar{\rho}' - \bar{\rho}|) \quad (4.1)$$

In Equation 4.1, r_z and r_ρ are distance variables defined by $r_z = s_z + n\frac{\lambda}{D_z}$ and $r_\rho = \sqrt{1 - r_z^2}$, where s_z is the \hat{z} component of the unit vector along the direction of excitation and the index n indicates the n -th element in the array. The $q' - q$ term in the complex exponential factor is the difference between the z -coordinates of the terminals of the reference dipoles between the two columns. Therefore, for the collinear array the complex exponential term disappears. The cylindrical coordinate vectors $\bar{\rho}$ and $\bar{\rho}'$ are the vectors traced from the origin to the reference element of the q and q' columns respectively. The impedance Z is equal to $\sqrt{\mu/\epsilon}$. The functions $P_z^{(q)}$ and $P_z^{q't}$ are the pattern factors for each column given by:

$$P_z^{(q)} = \frac{1}{I^{(q)}} \int_{-l}^l I^{(q)}(z'') e^{j\beta z'' r_z} dz'' \quad (4.2)$$

where the coordinate variable z'' exists along the length of the reference dipole for which the pattern is calculated. $I^{(q)}$ is the current distribution on the element q . The superscript t

indicates that the pattern factor of the reference element in the q' column is calculated by integrating the current distribution on the element when it is transmitting from its terminals.

As seen from the coefficient term outside the summation in Equation 4.1, the mutual impedance increases as the spacing D_z is decreased. This is the case for Configuration 1 of the parametric study outlined in Table 4.1. By considering the reference dipoles of Columns 1 and 2, the voltages and currents that exist on them, and by applying a two-port network model to describe this system, the relation between the impedances, currents, and voltages can be expressed as:

$$\begin{bmatrix} V^1 \\ V^2 \end{bmatrix} = \begin{bmatrix} Z^{1,1} & Z^{1,2} \\ Z^{2,1} & Z^{2,2} \end{bmatrix} \begin{bmatrix} I^1 \\ I^2 \end{bmatrix}, \text{ or: } \begin{aligned} V^1 &= Z^{1,1}I^1 + Z^{1,2}I^2 \\ V^2 &= Z^{2,1}I^1 + Z^{2,2}I^2 \end{aligned} \quad (4.3)$$

V^1 and V^2 are the voltages impressed at the terminals of each respective reference dipole, the $Z^{m,n}$ terms are the self and mutual-impedance values calculated by Equation 4.1, and the I^1 and I^2 values are the currents at the terminals of the reference dipoles. The driving point impedances for each terminal which are plotted on the Smith Chart are defined as V^1/I^1 and V^2/I^2 , i.e:

$$\begin{aligned} Z_{1D} &= \frac{V_1}{I_1} = Z_{1,1} + Z_{1,2} \frac{I_1}{I_2} \\ Z_{2D} &= \frac{V_2}{I_2} = Z_{1,1} + Z_{1,2} \frac{I_1}{I_2} \end{aligned} \quad (4.4)$$

As the mutual impedances increase by applying smaller D_z spacings in Equation 4.1, the driving point terminal impedances in Equation 4.4 should also increase in magnitude. This is confirmed in the data shown in Figure 4.1a. As the impedance curves move towards the right-hand side of the Smith Chart, they take on the larger normalized reactance and resistance values that are plotted in this region. Therefore, as the inter-element spacing D_z is decreased between SPLAT simulations, the magnitude of the terminal impedances shown in Figure 4.1a increase in accordance with Equation 4.1 and Equation 4.4.

Additionally, the symmetry of the geometry and the symmetry of the coupling matrix in the two-port network equation explains the identical terminal impedances seen at the terminals of the reference dipoles in Columns 1 and 2.

The results for the parametric study on the horizontal spacing between the vertical array elements in Configuration 3 can be explained using the same mutual impedance and coupling matrix equations. In this case, the changing horizontal spacing D_x , which moves the columns either farther or closer apart, affects the argument of the Hankel function inside of the summation in Equation 4.1. As the two columns are brought closer together by decreasing D_x , the argument of the Hankel function decreases. Since the amplitude of the Hankel function decays as $\sim x^{-1/2}$, where x is the argument of the Hankel function, the magnitude of each term of the summation in Equation 4.1 increases as the columns are brought closer together. Therefore, again the driving point impedance curves increase in magnitude as the column spacing is decreased as shown in Figure 4.1c.

Large normalized impedances are plotted on the region of the (impedance) Smith Chart concentrated near the $Z = \infty$ point on the right-hand side of the outermost $|\Gamma| = 1$ circle. Therefore, the increasing magnitude of the terminal impedances caused by the decreasing element spacing makes the impedance curves appear to cluster tightly together in that region. Therefore, the denser dipole arrays produce tighter, and more capacitive impedance curves when plotted on the Smith Chart.

A mutual impedance equation similar to Equation 4.1 that describes the coupling between array elements oriented in the horizontal direction is derived in Chapter 3, Section 3.4 of [5]. A similar explanation as the one provided above could be made for the results from the parametric study on the horizontal element arrays using this equation. However, the principle is the same in that the closer spacing produces tighter curves of higher impedance values. Therefore, this type of analysis will not be repeated. Instead the results for the remainder of the parametric study will be addressed qualitatively, since the other

major reason for conducting the study was to find an optimal array geometry for wide-band matching.

4.1.1.1 Vertical Dipole Array Ground Plane Distance Results.

As seen by comparing Figure 4.1a and Figure 4.1b the addition of a ground-plane reduces the size of the impedance curves and causes the terminal impedances to become more capacitive and larger in magnitude overall. The transformation of the impedance curves after including the ground plane is more pronounced for the array configurations with greater D_z spacing. The effect that the ground plane has on the terminal impedances can be explained by modeling the ground plane using Image Theory as was discussed in Section 3.2.4. Then, the mutual impedance relation given in Equation 4.1 can be extended to the two image columns. The negative voltages and negative currents of the image columns can be incorporated into Equation 4.3 to form a system of four equations describing the four terminal voltages, terminal currents, and mutual impedances between the reference dipoles of each column.

The mutual impedance equation can be used to calculate the $Z^{1,1}$, $Z^{1,2}$, $Z^{1,3}$, $Z^{1,4}$ etc. impedances to produce a 4x4 coupling matrix that takes into account the two real columns and the two image columns. This is how SPLAT solves for the array currents in the method-of-moments routine, except that the coupling matrix is 12x12 because each reference dipole's current is modeled by three modes or basis functions.

As shown in Figure 4.1b and Figure 4.1d, with the ground-plane present the trend of tighter impedance curves with smaller D_z spacing no longer strictly holds true. Although including the ground plane helps produce tighter impedance curves overall, within the family of curves shown in Figure 4.1b, the curves for a D_z spacing of 11.00 cm and 10.00 cm actually produce tighter curves than the spacing at 9.10 cm.

The real and imaginary components of the terminal impedances were investigated in more detail to try and better examine the effect of including the ground-plane. Figure 4.2 plots the resistance and reactance for the arrays of Configurations 1 and 2 separately.

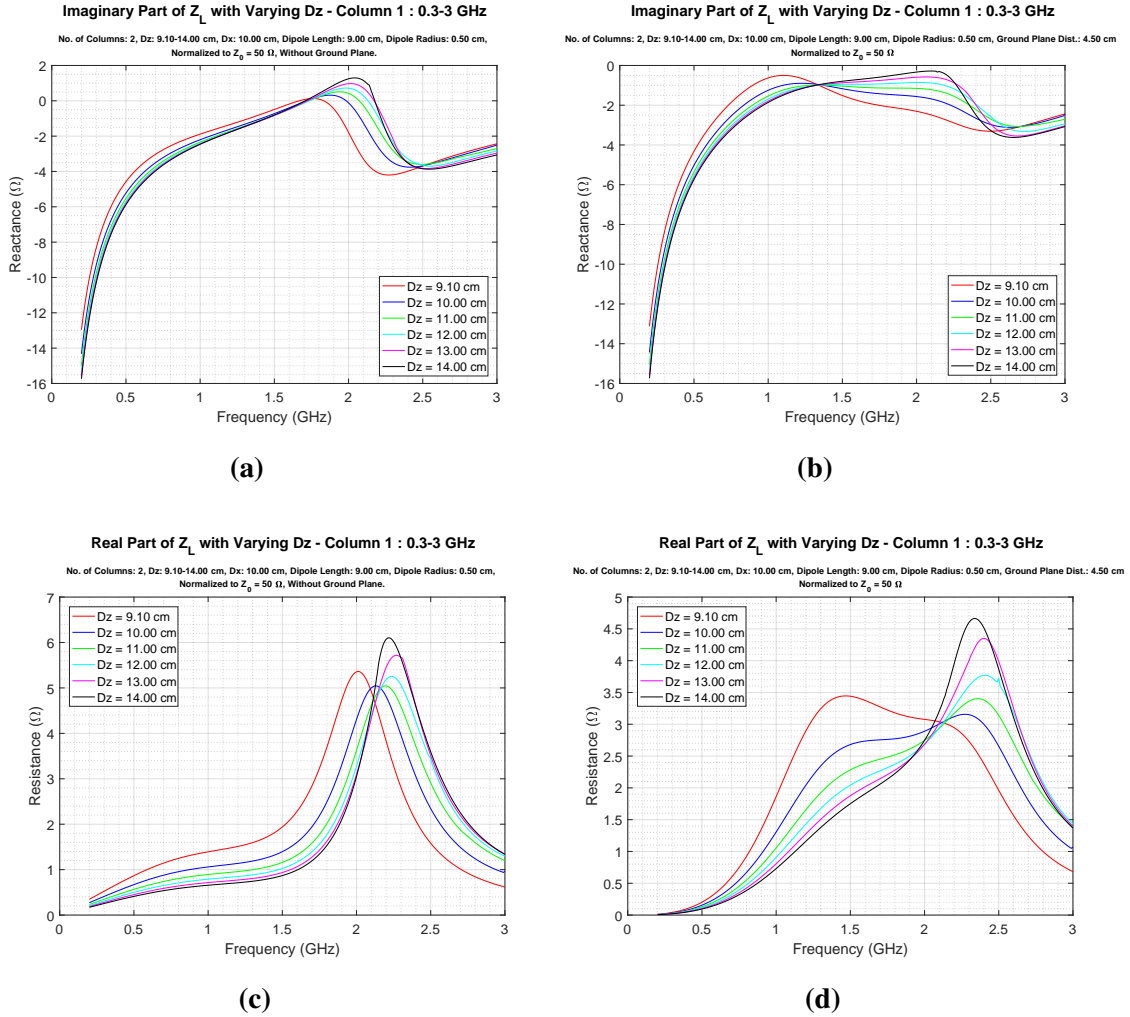


Figure 4.2: (a) Imaginary component of terminal impedances for Configuration 1. (b) Imaginary component of terminal impedances for Configuration 2. (c) Real component of terminal impedances for Configuration 1. (d) Real component of terminal impedances for Configuration 2.

With the included ground-plane, the impedances for the vertical elements of the collinear array become completely capacitive across the entire 0.3 GHz to 3.0 GHz frequency range. For the impedances plotted for Configuration 1 in 4.1a, the reactance across the differing geometries stay fairly constant except for in the window between 1.8 GHz to 2.3 GHz as shown in Figure 4.2a. In this window, changing the array geometry causes the reactance to vary greatly from configuration to configuration. When the ground-plane is added, the range of where this phenomenon occurs is extended to around 1.3 GHz to 2.5 GHz as shown in Figure 4.2b. However, the magnitude of the change is reduced. After about 1 GHz, the ground-plane helps keep the terminal impedances relatively constant across the 0.3 GHz to 3.0 GHz frequency range.

This leveling off of the terminal reactances is even more pronounced for the side-by-side spacing changes of Configurations 3 and 4. The normalized reactances for these configurations are shown in Figure 4.3:

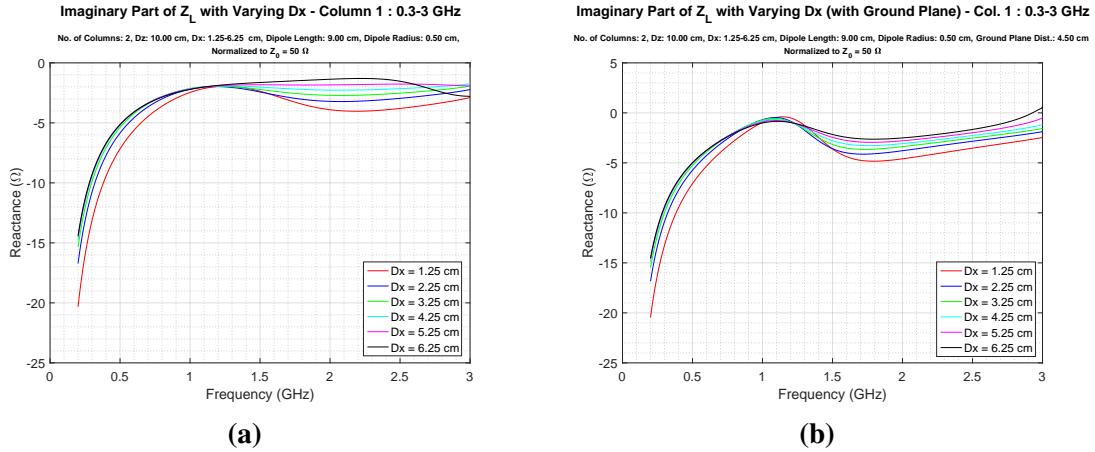


Figure 4.3: (a) Normalized reactances for Configuration 3. (b) Normalized reactances for Configuration 4.

These reactance plots help explain the tightly clustered curves for the small values of D_x in Figure 4.1c and Figure 4.1d. The curve for $D_x = 1.25\text{cm}$ has the most negative reactance for the majority of the frequency range. As mentioned in Section 3.3, these tighter

curves are the most advantageous for performing wideband matching. Unfortunately, these tighter D_x spacings cannot be realized with the collinear crossed dipole array without the vertical dipole elements touching.

The effect of changing the ground-plane distance itself is shown in Figure 4.4. The tightest impedance curves occur when the ground-plane distance is close to a quarter-wavelength at the resonant frequency of the individual dipole elements. For this reason, the ground-plane distances of 4.5 cm and 5.0 cm were chosen throughout the parametric study.

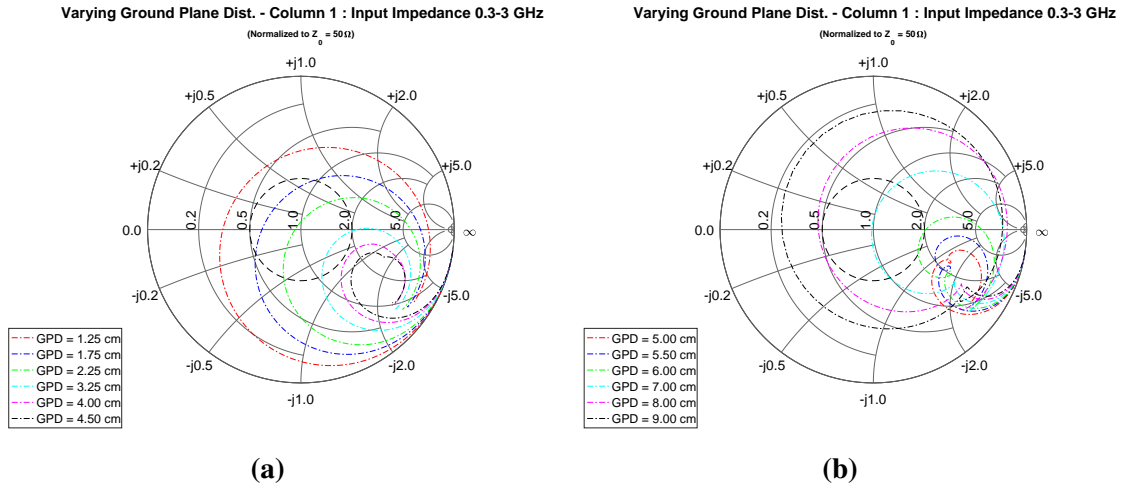


Figure 4.4: (a) Terminal impedances for Configuration 5 (Ground-Plane Distance varying from 1.25 cm to 4.50 cm) (b) Terminal impedances for Configuration 5 (Ground Plane Distance varying from 5.00 cm to 9.00 cm)

The results presented so far conclude the parametric study on the vertically oriented dipole elements for the two-column collinear array. From these results, it was determined that a D_z spacing of 10.00 cm, a D_x spacing of 9.10 cm (about as close as possible without horizontal elements touching), and a ground plane distance of 5.0 cm would provide the best set of terminal impedance curves for wide-band matching for the vertical elements in the array.

4.1.2 Horizontal Elements of the Two-Column Collinear Array.

Figure 4.5 shows the impedance curves for the parametric study conducted on the horizontal dipole elements in the two-column collinear array as specified by Configurations 6 and 7 in Table 4.1:

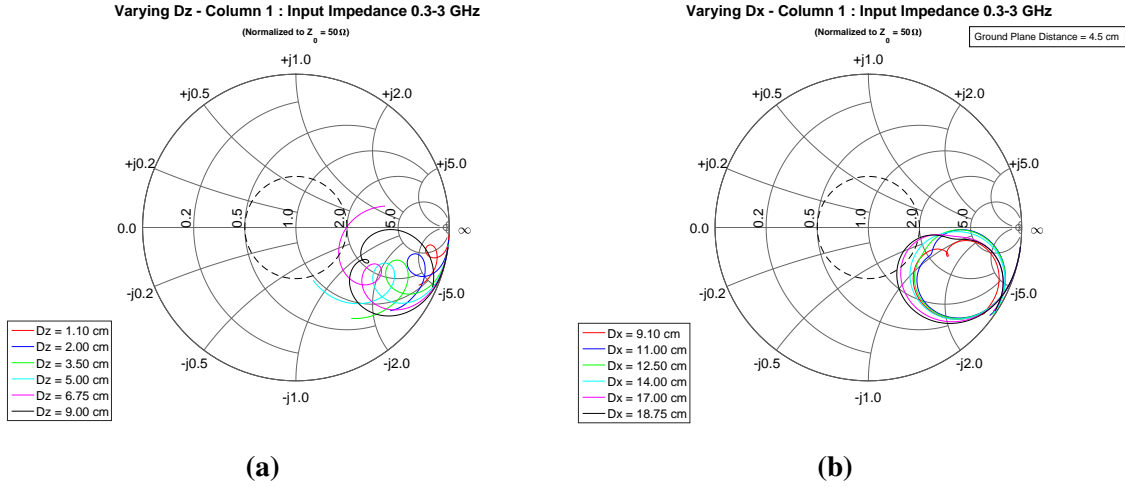


Figure 4.5: (a) Terminal impedances for Configuration 6 (b) Terminal impedances for Configuration 7

As seen in Figure 4.5a, the array spacing drastically affects the impedance of the horizontal dipoles. Intuitively, this makes sense as there is much more surface area presented between the dipoles within a single infinite column of horizontal elements. As the inter-element spacing D_z is reduced, the side-by-side configuration produces much stronger mutual coupling between the array elements versus the tip-to-tip vertical elements.

Unfortunately, the addition of the ground-plane does not enhance this effect but instead broadens the impedance curves for the horizontal dipoles once the ground-plane is added. Nevertheless, the curve for $D_x = 9.10$ cm is comparable to the impedance curve for the vertical dipole spacing $D_z = 10.00$ cm. Therefore, similar impedance values result for the vertical dipoles as the horizontal dipoles in the collinear array. More importantly, the $D_z = 10.00$ cm and $D_x = 9.10$ cm dimensions that were selected to produce the optimal

impedance curves for the vertical dipoles also produce the optimal impedance curves for the horizontal dipoles. Since the horizontal and vertical arrays ultimately must share the same array dimensions as one unified crossed-dipole array, this was a fortunate result.

Finally, Figure 4.6 shows the result of varying the ground-plane distance as indicated by Configuration 8 from Table 4.1:

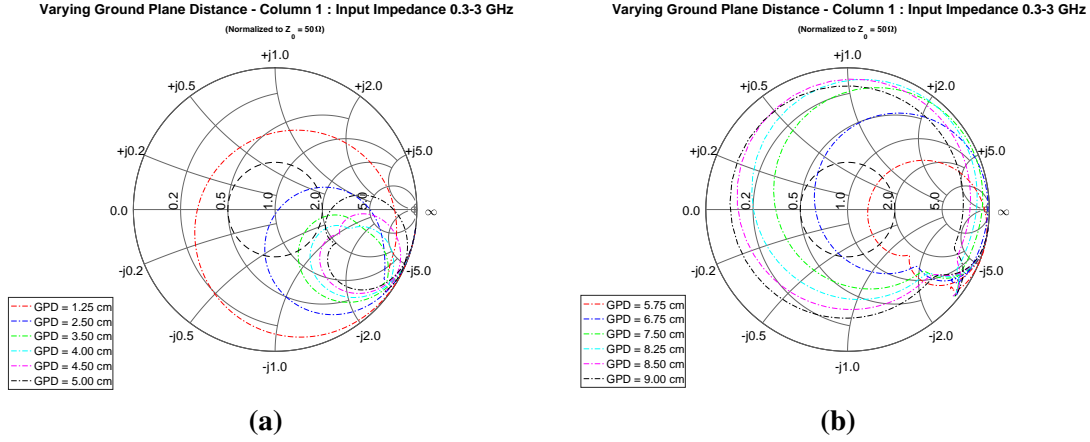


Figure 4.6: (a) Terminal impedances for Configuration 8 (b) Terminal impedances for Configuration 8

Again, the best results were obtained by letting the ground-plane distance be close to a quarter-wavelength away from the array at the center frequency of 1.5 GHz.

4.2 Stepped-Transmission Line Wide-band Matching

With the final spacing parameters determined as $D_z = 10.00$ cm, $D_x = 9.10$ cm, and with the ground-plane placed 5.00 cm behind the array, the stepped-transmission line wide-band matching technique as described in Section 3.3 was applied at the terminals. The results of applying the matching network are shown in the figures below by plotting the final transformed terminal impedances and the resultant VSWR of the antenna.

4.2.1 Impedance Matching Results: Two-Column Collinear Array.

The results for a two-stage matching network applied to the terminals of the vertical dipole array is shown in Figure 4.7:

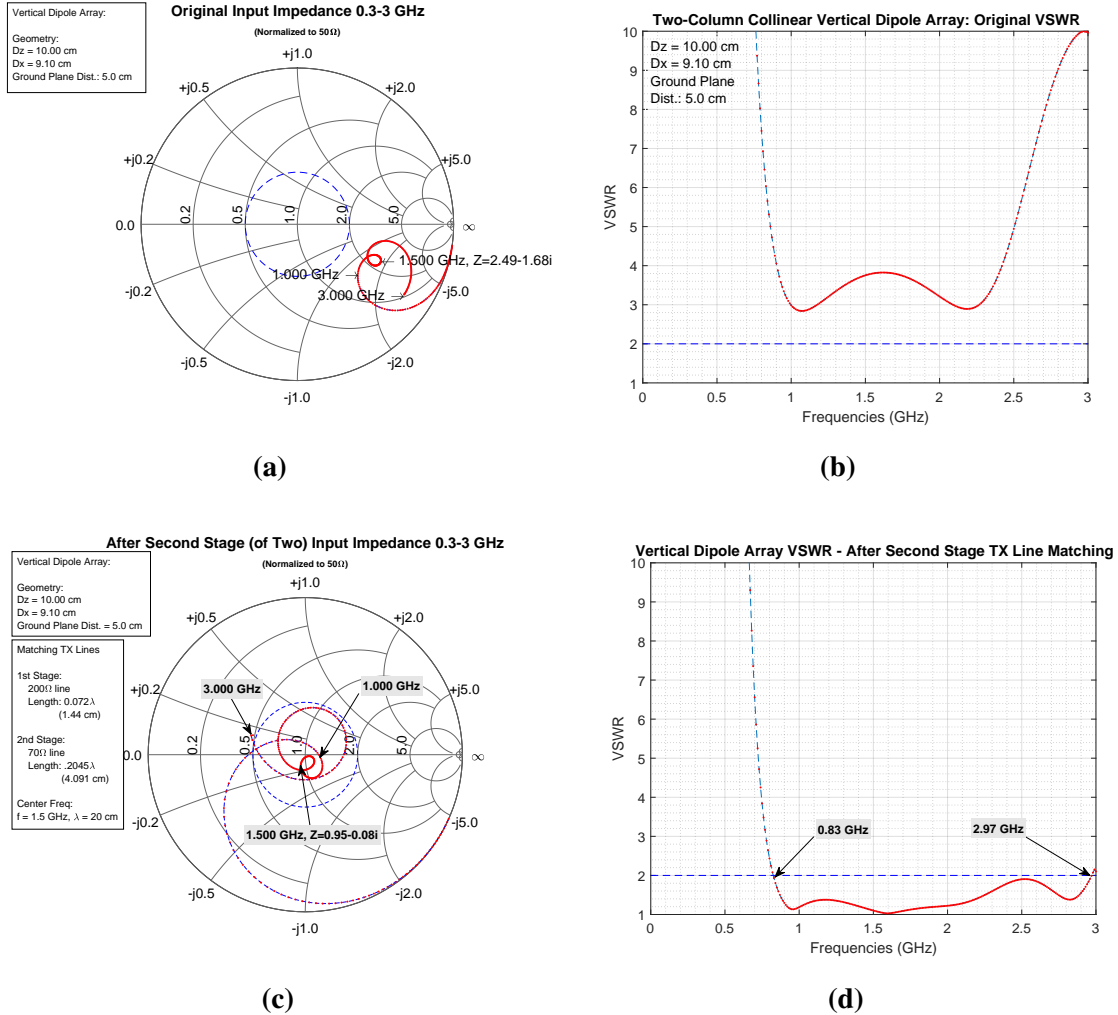


Figure 4.7: (a) Driving point impedances for optimal two-column collinear vertical dipole array. (b) VSWR for optimal two-column collinear vertical dipole array before matching. (c) Driving point impedances for two-column collinear vertical dipole array after wide-band matching. (d) VSWR for two-column collinear vertical dipole array after wide-band matching.

After following the procedures outlined in Section 3.3.2, the transmission line length GUI tool was used to fine tune the matching section lengths in order to bring more of the impedance curve from 0.3 GHz to 3.0 GHz below a VSWR of 2. It was found that using a section of transmission line slightly less than a quarter-wavelength long for the second matching section brought more of the frequency range below a VSWR of 2. A matching section of $L_1 = 1.44$ cm with a characteristic impedance of $Z_{01} = 200\Omega$ for the first segment was used. For the second matching section, $L_2 = 4.09$ cm with the characteristic impedance of the section $Z_{02} = 70\Omega$. Using this matching network, an impedance bandwidth of 0.83 GHz to 2.97 GHz (Fractional Bandwidth (FBW) = 3.6:1) was achieved for the vertical dipole array using the stepped-transmission line technique.

After comparing the single-stage versus two-stage matching solutions for the horizontal dipole array, it was seen that the single-stage stepped transmission line solution produced a wider impedance bandwidth. The results for a single-stage matching network for the horizontal dipole array is shown in Figure 4.8. For this matching network a transmission line section of $L_1 = 3.32$ cm with characteristic impedance $Z_{01} = 100\Omega$ was used. The result is an impedance bandwidth of 0.94 GHz to 2.47 GHz (FBW = 2.6:1).

Although this range still includes all of the L-band, which was objective of this study, the bandwidth is not quite as wide as the bandwidth for the vertical dipoles. When comparing Figure 4.7a against Figure 4.8a, it can be seen that the original impedance curve for the vertical dipoles was tighter to begin with versus the curve for the horizontal dipoles. Therefore, there was less spreading of the impedances as the curves were rotated around the Smith Chart. This made it easier to bring more of the frequency range for the vertical dipoles into the VSWR of 2 circle.

Since the vertical and horizontal dipoles must operate together 90° out-of-phase to achieve circular polarization in the crossed-dipole array, the bandwidth of the entire array is limited to the smaller of the two ranges (0.94 GHz to 2.47 GHz).

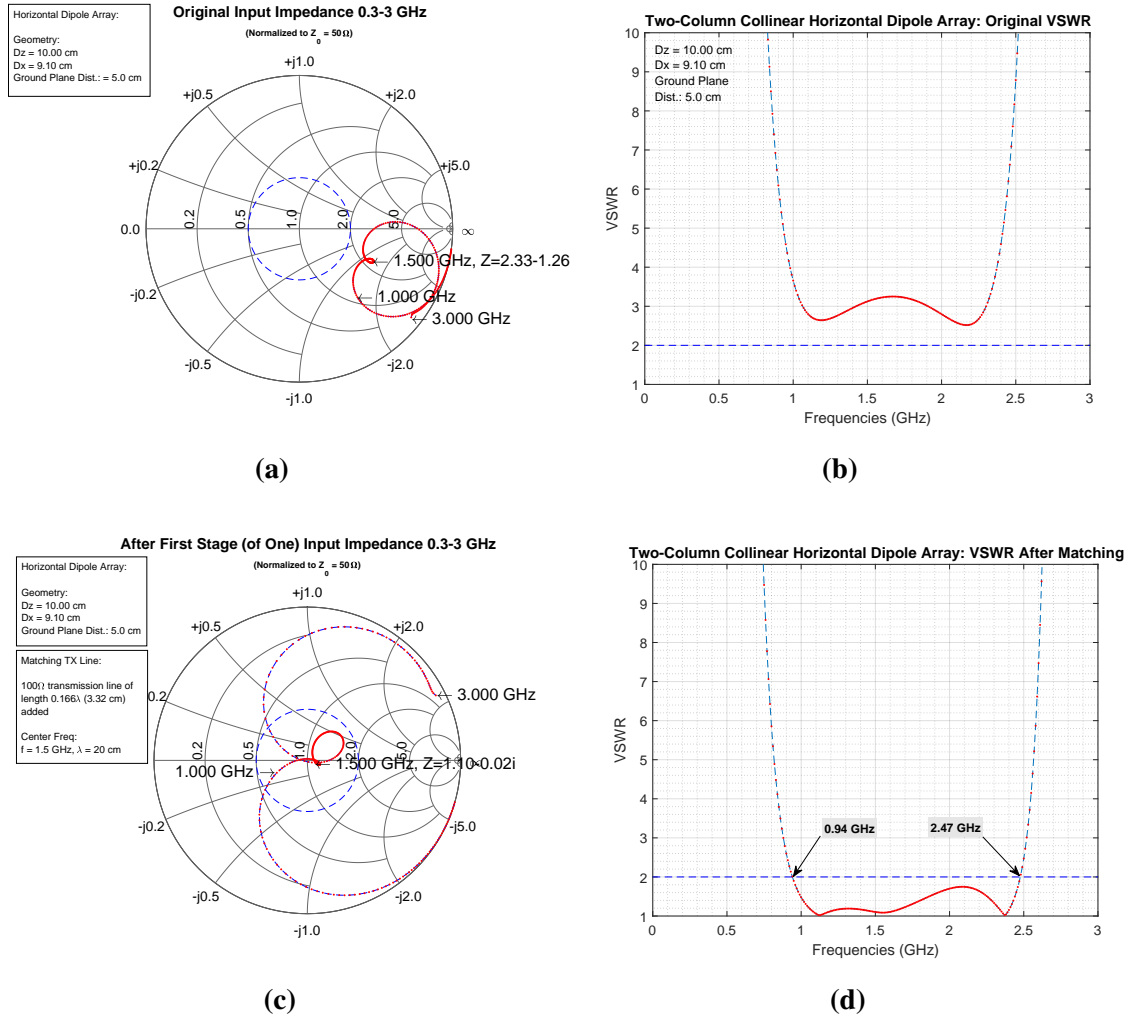


Figure 4.8: (a) Driving point impedances for optimal two-column collinear horizontal dipole array. (b) VSWR for optimal two-column collinear horizontal dipole array before matching. (c) Driving point impedances for two-column collinear horizontal dipole array after single-stage wide-band matching. (d) VSWR for two-column collinear horizontal dipole array after wide-band single-stage matching.

4.2.2 Impedance Matching Results: Two-Column Staggered Array.

To see if the denser, staggered dipole arrangement depicted in Figure 3.4b could perform any better based on its closer array element spacing, a SPLAT simulation was run for one possible configuration for a two-column staggered array.

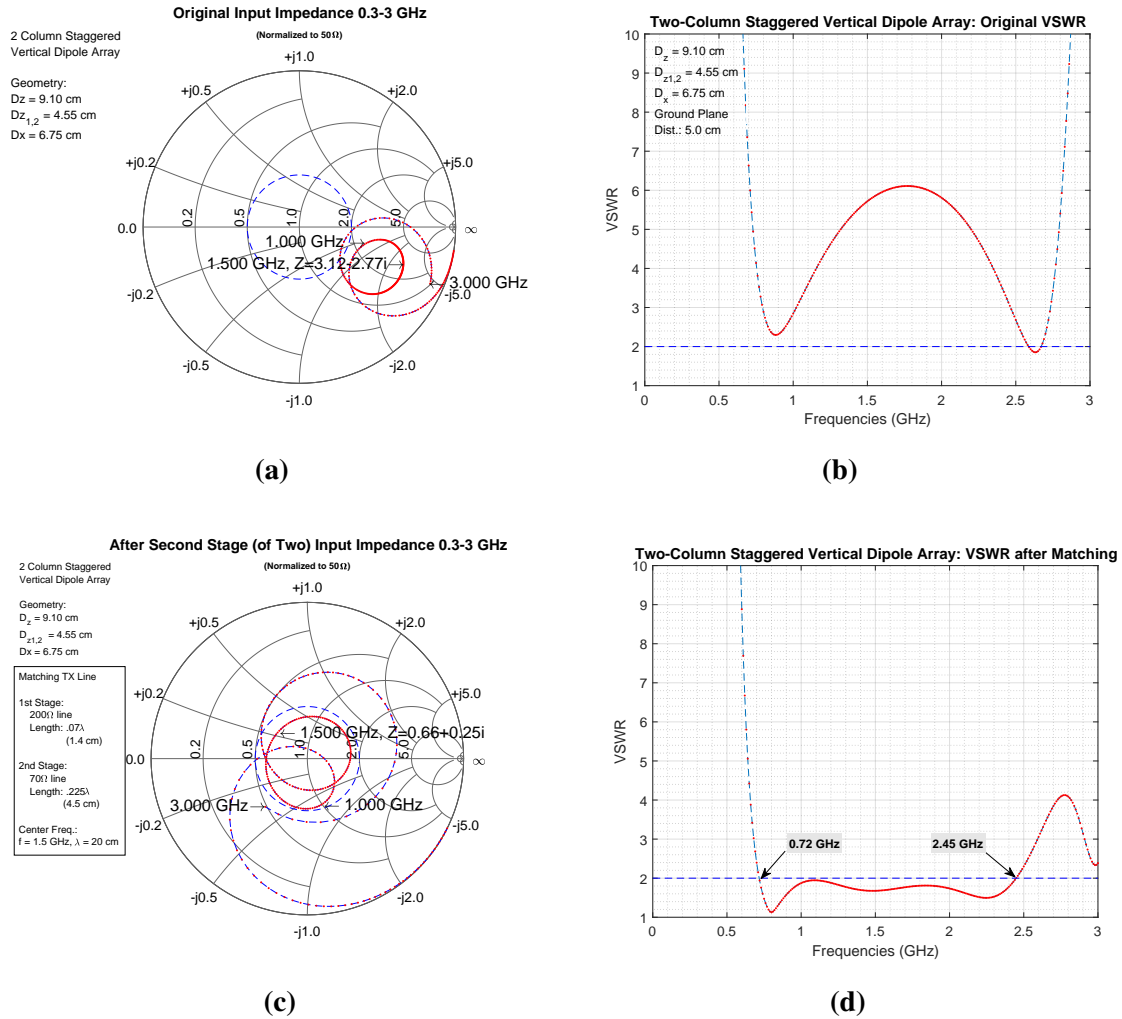
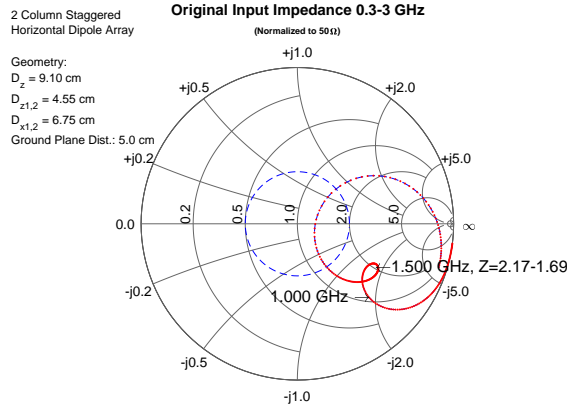


Figure 4.9: (a) Driving point impedances for two-column staggered vertical dipole array (b) VSWR for two-column staggered vertical dipole array before matching (c) Driving point impedances for two-column staggered vertical dipole array after two-stage wide-band matching (d) VSWR for two-column staggered vertical dipole array after two-stage wide-band matching

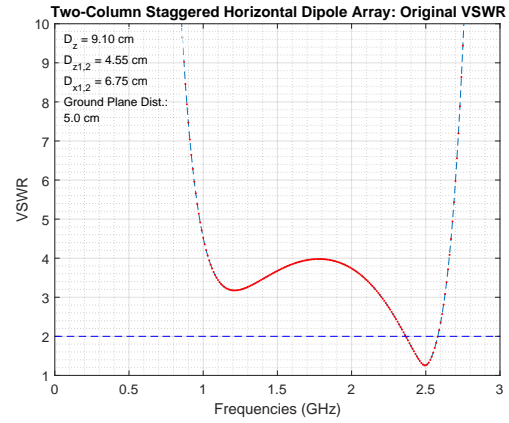
The results for a two-stage matching network for the staggered vertical dipole array is shown in Figure 4.9. The same $D_z = 9.10$ cm spacing was used for elements within each column, but the $D_{z1,2}$ offset of 4.55 cm between the two columns allowed the D_x spacing to be made closer at 6.75 cm without the horizontal dipoles touching. The resulting impedance curve for this arrangement is shown in Figure 4.9a. Although the curve is fairly tight, the high-frequency tail starts to widen after around 2 GHz. A two-stage stepped-transmission line matching network was used to perform the impedance matching. The result of using a first section of 1.4 cm, 200Ω line and a 4.5 cm, 70Ω line second section produced an impedance bandwidth of 0.72 GHz to 2.45 GHz (FBW = 3.4:1).

The results for a two-stage matching network for the horizontal dipole array is shown in Figure 4.10. As shown in Figure 4.10a, the original impedance curve for the staggered horizontal arrays is broader than the curve for the collinear horizontal array. A two-stage matching network comprised of a 0.6 cm, 200Ω line first stage and a 4.0 cm, 70Ω line second stage produced an impedance bandwidth of 1.00 GHz to 2.55 GHz (FBW: 2.55:1).

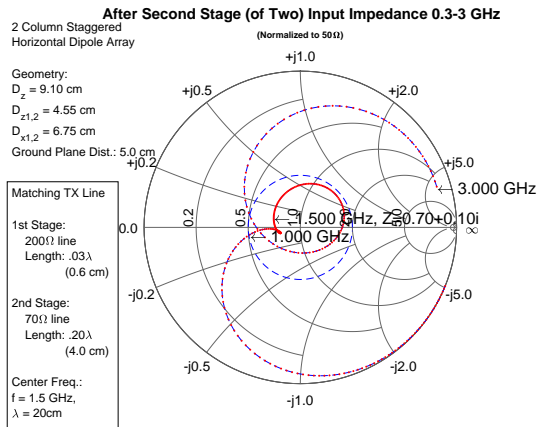
Therefore, when comparing the collinear array to the staggered array, the resulting impedance bandwidths are similar. Of course, only one staggered configuration was tested. A similar parametric study as the one conducted for the collinear array could be conducted to find a better starting configuration for the staggered array before wideband matching.



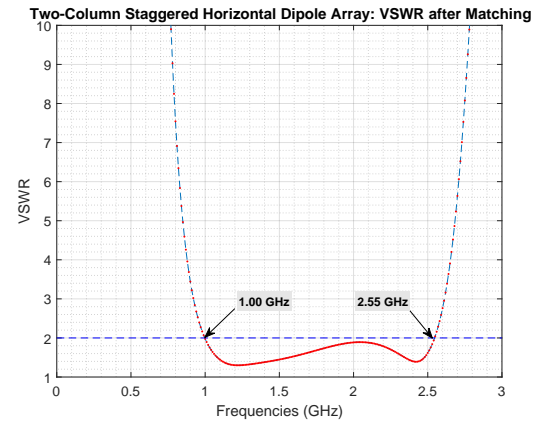
(a)



(b)



(c)



(d)

Figure 4.10: (a) Driving point impedances for two-column staggered horizontal dipole array. (b) VSWR for two-column staggered horizontal dipole array before matching. (c) Driving point impedances for two-column staggered horizontal dipole array after two-stage wide-band matching. (d) VSWR for two-column staggered horizontal dipole array after two-stage wide-band matching.

The results of the impedance matching for the collinear and staggered dipole arrays are summarized in Table 4.2:

Table 4.2: Impedance matching results

Array Type	Dipole Orientation	Matching Network Type	Z_{01}, L_1	Z_{02}, L_2	Impedance Bandwidth	Frac. BW
Collinear	Vertical	Two-Stage	200 Ω , 1.44 cm	70 Ω , 4.09 cm	0.83 GHz - 2.97 GHz	3.6:1
Collinear	Horizontal	Single-Stage	–	100 Ω , 3.32 cm	0.94 GHz - 2.47 GHz	2.6:1
Staggered	Vertical	Two-Stage	200 Ω , 1.40 cm	70 Ω , 4.50 cm	0.72 GHz - 2.45 GHz	3.4:1
Staggered	Horizontal	Two-Stage	200 Ω , 0.60 cm	70 Ω , 4.00 cm	1.00 GHz - 2.55 GHz	2.6:1

The impedance bandwidth for the staggered dipole array would again be limited to the inner most bounds of the impedance bandwidths calculated for each element orientation. Therefore, the staggered array's total circular polarization bandwidth would be from 1.00 GHz to 2.45 GHz. This range still covers the L-band, and the frequencies spanned in this range are close to the frequencies covered by the collinear array.

4.3 Current Distributions on the Array Dipoles

The impedances calculated for the crossed-dipole arrays are related to the values of the terminal currents by Ohm's Law. Since the terminal voltages are always set to a constant normalized value of 1V, the small variations in the terminal impedances shown by the tight impedance curves on the Smith Chart indicate that the terminal currents are also varying minimally with frequency. However, the impedance is only calculated at the terminals of the dipoles using the coefficients of the current basis functions as described in Section 3.2.5.1. Therefore, the Smith Charts do not provide any information about the current distribution over the entire reference dipole.

By the principle of pattern multiplication, the far-field pattern of the array is calculated in part by the pattern factor of Equation 3.12. This term takes into account the distribution of the currents on the reference dipole of each infinite column array. Therefore, although the impedance bandwidths calculated in Section 4.2.2 describe the range of frequencies

where minimal power is lost due to impedance mismatch, this bandwidth figure does not guarantee that the array will produce a desirable radiation pattern at those frequencies. To adopt the terminology used in [20], which describes the duality of an antenna as both a circuit device and a space device, the impedance bandwidth analysis thus far has considered the array from a circuit device perspective. Circuit parameters such as the mismatch loss, reflection coefficient, and VSWR have been considered in the impedance bandwidth study.

However, the space parameters such as the far-field pattern and directivity must also be considered, especially because the array is designed as a feed for such a unique, sparse-aperture, cruciform reflector. The transition region between the circuit quantities and the space quantities is the current distribution on the array [20]. Therefore, the current distributions on the reference dipoles were reconstructed using the sinusoidal basis functions and the weighting coefficients as described in Section 3.2.5.1. The figures in this section show what the current distribution looks like on the array for both the L-band set of frequencies, and at the limits of the impedance bandwidth calculated in the previous section. The far-field patterns calculated from these current distributions are then shown in Section 4.4.

4.3.1 Current Distribution on Two-Column Collinear Array.

The current distribution on the reference dipoles in the two-column collinear array at the center frequency of the L-band at 1.5 GHz is shown in Figure 4.11. As indicated by the data point labels on the plot, the complex weighting coefficients have now been applied to the unweighted normalized sinusoidal basis functions. The linear combination of these basis functions reconstructs the current. The distance coordinates given in the plots are the local coordinates of each reference dipole and not the global coordinates that are relative to the center of the array. For the horizontal dipoles, the current distribution was not identical for both columns, but was instead symmetric about the center of the array. The current

distribution for both columns of the vertical arrays were identical, so only the distribution on Column 1 is shown.

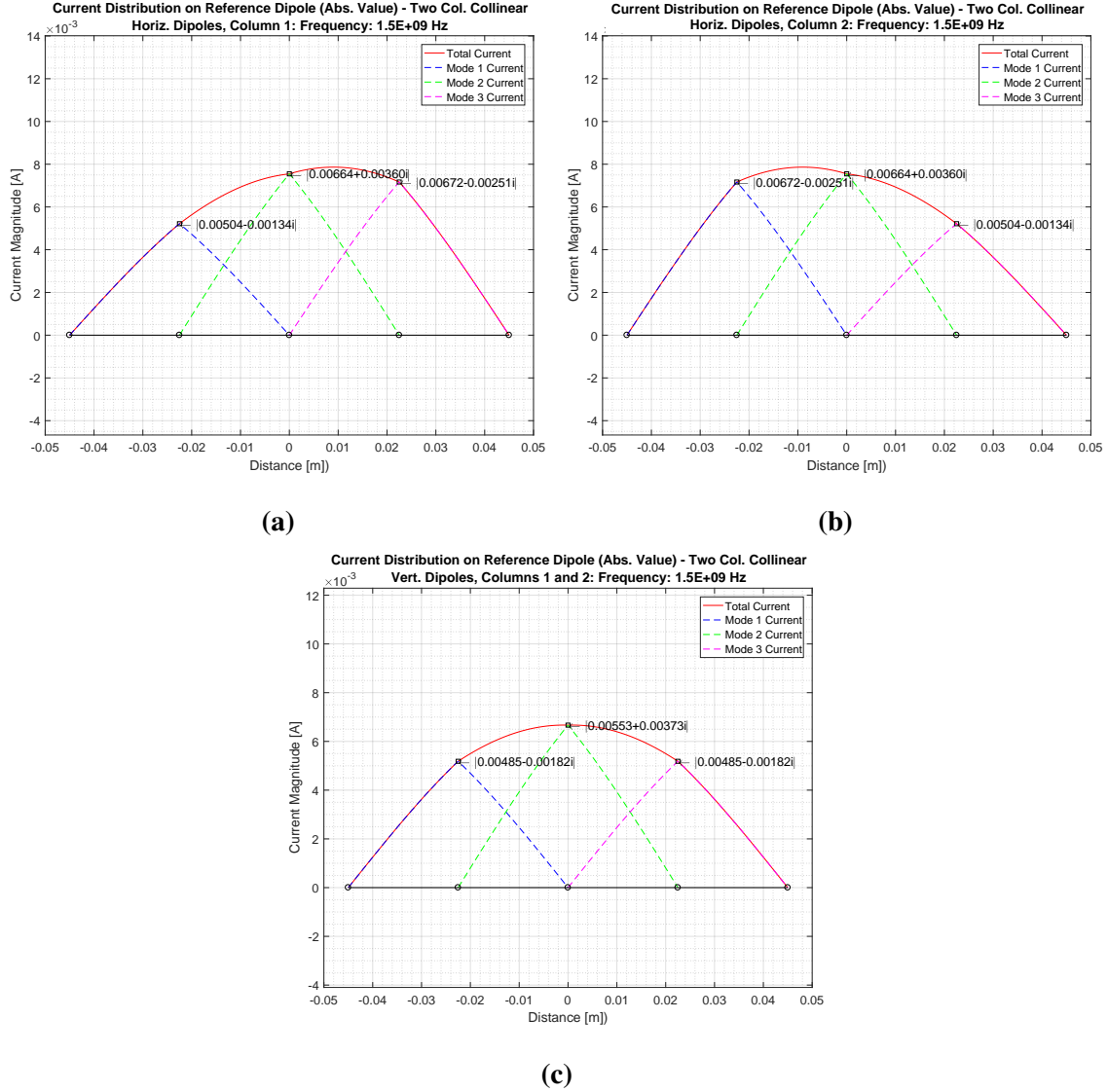


Figure 4.11: (a) Current distribution along reference dipole of Column 1 for horizontal collinear array at 1.5 GHz. (b) Current distribution along reference dipole of Column 2 for horizontal collinear array at 1.5 GHz. (c) Current distribution along reference dipole of Columns 1 and 2 for vertical collinear array at 1.5 GHz.

At the resonant frequency of the individual dipoles, the current maximum occurs at the center of the dipoles for the vertical infinite array. For the two horizontal columns, the voltages at the terminals of the neighboring horizontal element pulls the current maximum towards this neighboring element. The plots in Figure 4.11 only show the magnitude of the current distribution. The phase information for the current along the dipole can be seen by plotting the real and imaginary components separately.

The magnitude of the current distribution on the reference dipoles of the two-column collinear array for five evenly spaced frequencies in the L-band (1.0 GHz, 1.25 GHz, 1.50 GHz, 1.75 GHz and 2.00 GHz) are shown in Figure 4.12. The location of the current maximum for the horizontal dipoles moves increasingly towards the other horizontal element as the frequency increases. Additionally, by 2 GHz, a second peak in the current distribution starts to appear for both dipole orientations. The presence of these second current maxima on the dipoles is responsible for the side-lobes in the far-field pattern as shown in Figure 4.15a and Figure 4.18a.

The magnitude of the current of the dipoles at the terminals is also indicated in Figure 4.12. As was discussed, these were the current values that were used in calculating the terminal impedances. The minimum and maximum values of the terminal currents are shown. The variation in the value of the complex terminal currents is responsible for the shape of the terminal impedance curves plotted on the Smith Charts. The superimposed current distributions show for which frequencies this variation is minimal. Furthermore, the overall similarity of the entire current distribution from frequency to frequency translates into a uniformity in the far-field patterns at these different frequencies as shown in the plots in Section 4.4.

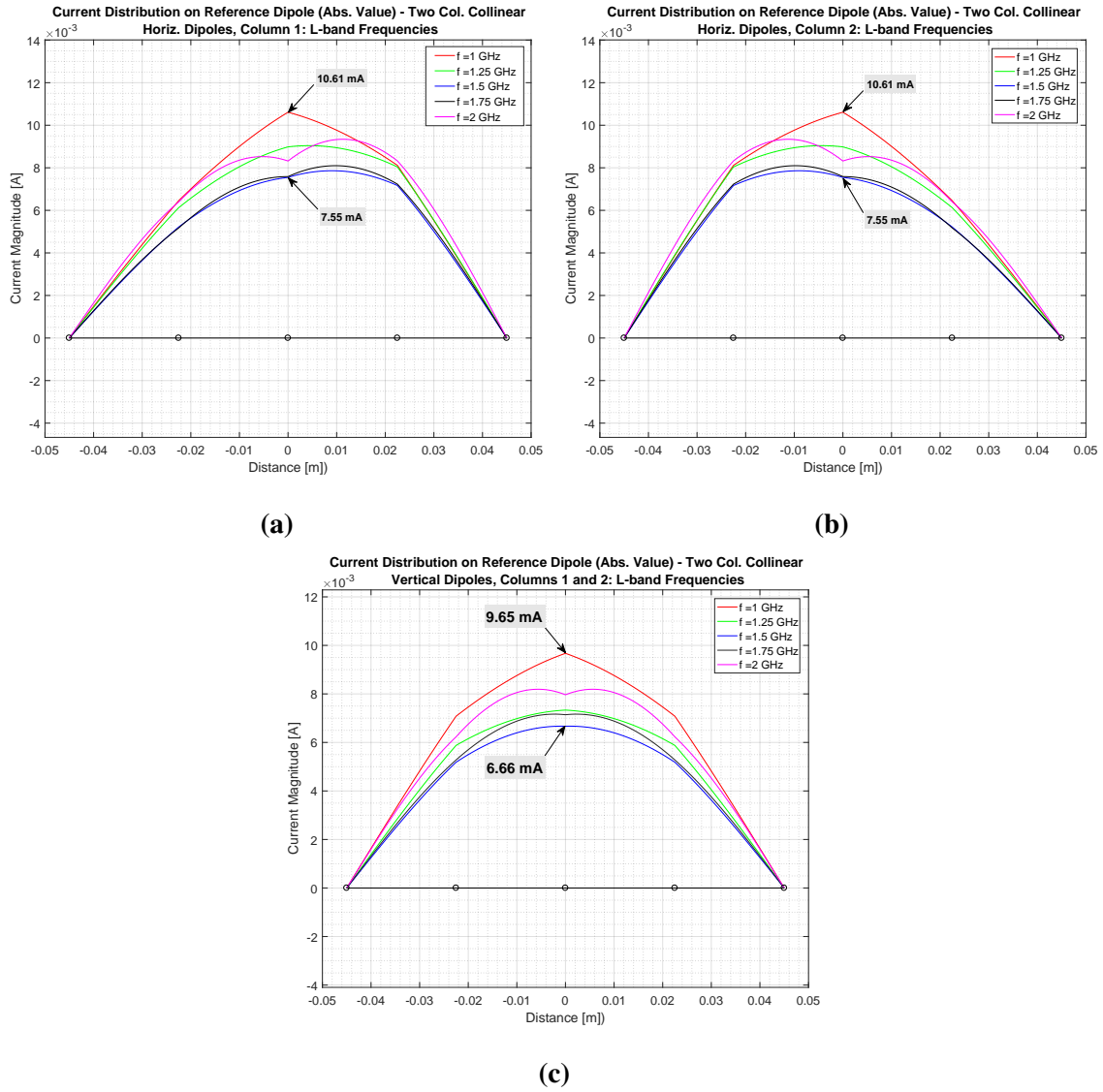


Figure 4.12: (a) Current distribution along reference dipole of Column 1 for horizontal collinear array from 1-2 GHz. (b) Current distribution along reference dipole of Column 2 for horizontal collinear array from 1-2 GHz. (c) Current distribution along reference dipole of Columns 1 and 2 for vertical collinear array from 1-2 GHz.

The same procedure was repeated to find the current distribution for the limits of the impedance bandwidth for the horizontal and vertical collinear arrays listed in Table 4.2:

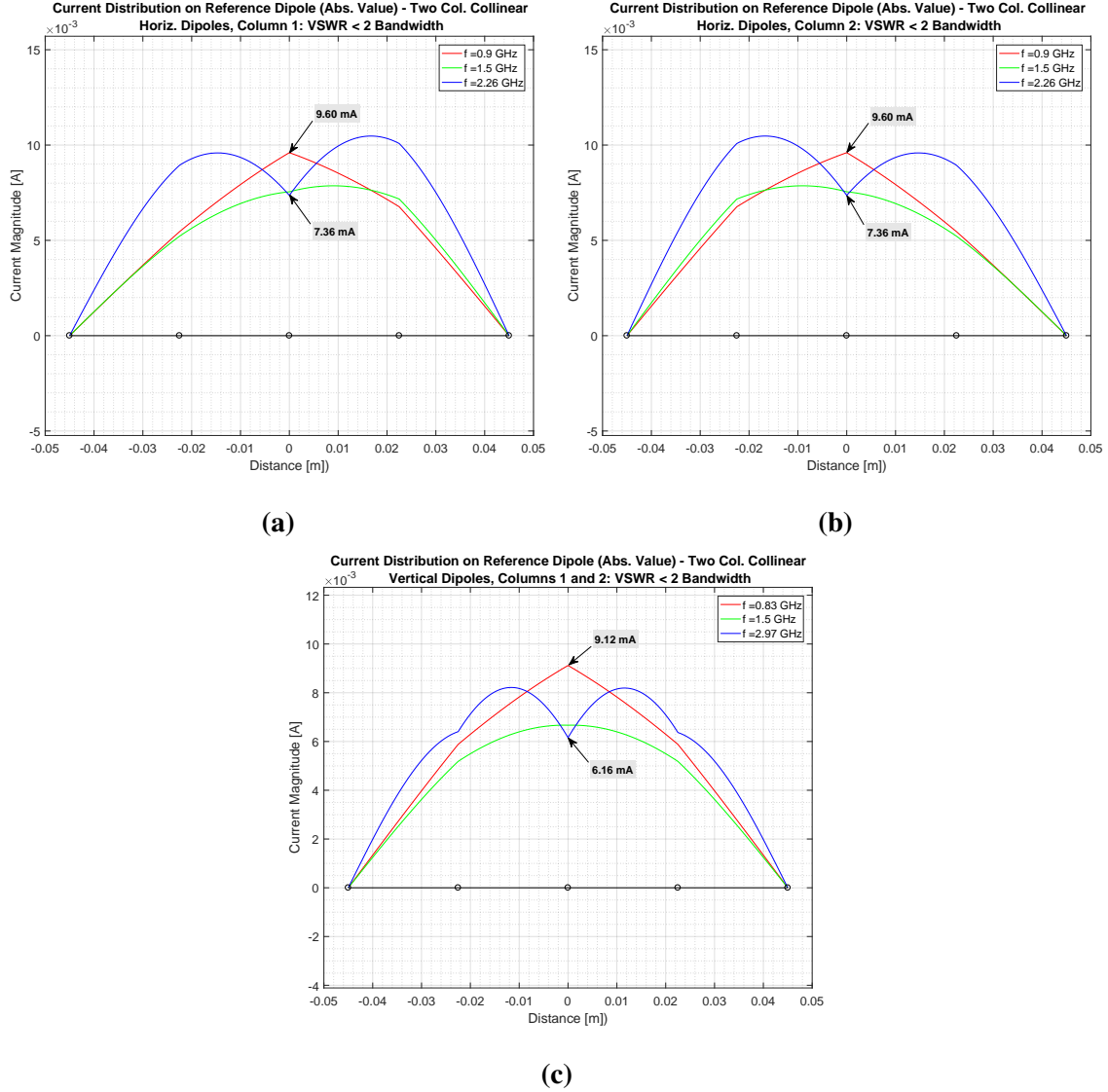


Figure 4.13: (a) Current distribution along reference dipole of column 1 for horizontal collinear array (b) Current distribution along reference dipole of column 2 for horizontal collinear array (c) Current distribution along reference dipole of columns 1 and 2 for vertical collinear array

As shown in Figure 4.13, by 2.97 GHz for the vertical dipoles, the second current maximum causes the main beam in Figure 4.15c to point off-axis with considerable side-lobes also present in the pattern.

4.3.2 Current Distribution on Two-Column Staggered Array.

Figure 4.14 plots the L-band current distributions for the two-column staggered array configuration specified in Table 3.2. The distributions are more uniform from frequency to frequency for the staggered arrays. The current distribution on the horizontal dipoles in the staggered column array are also identical between Columns 1 and 2. Furthermore, no additional current maxima are present at 2.0 GHz. Therefore, especially for the vertical dipoles, the denser staggered array helps keep the entire current distribution more uniform across the frequency range than the collinear array.

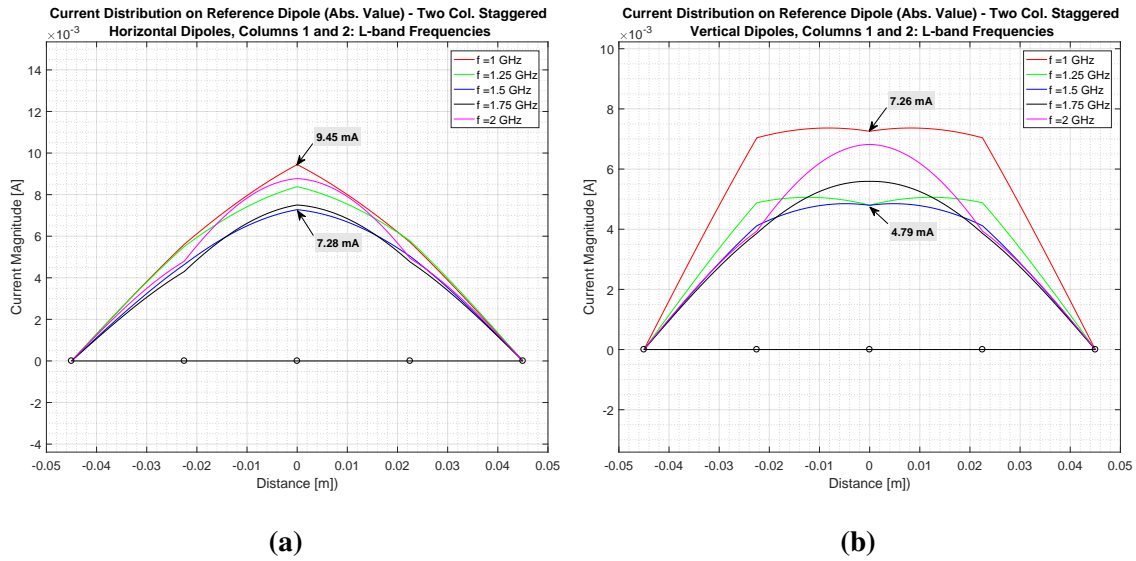


Figure 4.14: (a) Current distribution along reference dipole for vertical staggered array (b) Current distribution along reference dipole for horizontal staggered array

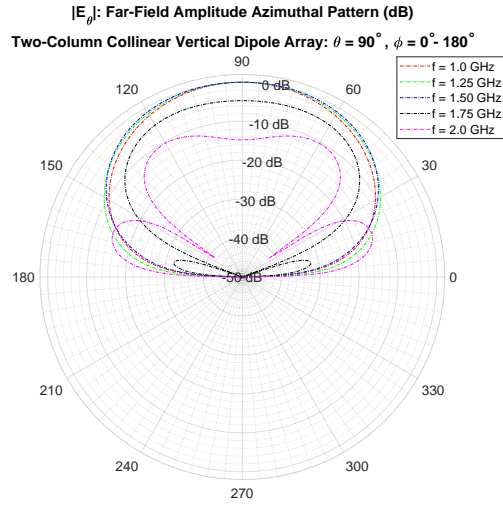
This consistency of the current distribution across the L-band frequency range results in the uniform far-field amplitude patterns for the staggered array as shown in Figure 4.20 and Figure 4.22.

4.4 Tightly Packed Dipole Array Far-field Patterns

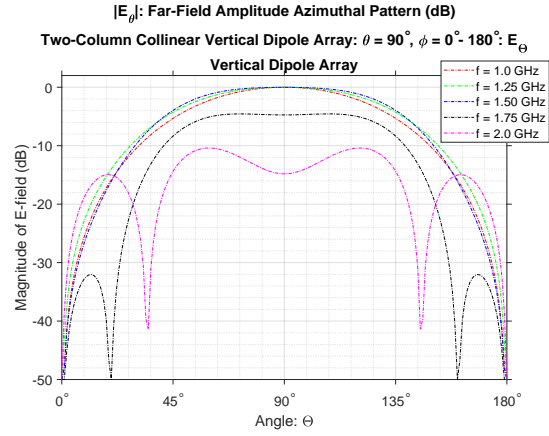
4.4.1 Far-Field Amplitude Plot: Two-Column Collinear Array.

The far-field amplitude patterns for the two-column collinear array with dimensions $D_z = 9.10$ cm, $D_x = 10.00$ cm, and ground-plane distance = 5.0 cm are shown in this section. The far-field patterns are calculated for the same frequencies for which the current distributions in Section 4.3 were plotted. As discussed in Section 3.4, the far-field plots computed directly from SPLAT in bistatic mode are limited to the azimuthal pattern with the elevation angle θ fixed at 90° based on the definition of the excitation voltages. The amplitude patterns for the $|\mathbf{E}_\theta|$ component and $|\mathbf{E}_\phi|$ component of the E-field are plotted separately. The elevation pattern with the azimuthal angle ϕ fixed at 90° was computed using the array factor pattern multiplication method in MATLAB and the current distributions calculated in SPLAT as described in Section 3.4.

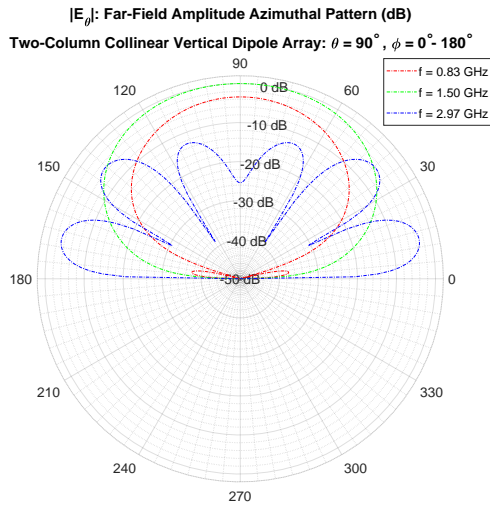
The $|\mathbf{E}_\phi|$ patterns were computed by using the horizontal dipole array current distributions shown in the previous section for the input variable I in Equation 3.12. Similarly, the $|\mathbf{E}_\theta|$ patterns are produced by the currents on the vertical dipole elements in the crossed-dipole array. Together, these two plots for each field component represent the radiation pattern from a circularly polarized array. By the reciprocity theorem, these amplitude patterns are equivalent to the receive pattern for the antenna feed [7]. Each polar plot of the pattern is accompanied by the equivalent representation in rectangular coordinates. All patterns are normalized to the peak value of the main beam.



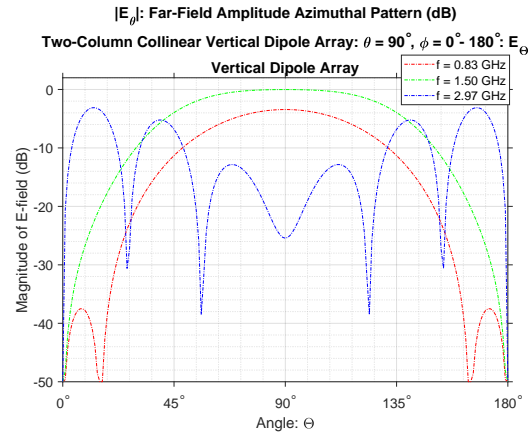
(a)



(b)



(c)



(d)

Figure 4.15: (a) Far-field plot of $|E_\theta|$ azimuthal amplitude pattern for two-column collinear crossed-dipole array (1-2 GHz). (b) Rectangular plot of $|E_\theta|$ far-field (1-2 GHz). (c) Far-field plot of $|E_\theta|$ azimuthal amplitude pattern for two-column collinear crossed-dipole array (0.83-2.97 GHz). (d) Rectangular plot of $|E_\theta|$ far-field (0.83-2.97 GHz).

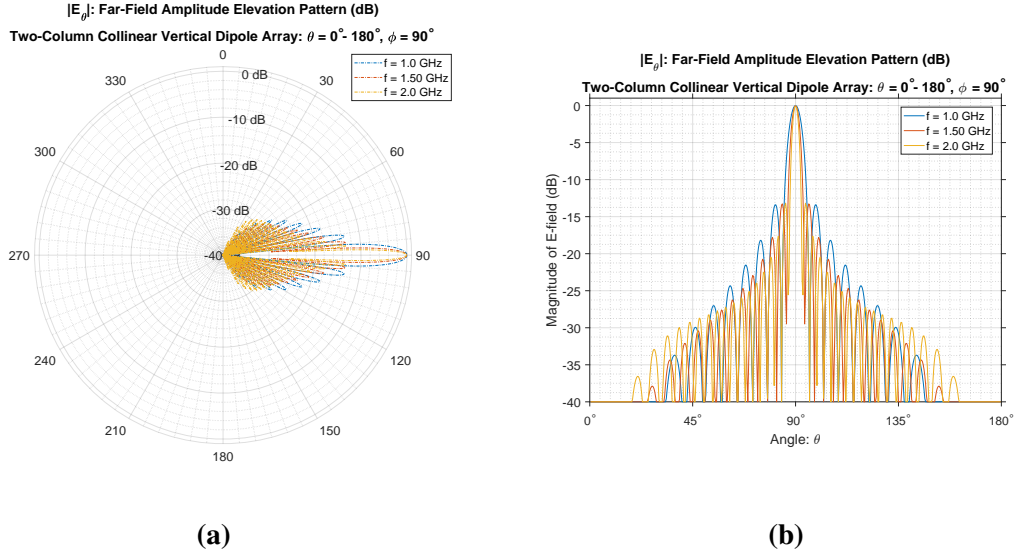


Figure 4.16: (a) $|E_\theta|$ Far-field amplitude elevation pattern for collinear crossed-dipole array (b) $|E_\theta|$ far-field amplitude elevation pattern for collinear crossed-dipole array rectangular plot array

The amplitude patterns for the vertical component of the crossed-dipole array in Figure 4.15 show the effect that the changing current distribution has on the shape of the radiation pattern and the size of the side-lobes. For the pattern at 2.0 GHz, the main beams point off-axis from the surface normal of the array towards the $\phi = 50^\circ$ and $\phi = 130^\circ$ directions. The amplitude of the E_θ component of the field in the normal direction of $\phi = 90^\circ$ is 4 dB lower than the value of the field for these two main beams at 2.0 GHz. However, aside from the pattern at 2.0 GHz, the patterns for E_θ for the other frequencies are otherwise fairly consistent in terms of shape and magnitude in the direction towards the reflector.

The pattern at 2.97 GHz, which is the upper limit of the impedance bandwidth calculated for the vertical dipole array, however, shows the effect of the multiple current maxima in the current distribution shown in Figure 4.15c. In the far-field, the main beam

is again steered off axis from the surface normal of the array and multiple side-lobes occur. The amplitude of the field in the direction towards the reflector at $\phi = 90^\circ$ at 2.97 GHz is 24 dB below the value of the field in this direction at 1.5 GHz. This shows that the performance of the antenna in terms of the space parameters at the limits of the calculated impedance bandwidth may not be adequate. Based the gain requirement for the far-field pattern, the pattern bandwidth may be more restrictive than the impedance bandwidth calculated for the feed. Nevertheless, Figure 4.15 shows that within the L-band at least, the E_θ amplitude pattern is consistent in magnitude with the main beam pointing in the $\phi = 90^\circ$ direction towards the reflector.

Figure 4.16 shows that the 28-by-2 element array produces a narrow main-beam for the E_θ elevation pattern. This is ideal in efficiently illuminating the narrow horizontal arm of the reflector shown Figure 4.17 [4].

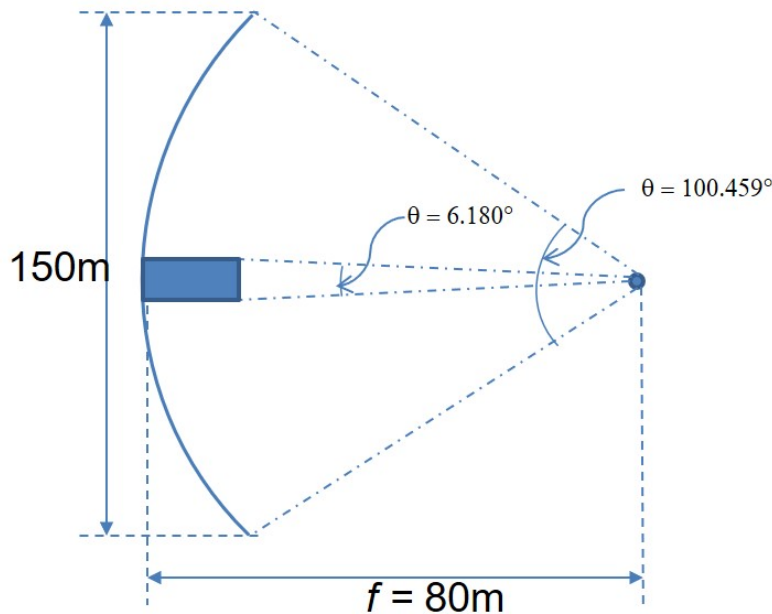


Figure 4.17: Cruciform reflector geometry side view showing the 6.18 degree fill-angle for the reflector arms

The magnitude of the closest side-lobes are about -12 dB below that of the main beam. Table 4.3 lists the 3 dB beamwidth and the magnitude of the elevation pattern at the 6.18° point illustrated in Figure 4.17. Ideally, at this angle we would want the magnitude of the field to fall off sharply to minimize the spillover. A -10 dB drop-off from the peak value of the main-beam was used originally as a design goal for the feed in [3]. As shown in Table 4.3, the collinear array meets this design criteria for the vertical elements and comes close to meeting it for the horizontal elements.

Table 4.3: Collinear and Staggered Array Beamwidth Calculations

<i>at 1.5 GHz</i>	Collinear Vert. Elem.	Collinear Horiz. Elem.	Staggered Vert. Elem.	Staggered Horiz. Elem.
3 dB Beamwidth	3.67°	4.01°	7.91°	5.04°
Magnitude at 6.18°	-12.23 dB	-9.36 dB	-2.08 dB	-5.08 dB
10 dB Beamwidth	5.73°	6.98°	12.94°	10.42°

Figure 4.18 shows the far-field amplitude pattern for the E_ϕ component of the field. The azimuthal pattern exhibits a similar uniform pattern which starts to degrade at 2.0 GHz. The elevation pattern however shows high directivity across the L-band range with again about a -12 dB difference between the magnitude of the main beam and the nearest side-lobe.

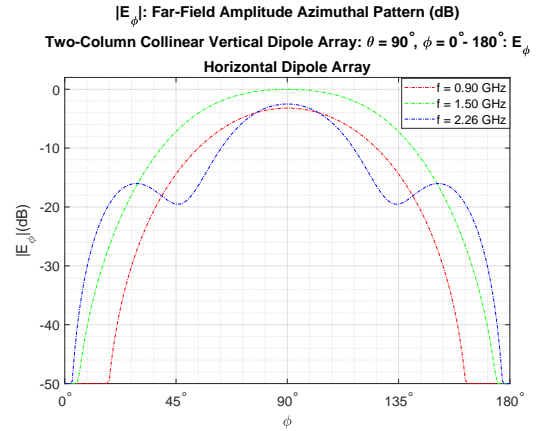
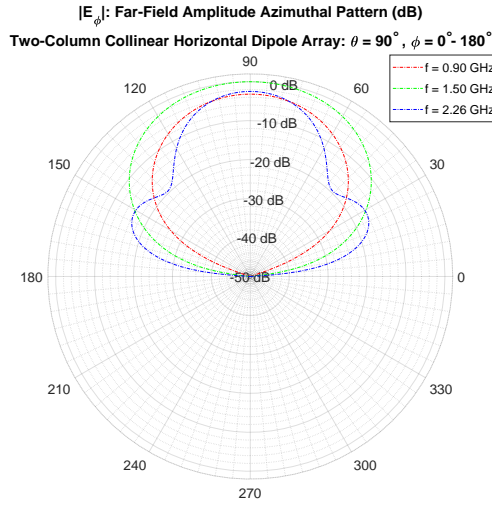
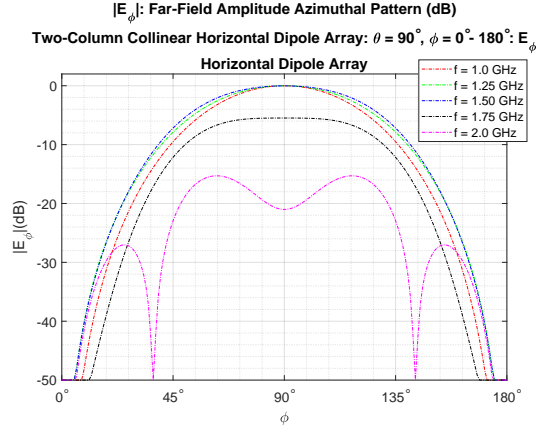
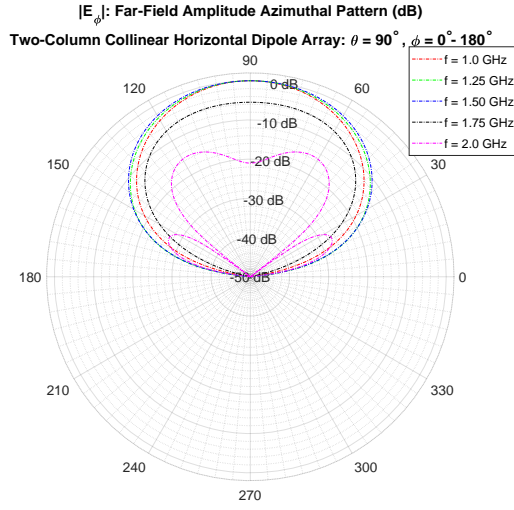


Figure 4.18: (a) Far-field plot of $|E_\phi|$ azimuthal amplitude pattern for two-column collinear crossed-dipole array (1-2 GHz). (b) Rectangular plot of $|E_\phi|$ far-field (1-2 GHz). (c) Far-field plot of $|E_\phi|$ azimuthal amplitude pattern for two-column collinear crossed-dipole array (0.90-2.26 GHz). (d) Rectangular plot of $|E_\phi|$ far-field (0.90-2.26 GHz).

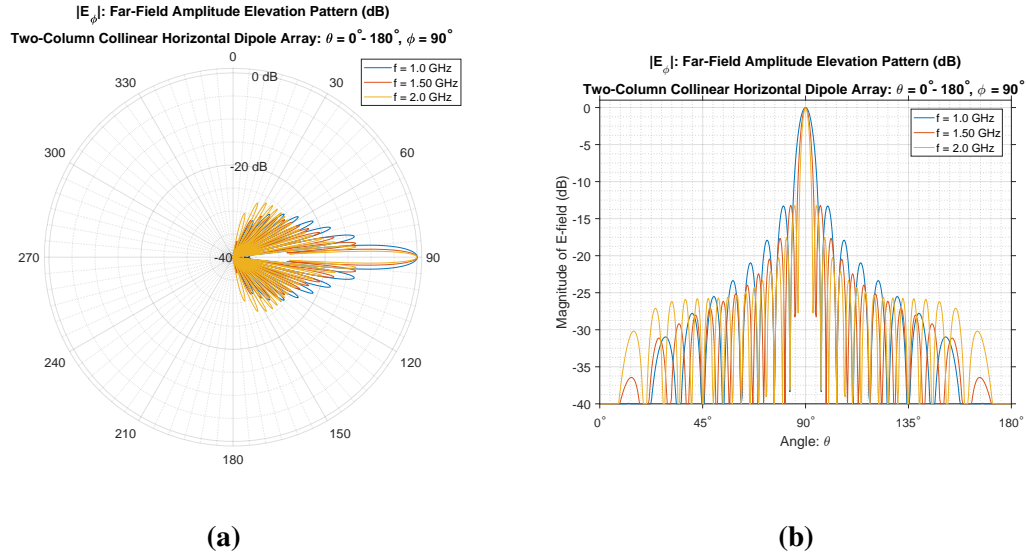


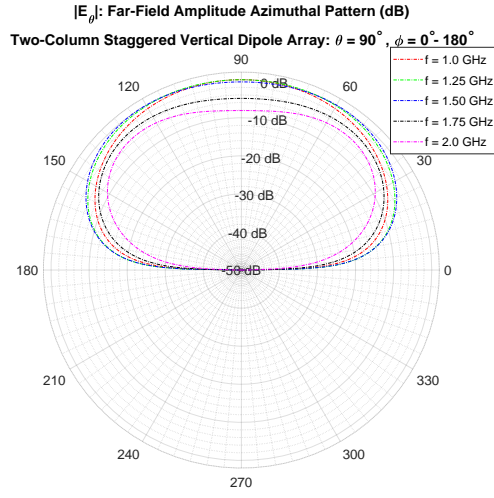
Figure 4.19: (a) $|E_\phi|$ far-field amplitude elevation pattern for collinear crossed-dipole array (b) $|E_\phi|$ far-field amplitude elevation pattern for collinear crossed-dipole array rectangular plot

4.4.2 Far-Field Amplitude Plot: Two-Column Staggered Array.

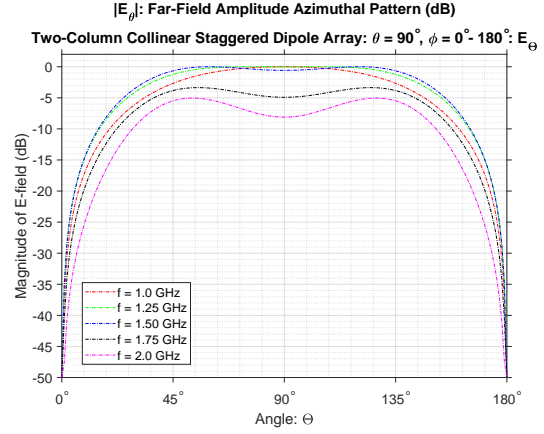
The far-field patterns were also calculated for the staggered-array configuration. As seen from Figure 4.14a and Figure 4.14b, the current distributions for the staggered array dipoles remained very consistent between the L-band frequencies. This translates into the uniform far-field patterns for the L-band frequencies shown in Figure 4.20 and Figure 4.22. The amplitude patterns for the staggered array also maintain this uniformity up to 2.00 GHz unlike the patterns for the collinear array. Thus, if the design requirements favor the consistency of the pattern over the width of the impedance bandwidth, then the staggered arrangement would be preferable. However, the trade-off in the elevation pattern is that the denser array configuration does not exhibit as narrow of a main-beam as seen in Figure 4.21 and in Table 4.3. With only a -2.08 dB and -5.08 dB drop-off at the 6.18° point, there would be significant spillover past the reflector arms from the staggered dipole array.

It should be noted that these far-field patterns for all of the configurations were obtained by assuming an identical current distribution on all elements relative to the reference dipoles in the array. In actuality, the currents on the elements in the finite 108-element feed in Figure 2.3 would exhibit some variation. The elements towards the end of the arrays would exhibit the same kind of perturbation seen in Figure 4.12a and Figure 4.12b, which demonstrate what happens to the current distribution on the edge elements for a finite array.

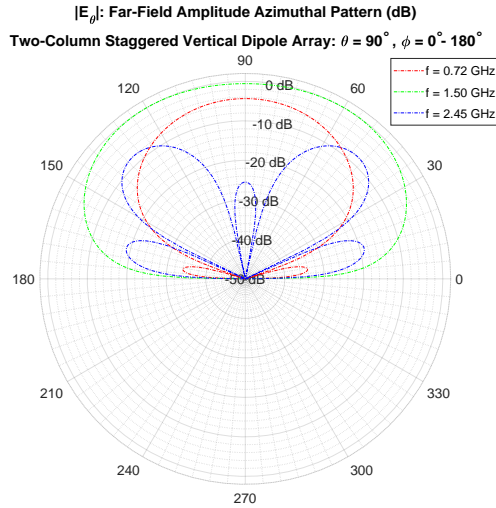
Furthermore, a separate study has been proposed for this feed design which involves tailoring the shape of the far-field pattern from the array using the technique of pattern synthesis [21]. Therefore, a study dedicated to optimizing the pattern for the cruciform reflector could be performed to produce far-field patterns that are more suitable than the results shown in this section. The main focus of this study was in the optimization of the array geometry to improve the impedance bandwidth of the crossed-dipole array. The far-field plots were calculated to provide some baseline information about what the pattern would look like based on these array geometries and resulting current distributions.



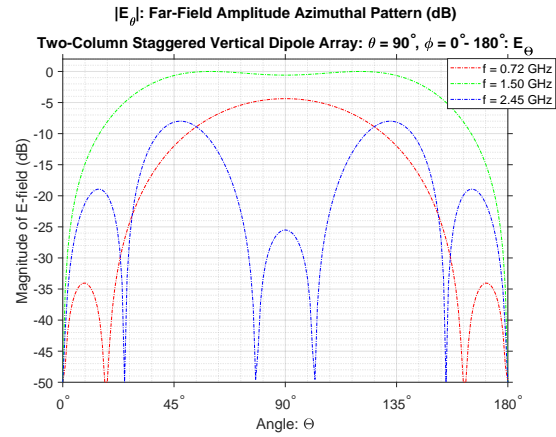
(a)



(b)

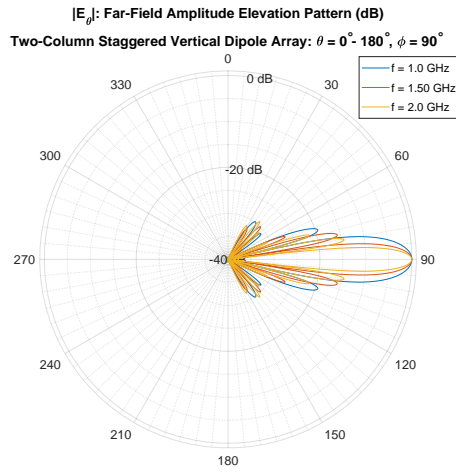


(c)

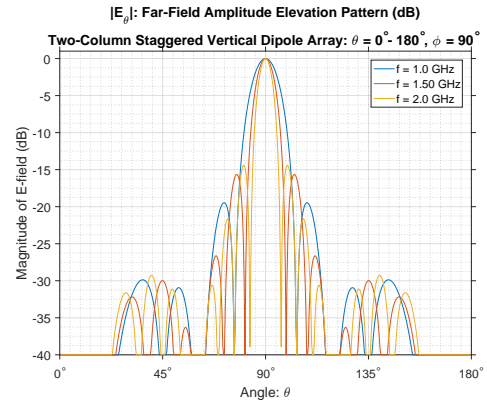


(d)

Figure 4.20: (a) Far-field plot of $|E_\theta|$ azimuthal amplitude pattern for two-column staggered crossed-dipole array (1-2 GHz). (b) Rectangular plot of $|E_\theta|$ far-field (1-2 GHz). (c) Far-field plot of $|E_\theta|$ azimuthal amplitude pattern for two-column staggered crossed-dipole array (0.72-2.45 GHz). (d) Rectangular plot of $|E_\theta|$ far-field (0.72-2.45 GHz).

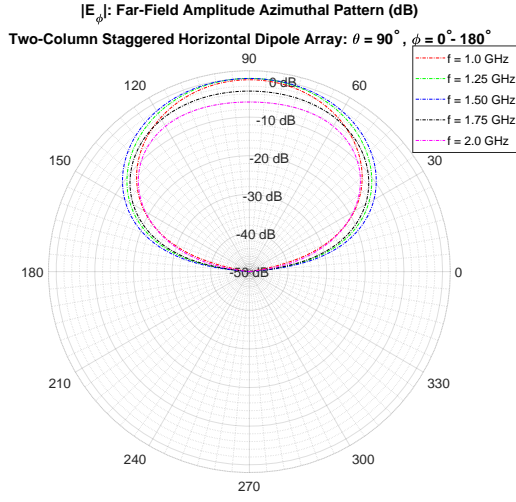


(a)

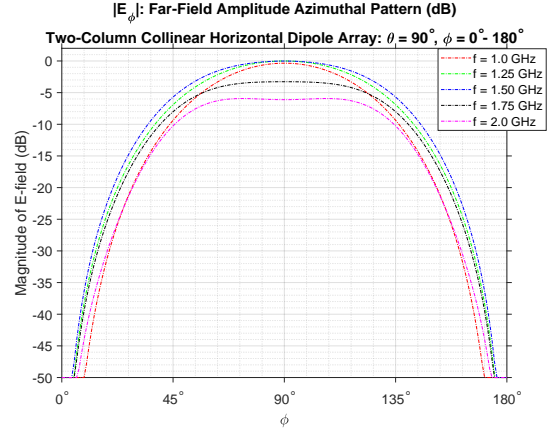


(b)

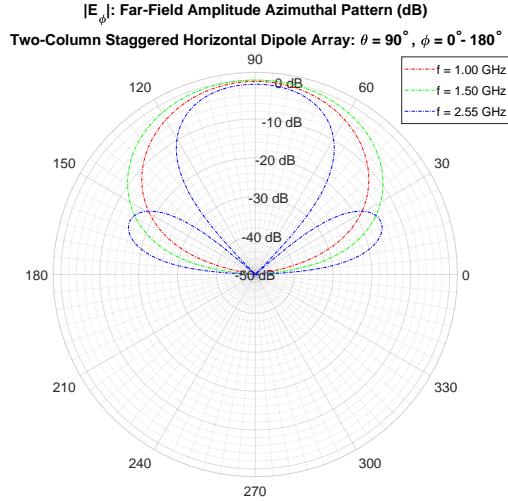
Figure 4.21: (a) $|E_\theta|$ Far-field amplitude elevation pattern for staggered crossed-dipole array (b) $|E_\theta|$ Far-field amplitude elevation pattern for staggered crossed-dipole array rectangular plot



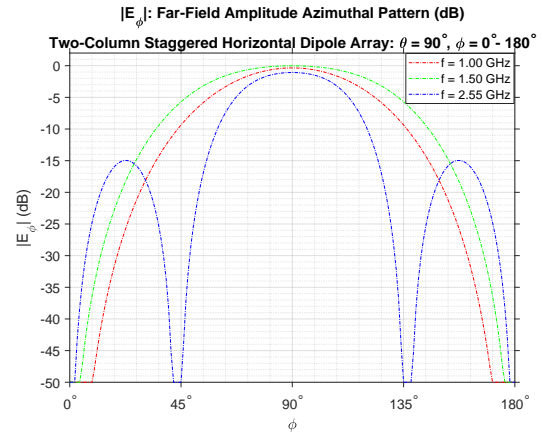
(a)



(b)

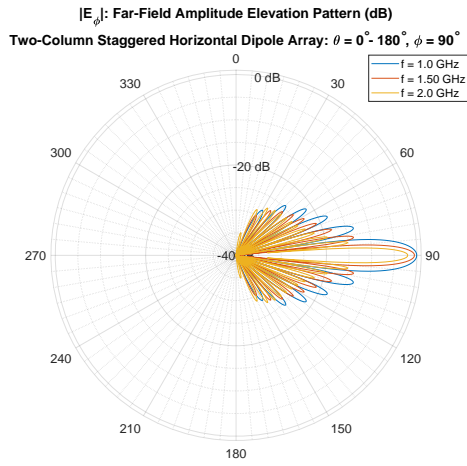


(c)

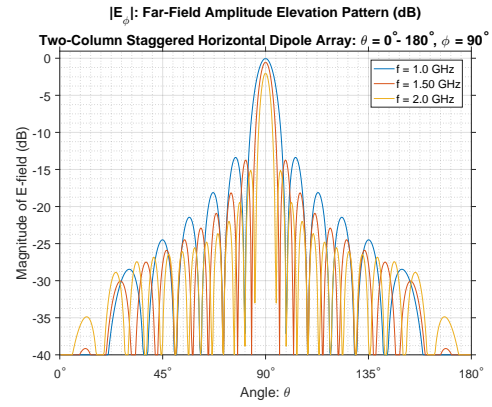


(d)

Figure 4.22: (a) Far-field plot of $|E_\phi|$ azimuthal amplitude pattern for two-column staggered crossed-dipole array (1-2 GHz). (b) Rectangular plot of $|E_\phi|$ far-field (1-2 GHz). (c) Far-field plot of $|E_\phi|$ azimuthal amplitude pattern for two-column staggered crossed-dipole array (1.00-2.55 GHz) (d) Rectangular plot of $|E_\phi|$ far-field (1.00-2.55 GHz).



(a)



(b)

Figure 4.23: (a) $|E_\phi|$ Far-field amplitude elevation pattern for staggered crossed-dipole array (b) $|E_\phi|$ Far-field amplitude elevation pattern for staggered crossed-dipole array rectangular plot

V. Conclusion

The impedance bandwidth of a tightly-packed crossed-dipole array antenna was studied in this thesis. In particular, the effect of changing the inter-element spacing in the array on the antenna's bandwidth was investigated. The objective of the research was to design an antenna with an impedance bandwidth large enough to cover the L-band range of frequencies. This bandwidth was defined as the set of frequencies where the VSWR at the terminals of the crossed-dipoles in the array is below 2.

This study was conducted to extend previous research that was performed on designing a feed for a large, deployable, cruciform reflector which is intended to be used on a communications satellite. Previous research on the feed focused on the pattern characteristics of a feed design consisting of a sparser array of dipoles at a single frequency. The study reported in this thesis tested the hypothesis that a denser array of periodically spaced elements could produce a higher bandwidth by exploiting the mutual coupling between elements.

The research was performed by conducting a parametric study using a computational electro-magnetics code. Using this code, different array configurations with varying element spacings were simulated. The results of this parametric study were used to simulate a final array configuration. The impedance characteristics of this final design were then used to design a stepped-transmission line wideband matching network for the array that brought the VSWR of the elements below 2. An impedance bandwidth of 2.6:1 was achieved for the crossed-dipole array which exceeded coverage of the L-band frequencies. The beneficial effect of mutual coupling in minimizing the variation in terminal impedance from frequency to frequency was seen to be stronger for denser array configurations.

Both a collinear arrangement of dipoles and a denser staggered arrangement were tested. The current distribution and far-field plots calculated for these two different

configurations showed that the denser staggered array produced a more uniform far-field pattern across the L-band frequency range as well at the expense of a wider main-beam.

Future studies could be conducted that refine the antenna design produced in this thesis by increasing the number of columns in the array. This could further increase the coupling to improve the bandwidth and could also result in a more narrow far-field pattern. Additionally, the effect of including a dielectric layer around the dipoles to further improve the bandwidth could also be investigated. A separate study has been proposed as well which would involve tailoring the current distribution on the array to produce a more desirable far-field pattern using the technique of pattern synthesis.

Overall, this study has demonstrated the viability of using a tightly-packed crossed-dipole array feed for the deployable, cruciform reflector antenna design. Using the design principles and analysis techniques demonstrated in this thesis, a dipole array feed could be designed in order to take advantage of the high gain provided by such a large reflector, and thereby improve the performance of future U.S. Air Force communication satellites.

Appendix: Full Results

A.1 SPLAT Files

The command file structure used in SPLAT is shown below [8]. (File extension = “.in”):

```
pattern_type                {'bistatic','monostatic','frequency sweep'}
start value, end value, increment    {Independent variable parameters}
theta_in, phi_in, phi_out, fGHZ
impedance_in_flag, impedance_write_flag, line_in_flag
[x_line,y_line]
['Z_matrix_file #1']
['Z_matrix_file #2']
['Z_matrix_file #3']
...
separation_criterion, rho, converge_pct, min_int
norm_type                    {'echowidth','regular','schneider'}
norm_flag
[norm_val]                    {read if norm_flag is set}
v_write_flag, cur_write_flag
inputs_only_flag, write_flag, plot3d, plotxz, plotyz
mag_field_out
'geometry file name'
'output file name'
partial_fields_flag, scan_impedance_flag, v_in_flag, cur_in_flag
['partial fields file name']
['scan impedance input file name', 'scan impedance output file name']
['voltage vector file name']
['current vector file name']
```

Based on the command file template, an example command file (“VLSA.in”) used in the parametric study is provided below:

```

'frequency sweep'      ! pattern type 'bistatic','monostatic','frequency sweep'
0.20,3.00,0.01          ! start value, end value, increment
90,90,90.,7.7          ! theta in, phi in, phi out, fGHz
.false.,.false.        ! impedance in flag, impedance write flag,
10.0,0.0,.01,80        ! sep. crit., rho, converge percent., min. interval
'schneider'            ! norm. type 'echowidth','regular','schneider'
.true.                 ! norm. flag
1.0                    ! norm. value
.true.,.true.          ! voltage write flag, current write flag
.false.,.true.         ! inputs only flag, write flag
.false.               ! magnetic field out flag
'VLSA2Col.geo'         ! geometry file name
'VLSA2Col.dat'         ! output file name
.false.,.false.,.true.,.false. ! partial fields., scan imp., volt. in., curr. in.
.false.,.false.       ! near fields flag, line source in flag
'VLSAvolt.vlt'        ! voltage vector file name

```

The geometry file structure used in SPLAT is shown below [8]. (File extension = “.geo”):

```

! Geometry Template File for SPLAT
!! Dz
    ! Interelement spacing within a column. Must be the same for all cols in array
!! ambient dielectric constant, ambient conductivity, ambient loss tangent
    !      1.0, 0.0, 0.0

```

```

!! NUM_SHELLS Section
!      BEGIN NUM_SHELLS lines:
!          shell radius, dielectric constant, conductivity, loss tangent
!          ...
!          shell radius, dielectric constant, conductivity, loss tangent
!      END NUM_SHELLS lines
!! NUM_CELL Section  number of cells?
!      BEGIN NUM_CELL lines:
!      NUM_NODES, NUM_SEGMENTS, NUM_MODES, NUM_ARRAYS
!      BEGIN NUM_NODES lines:
!          Node Label, x,y,z
!          ...
!          Node Label, x,y,z
!      END NUM_Nodes lines
!      BEGIN NUM_SEGMENTS lines:
!          Segment label, Node 1, Node 2
!          wire conductivity, wire radius, shell #
!          ...
!          Segment label, Node 1, Node 2
!          wire conductivity, wire radius, shell #
!      END NUM_SEGMENTS lines
!      BEGIN NUM_MODES lines:
!          segments, terminal, segment, ,segment
!          ...
!          segments, terminal, segment, ,segment
!      END NUM_MODES lines
!      BEGIN NUM_ARRAYS lines:
!          # clones, Dx, xc, yc, zc, alpha
!          ...
!          # clones, Dx, xc, yc, zc, alpha
!      END NUM_ARRAYS lines
!      END NUM_CELL lines

```

```

!! NUM_LOADS, NUM_CKT, NUM_RODS section

! BEGIN NUM_LOADS lines:
    ! [mode #, complex lumped load value, [,circuit flag]]
    ! ...
    ! [mode #, complex lumped load value, [,circuit flag]]
! END NUM_LOADS lines
! BEGIN NUM_CKT lines:
    ! [inductor, capacitor, center frequency]
    ! ...
    ! [inductor, capacitor, center frequency]
! END NUM_CKT lines
! BEGIN NUM_RODS lines:
    ! [mode #, complex permittivity of rod]
    ! ...
    ! [mode #, complex permittivity of rod]
! END NUM_RODS lines

```

Based on the geometry file template, an example geometry file (“VLSA2Col.geo”) used in the parametric study is provided below:

```

10.000000          ! Dz: Interelement spacing within a column.
1.0 0.0 0.0        ! ambient dielec. const., ambient conduct., ambient loss tang.
0                  ! NUM_SHELLS: Number of dielectric shells
1                  ! NUM_CELL: Number of cells
5 4 3 1            ! Num. of Nodes, Num. of Segments, Num. of Modes, Num. of Arrays
10 0.000 0.000 -4.500    ! Node label, x, y, z
15 0.000 0.000 -2.250    ! Node label, x, y, z
20 0.000 0.000 0.000     ! Node label, x, y, z
25 0.000 0.000 2.250     ! Node label, x, y, z

```

```

30 0.000 0.000 4.500      ! Node label, x, y, z
1 10 15                    ! Segment label, Node 1, Node 2
.0000 0.5000 0            ! wire conductivity, wire radius, shell number
2 15 20                    ! Segment label, Node 1, Node 2
.0000 0.5000 0            ! wire conductivity, wire radius, shell number
3 20 25                    ! Segment label, Node 1, Node 2
.0000 0.5000 0            ! wire conductivity, wire radius, shell number
4 25 30                    ! Segment label, Node 1, Node 2
.0000 0.5000 0            ! wire conductivity, wire radius, shell number
2 15 1 2                   ! Number of segments, terminal node, start segment, end segment
2 20 2 3                   ! Number of segments, terminal node, start segment, end segment
2 25 3 4                   ! Number of segments, terminal node, start segment, end segment
2 10.0 0 0 0 0            ! Number of clones, Dx, x center, y center, z center, alpha
0 0 0                     ! Number of loads, Number of circuits, Number of rods

```

The voltage vector files are simply a list of the complex voltages defined for the modes spanning each reference dipole separated into their real and imaginary components and theta and phi polarizations:

```

0.000,0.000,0.000,0.000  !Complex voltage theta pol., Complex voltage phi pol.
1.000,0.000,0.000,0.000  !Complex voltage theta pol., Complex voltage phi pol.
0.000,0.000,0.000,0.000  !Complex voltage theta pol., Complex voltage phi pol.
0.000,0.000,0.000,0.000  !Complex voltage theta pol., Complex voltage phi pol.
1.000,0.000,0.000,0.000  !Complex voltage theta pol., Complex voltage phi pol.
0.000,0.000,0.000,0.000  !Complex voltage theta pol., Complex voltage phi pol.

```

Finally, an example output file from SPLAT is shown below which lists the value of the E-field for the various output angles and the value of the current coefficients for the current modes spanning the reference dipole. The order of the currents listed is the order in which the modes are defined in SPLAT [8]:

SPLAT - Frequency Sweep

Phi_in = 90.000 Phi_out = 90.000 Theta_in = 90.000

FreqGHz	RealField	ImagField	RealField	ImagField
.2000	-.135204E-01	-.463950	0.000000	0.000000
.2100	-.165232E-01	-.513436	0.000000	0.000000
.2200	-.200171E-01	-.565661	0.000000	0.000000
.2300	-.240414E-01	-.620674	0.000000	0.000000
.2400	-.286717E-01	-.678494	0.000000	0.000000
.2500	-.339375E-01	-.739172	0.000000	0.000000
.2600	-.399367E-01	-.802732	0.000000	0.000000
.2700	-.467124E-01	-.869204	0.000000	0.000000
.2800	-.543390E-01	-.938638	0.000000	0.000000
.2900	-.628684E-01	-1.01104	0.000000	0.000000
.3000	-.724284E-01	-1.08646	0.000000	0.000000
...				
2.900	-16.6157	14.4974	0.000000	0.000000
2.910	-16.6933	14.4625	0.000000	0.000000
2.920	-16.7734	14.4306	0.000000	0.000000
2.930	-16.8586	14.4052	0.000000	0.000000
2.940	-16.9445	14.3818	0.000000	0.000000
2.950	-17.0332	14.3656	0.000000	0.000000
2.960	-17.1323	14.3568	0.000000	0.000000

2.970	-17.2352	14.3620	0.00000	0.00000
2.980	-17.3351	14.3624	0.00000	0.00000
2.990	-17.4325	14.3909	0.00000	0.00000
3.000	-17.6568	14.5520	0.00000	0.00000

Induced Voltage

j	v_thetaj		v_phij	
1	0.0000000E+00	0.0000000E+00	0.0000000E+00	0.0000000E+00
2	1.000000	1.3741843E-07	0.0000000E+00	0.0000000E+00
3	0.0000000E+00	0.0000000E+00	0.0000000E+00	0.0000000E+00
4	0.0000000E+00	0.0000000E+00	0.0000000E+00	0.0000000E+00
5	1.000000	-1.3741843E-07	0.0000000E+00	0.0000000E+00
6	0.0000000E+00	0.0000000E+00	0.0000000E+00	0.0000000E+00

Currents

j	cur_thetaj		cur_phij	
1	1.4192660E-03	-6.4815148E-03	0.0000000E+00	0.0000000E+00
2	2.6863783E-03	6.9596781E-03	0.0000000E+00	0.0000000E+00
3	1.3820748E-03	-5.0058910E-03	-0.0000000E+00	0.0000000E+00
4	1.6863216E-03	-5.9982189E-03	0.0000000E+00	0.0000000E+00
5	2.6852910E-03	6.9657355E-03	0.0000000E+00	0.0000000E+00
6	1.1049735E-03	-5.4761223E-03	-0.0000000E+00	0.0000000E+00

Bibliography

- [1] D. Van Dyne, “Simulation of locking space truss deployments for a large deployable sparse aperture reflector,” Master’s thesis, Air Force Institute of Technology, 2015.
- [2] J. M. Wilson, “The design and analysis of electrically large custom-shaped reflector antennas,” Master’s thesis, Air Force Institute of Technology, 2013.
- [3] J. Wilson, E. Moore, S. Hartzell, R. Marhefka, and A. Terzuoli, “Sparse cruciform reflector with phased array feed,” in *2014 USNC-URSI Radio Science Meeting (Joint with AP-S Symposium)*, pp. 31–31, July 2014.
- [4] D. Hesser, L. Lee, L. Burchett, R. Marhefka, A. Terzuoli, and R. Wasky, “Structural and electromagnetic design considerations for very large space antennas,” in *2017 IEEE International Symposium on Antennas and Propagation USNC/URSI National Radio Science Meeting*, pp. 559–560, July 2017.
- [5] B. A. Munk, *Finite Antenna Arrays and FSS*. John Wiley and Sons, 2003.
- [6] S. X. Ta, I. Park, and R. W. Ziolkowski, “Crossed dipole antennas: A review.,” *IEEE Antennas and Propagation Magazine*, vol. 57, pp. 107–122, Oct 2015.
- [7] C. A. Balanis, *Antenna Theory Analysis and Design*. John Wiley and Sons, 2005.
- [8] D. S. Janning, *SPLAT User’s Guide and Programmer’s Manual*. 2010.
- [9] J. Heller, A. Jennings, J. Black, and G. Greschik, “Precision of large deployable reflector,” in *2014 AIAA Spacecraft Structures Conference*, 2014.
- [10] J. C. Heller, “Feasibility of very large sparse aperture deployable antennas,” Master’s thesis, Air Force Institute of Technology, 2013.

- [11] B. A. Munk, *Frequency Selective Surfaces Theory and Design*. John Wiley and Sons, 2000.
- [12] A. Bhattacharyya, *Phased Array Antennas: Floquet Analysis, Synthesis, BFNs and Active Array Systems*. Wiley Series in Microwave and Optical Engineering, Wiley, 2006.
- [13] D. S. Janning, *Surface Waves in Arrays of Finite Extent*. PhD thesis, Ohio State University, 2000.
- [14] H. U. United States. Radio Research Laboratory and H. Reich, *Very high-frequency techniques*. No. v. 1 in Very High-frequency Techniques, McGraw-Hill Book Co., 1947.
- [15] V. H. Rumsey, “The design of frequency-compensating matching sections,” *Proceedings of the IRE*, vol. 38, pp. 1191–1196, Oct 1950.
- [16] M. A. Hamid and M. M. Yunik, “On the design of stepped transmission-line transformers (correspondence),” *IEEE Transactions on Microwave Theory and Techniques*, vol. 15, pp. 528–529, September 1967.
- [17] F. A. Regier, “Impedance matching with a series transmission line section,” *Proceedings of the IEEE*, vol. 59, pp. 1133–1134, July 1971.
- [18] K. Warnick, *Numerical Methods for Engineering: An Introduction Using MATLAB and Computational Electromagnetics Examples*. Electromagnetics and Radar Series, SciTech Pub., 2011.
- [19] D. Pozar, *Microwave Engineering, 4th Edition*. Wiley, 2011.
- [20] J. Kraus and R. Marhefka, *Antennas for all applications*. McGraw-Hill series in electrical engineering, McGraw-Hill, 2002.

- [21] R. Marhefka, “A design study of the feed for the very large cruciform antenna (white paper),” October 2017.

REPORT DOCUMENTATION PAGE				<i>Form Approved OMB No. 0704-0188</i>	
<small>The public reporting burden for this collection of information is estimated to average 1 hour per response, including the time for reviewing instructions, searching existing data sources, gathering and maintaining the data needed, and completing and reviewing the collection of information. Send comments regarding this burden estimate or any other aspect of this collection of information, including suggestions for reducing the burden, to Department of Defense, Washington Headquarters Services, Directorate for Information Operations and Reports (0704-0188), 1215 Jefferson Davis Highway, Suite 1204, Arlington, VA 22202-4302. Respondents should be aware that notwithstanding any other provision of law, no person shall be subject to any penalty for failing to comply with a collection of information if it does not display a currently valid OMB control number.</small>					
PLEASE DO NOT RETURN YOUR FORM TO THE ABOVE ADDRESS.					
1. REPORT DATE (DD-MM-YYYY)		2. REPORT TYPE		3. DATES COVERED (From - To)	
4. TITLE AND SUBTITLE				5a. CONTRACT NUMBER	
				5b. GRANT NUMBER	
				5c. PROGRAM ELEMENT NUMBER	
6. AUTHOR(S)				5d. PROJECT NUMBER	
				5e. TASK NUMBER	
				5f. WORK UNIT NUMBER	
7. PERFORMING ORGANIZATION NAME(S) AND ADDRESS(ES)				8. PERFORMING ORGANIZATION REPORT NUMBER	
9. SPONSORING/MONITORING AGENCY NAME(S) AND ADDRESS(ES)				10. SPONSOR/MONITOR'S ACRONYM(S)	
				11. SPONSOR/MONITOR'S REPORT NUMBER(S)	
12. DISTRIBUTION/AVAILABILITY STATEMENT					
13. SUPPLEMENTARY NOTES					
14. ABSTRACT					
15. SUBJECT TERMS					
16. SECURITY CLASSIFICATION OF:			17. LIMITATION OF ABSTRACT	18. NUMBER OF PAGES	19a. NAME OF RESPONSIBLE PERSON
a. REPORT	b. ABSTRACT	c. THIS PAGE			19b. TELEPHONE NUMBER (Include area code)